THESIS

LOOK UP: PROBING THE VERTICAL PROFILE OF NEW PARTICLE FORMATION AND GROWTH IN THE PLANETARY BOUNDARY LAYER WITH MODELS AND OBSERVATIONS

Submitted by

Samuel O'Donnell

Department of Atmospheric Science

In partial fulfillment of the requirements

For the Degree of Master of Science

Colorado State University

Fort Collins, Colorado

Summer 2022

Master's Committee:

Advisor: Jeffrey Pierce

Shantanu Jathar
Sonia Kreidenweis

ABSTRACT

LOOK UP: PROBING THE VERTICAL PROFILE OF NEW PARTICLE FORMATION AND GROWTH IN THE PLANETARY BOUNDARY LAYER WITH MODELS AND OBSERVATIONS

The processes of new particle formation (NPF) and growth are important contributors to cloud condensation nuclei (CCN) concentrations, and CCN are important for climate from their impact on planetary radiative forcing. While the general ubiquity and importance of NPF is understood, the vertical extent and governing mechanisms of NPF and growth in the lower troposphere are uncertain. We present a two-part analysis of the vertical profile of NPF during the HI-SCALE field campaign at the Southern Great Plains observatory in Oklahoma, USA. Firstly, we analyzed airborne and ground-based observations of four NPF events. Secondly, we used a column aerosol chemistry and microphysics model, along with the observations, to probe factors that influence the vertical profile of NPF. During HI-SCALE, we found several instances of enhanced NPF occurring several hundred meters above the surface; however, the spatio-temporal characteristics of the observed NPF made comparisons between airborne- and ground-based observations difficult. For six unique events, the model represented the observed NPF (or lack of NPF) and particle growth at the surface to within 10 nm. The model predicted enhanced NPF rates in the upper mixed layer, and this enhancement is primarily due to the temperature dependence in the NPF schemes. The simulations were sensitive to the initial vertical profile of gas-phase species from HI-SCALE, such that vertical mixing in the model either enhanced or suppressed NPF rates, aerosol number concentrations, and particle growth rates at the surface. Finally, our analysis

provides insights for future field campaigns and modeling efforts investigating the vertical profile of NPF.

ACKNOWLEDGMENTS

I would like to extend my utmost gratitude to my co-authors and collaborators who were instrumental in shaping this work:

- Ali Akherati spent copious hours helping with model developments and understanding;
- Yicong (Charles) He provided SOM yields and informed the HOM parameterizations;
- Anna Hodshire helped with the analysis of HI-SCALE data, and provided extensive feedback on the manuscript;
- John Shilling provided great insight into the PTR-MS and the SMPS data from PNNL;
- Chongai Kuang provided insight into much of the data at SGP, and he meticulously processed aerosol size distribution data for this analysis;
- Jerome Fast provided valuable insight into the HI-SCALE campaign and the accuracy and readability of this manuscript;
- Fan Mei worked on the CPCs used during HI-SCALE, and she provided insight into how the data were collected;
- Charles Long who collected irradiation data during HI-SCALE;
- Siegfried Schobesberger and Joel Thornton provided great feedback and insight into the HRToF-CIMS data;
- Jim Smith provided feedback throughout the development of this project, and his insights greatly shaped this work;
- Shantanu Jathar always provided great feedback and posed intriguing science questions about the work, ultimately leading to a vastly improved final result;

- I would also like to extend the greatest appreciation to my advisor, Jeffrey Pierce, for his well-rounded support, affirmation, motivation, and patience throughout this project. I am consistently reminded of Jeff's enthusiasm and depth of knowledge about aerosol microphysics, and I have always appreciated our conversations about science and life in general.

This work was supported by the Atmospheric System Research (ASR) program, part of the US Department of Energy's Office of Biological and Environmental Research within the Office of Science, under grants DE-SC0019000, DE-SC0021208 and DE-SC0017975 and the National Oceanic and Atmospheric Administration (NA17OAR4310003). Pacific Northwest National Laboratory (PNNL) investigators JES and JDF were also supported by the ASR program. PNNL is operated by DOE by the Battelle Memorial Institute under contract DE-A06-76RLO 1830. The HI-SCALE field campaign was supported by the Atmospheric Radiation Measurement (ARM) Climate Research Facility. HI-SCALE data used in this manuscript are freely available from the ARM data archive (https://www.arm.gov/data and https://www.arm.gov/research/campaigns/aaf2016hiscale).

Finally, I would like to thank my friends and family for their unwavering support and encouragement throughout this endeavor.

TABLE OF CONTENTS

ABSTRACT ii

ACKNOWLEDGMENTS iv

Chapter 1. Introduction 1

Chapter 2. Methods 9

2.1. Aerosol and chemical data 9

2.1.1. Surface instrumentation 10

2.1.2. Aircraft instrumentation 11

2.1.3. Choice of included data and analysis days 13

2.2. Meteorological data 14

2.3. Models 15

2.3.1. SOM-TOMAS 15

2.3.2. Incorporating gas-phase observations in the model 20

2.3.3. Initializing aerosol size distributions 22

2.3.4. Meteorology in SOM-TOMAS 24

2.3.5. Hydroxyl radical concentrations 24

2.3.6. Model uncertainty analysis 26

2.3.7. Vertical sensitivity analysis 28

2.3.8. HYSPLIT model 29

Chapter 3. Results 30

3.1. NPF during HI-SCALE 30

3.1.1. Overview of surface observations 30

3.1.2. Evidence for NPF occurring aloft during HI-SCALE 33

3.2. Model Results 36

3.2.1. Model results of NPF events and non-NPF events at the surface 36

3.2.2. Analysis of uncertain model parameters 38

3.2.3. NPF occurring aloft in the model 41

3.2.4. Analysis of potential drivers of NPF aloft 44

3.3. Discussion on the necessary constraints to better understand the vertical profile of nucleation and growth 50

Chapter 4. Conclusions 58

Bibliography 62

Appendix A 84

Appendix B 85

CHAPTER 1

INTRODUCTION

Aerosol particles exert considerable influence on global climate through direct and indirect radiative forcing. Aerosol particles absorb and scatter shortwave-solar radiation, in turn having a direct influence on local and global planetary insolation (Charlson et al., 1992; Myhre et al., 2013). Additionally, aerosol particles with diameters (D_p) larger than ~50 nm can act as cloud condensation nuclei (CCN), the particles on which cloud droplets form, with more hydrophilic particles at the same size activating to cloud droplets more readily. Hence, CCN number concentrations directly influence the cloud droplet number concentration, subsequently altering cloud albedo, lifetime, frequency, precipitation efficiency, and development (Twomey, 1974; Albrecht, 1989; Gryspeerdt et al., 2014; Rosenfeld et al., 2014; Clement et al., 2009; Stevens and Feingold, 2009). The cumulative effects of aerosol particles, both direct and indirect, on climate remains one of the largest uncertainties in past and future climate estimates, driving the need to better understand the processes that influence these aerosol forcings (Boucher et al., 2013).

New particle formation (NPF) is the formation of sub-nanometer particles from low-volatility vapors and is the largest source of particle number in the atmosphere (Seinfeld and Pandis, 2016; Kulmala et al., 2004, 1998; Kulmala and Kerminen, 2008). To survive to reach climate-relevant sizes, these freshly nucleated particles with diameters ~1 nm must grow, primarily through condensation of low-volatility gases, to larger sizes where the rate of coagulational scavenging by existing particles is lower (Pierce and Adams, 2007; Wang et al., 2020). NPF events generally last for several hours with subsequent growth happening over subsequent hours to days (Kulmala et al., 2004; Kerminen et al., 2018; Pierce et al., 2012). This process of NPF and growth occurs in many locations throughout the lower and upper troposphere and has been estimated to

contribute a substantial fraction of the global average low-cloud-level CCN in the present-day (38-66%) and pre-industrial (44-84%) atmospheres (Gordon et al., 2017; Pierce and Adams, 2009c; Dunne et al., 2016). Lower-tropospheric NPF events can take place over vastly different spatial scales ranging from localized plumes spanning several hundred meters, to regional events that take place over tens to hundreds of kilometers (Kerminen et al., 2018; Kulmala et al., 2004; Stevens and Pierce, 2014). The temporal frequency of NPF events also vary on annual (e.g., the seasonal cycles of precursor vapors and sinks) to hourly (e.g., changes in vapor sources and vapor/particle sinks that determine the length of NPF events) scales, thus creating a two-fold problem of scale when trying to create representative models for NPF and growth that will work in a diversity of environments in atmospheric models (Lee et al., 2019).

While precise mechanistic descriptions of NPF are still uncertain, there are many theoretical and semi-empirical mechanisms describing NPF in the troposphere (Dunne et al., 2016; Riccobono et al., 2014; Lehtipalo et al., 2018; Lee et al., 2019). In most tropospheric environments, these mechanisms depend on sulfuric acid and one or more of ammonia, amines, water vapor, and certain organic species. In virtually all cases, lower temperature is more favorable for particle nucleation. Sulfuric acid has been recognized as a key component for stabilizing molecular clusters and early particle growth due to its low saturation vapor pressure and affinity for reaction with base compounds such as ammonia and amines to form salts (e.g., Ball et al., 1999). Along with sulfuric acid, recent studies have emphasized the importance of low-volatility and highly oxygenated organic molecules (HOMs) for their role in NPF and early particle growth (Bianchi et al., 2019). Studies using the European Council for Nuclear Research's Cosmics Leaving OUtdoor Droplets (CLOUD) chamber have found that the HOMs can cluster efficiently with sulfuric acid under atmospheric conditions, which could help explain observed NPF in the boreal environment

(Tröstl et al., 2016). Additionally, Kirkby et al. (2016) found HOMs alone could form stable clusters under atmospheric conditions; however, the role of pure organic NPF in the atmosphere is still highly uncertain given the multitude of organic and inorganic species participating in NPF as well as the presence of non-trivial sulfuric acid concentrations in much of the present-day troposphere. Water vapor or relative humidity (RH) also plays a role in stabilizing reactions with sulfuric acid, especially in the absence of bases and organics (Dunne et al., 2016; Lee et al., 2019; Yu et al., 2017b). The sulfuric acid-water NPF can be an important mechanism in cold regions with lower concentrations of bases and organic species (e.g. upper troposphere). Finally, aerosol particle-phase diffusivity can affect the growth rate of particles by changing the equilibrium partitioning timescale for condensing mass. Several studies have found that treating particles as semi-solid leads to faster growth of nucleation mode particles due to the squared-radius dependence of internal mixing and, thus, equilibrium partitioning (He et al., 2021; Zaveri et al., 2014, 2018).

The most comprehensive observations of NPF events have been made at the surface, which is likely representative of the lower mixed layer (mixed layer: lower 0-2 km of the troposphere that is well-mixed due to free convection or mechanical turbulence; Figure 1). However, many studies have found NPF to occur at various levels between the surface and several km in altitude, including the top of the mixed layer and within the residual layer (residual layer: the region between the top of the currently developing mixed layer and the top of the previous-days' mixed layer; Figure 1). Further, studies have also focused on NPF in the upper troposphere (Park et al., 2021; Rose et al., 2017; Bianchi et al., 2016; Zhao et al., 2020), ~10 km and higher, but we will not focus on this NPF in this manuscript. Nilsson et al. (2001) found NPF events observed at the surface to be highly correlated with the rapid development of the mixed layer during the day, thus

pointing to several potential mechanisms for mixed layer-NPF interactions, namely (Figure 1): (1) entrainment of particles formed by NPF in the residual layer into the mixed layer; (2) mixing of NPF precursors between the residual layer and the mixed layer; (3) mixing of convective parcels in the mixed layer with adiabatic cooling during lifting leading to enhanced NPF; (4) decreases in existing aerosol concentrations in the mixed layer due to entrainment of cleaner air from the residual layer, thus leading to reduced coagulation and condensation sinks and enhanced NPF and growth. Since Nilsson et al. (2001), studies have utilized airborne measurement platforms and found NPF occurring at various levels within the mixed layer and often near the top of the mixed layer (e.g. Wehner et al., 2007, 2010; Schobesberger et al., 2013; Chen et al., 2018; Platis et al., 2016; Leino et al., 2019; Nikandrova et al., 2018; Lampilahti et al., 2021a, 2021b; Qi et al., 2019, Boulon et al., 2011). These enhancements are still thought to be a result of the mechanisms (1)-(4) from Nilsson et al (2001); however, the exact influence of each mechanism is uncertain, and the influence of additional factors, such as temperature and chemistry, are not fully understood. Figure 1 summarizes mechanisms (1)-(4) above, in addition to highlighting the potential influences of temperature, long-range transport, and different chemical drivers on NPF and growth.

NPF occurring aloft can be indistinguishable from NPF occurring at the surface using surface aerosol size distributions if particles formed aloft rapidly mix down to the surface before they have grown to larger sizes. This is understandable since mixing timescales within the mixed layer are often on the order of ~30 minutes. In cases where mixing to the surface is delayed, particles may be first detected at the surface after they have already undergone substantial growth to ~10-20 nm sizes, indicating that NPF occurred elsewhere in the atmosphere (Pierce et al., 2012; Wang et al., 2016; Wehner et al., 2007, 2010; Birmili and Wiedensohler, 2000). However, surface observations of nascent 10-20 nm particles alone may not necessarily be from NPF and growth

aloft because these particles may also have been formed in a plume that advected over the measurement site due to a wind shift (Stevens and Pierce, 2012; Song et al., 2010; Wehner et al., 2007) or be from primary ultrafine emissions such as from fungal spore rupturing (Subba et al., 2021; Lawler et al., 2020; Ruiz-Jimenez et al., 2021). This difficulty in distinguishing NPF events occurring aloft can lead to inaccurate understanding of NPF in the troposphere from ambient surface data.

Several studies have tried to address knowledge gaps associated with the vertical extent of NPF through the use of 1-dimensional (1D) column models. Hellmuth (2006) developed a 1D model to investigate gas-aerosol-turbulence interactions in the planetary boundary layer, which included a third-order closure approach to boundary layer turbulence, sulfur and ammonia chemistry, and aerosol dynamics. However, the model represented only ammonia and sulfur chemistry/aerosols, aerosol dynamics for three aerosol modes, and binary (sulfuric acid-water) and ternary (sulfuric acid-water-ammonia) inorganic nucleation schemes that are inconsistent with more recent experiments and schemes. The vertical profiles of aerosol particles and gas-phase species (including atmospheric oxidants) were assumed to decrease linearly with altitude. Using the model, Hellmuth (2006) found binary NPF to be favored in the upper third of the developing mixed layer while ternary NPF takes place earlier in the mixed layer development at the surface in addition to in the free troposphere. Particles that formed aloft were then mixed downward to the surface, leading to the conclusion that surface observations and single box models were insufficient to capture the origin of freshly nucleated particles; however, measurements were not used to constrain the model or test the results. Similarly, Boy et al. (2006) used a different column model (Model to predict new Aerosol formation in the Lower TropospherE: MALTE) to investigate NPF, particle growth, and deposition in and above a forest canopy. MALTE utilizes

relatively similar meteorology schemes and representations of aerosol nucleation and dynamics as Hellmuth (2006); however, the MALTE chemistry package is considerably more complex (70 species, 123 chemical and 16 photochemical reactions), including secondary organic aerosol (SOA) production for aerosol growth. The aerosol size distribution and some gas-phase species were constrained with 12 h surface measurements, but the vertical gradients of said quantities were assumed to all follow the same linearly decreasing vertical fit. Boy et al. (2006) found most NPF and growth occurring in the lower mixed layer over the boreal forest in Finland due to the intense biogenic emissions of organic species that contributed to stronger particle growth and survival. Similarly, Lauros et al., (2011) used MALTE, with updated turbulence parameters and organic NPF mechanisms, to investigate the vertical gradients of NPF over boreal Finland, and they found organic mediated nucleation was likely to play a significant, but uncertain, role in that region. However, the vertical profiles of aerosol particles and gas-phase species were initialized at zero and again were not constrained by observations. Overall, this body of work highlights the importance of atmospheric turbulence and mixing for NPF in the lower troposphere, but there is a need for more constraints on the vertical profiles of aerosol particles and gas-phase species from observations.

As discussed, some studies have investigated and compared observations of NPF events at the surface and from airborne platforms, and fewer studies have modeled NPF vertically; therefore, an opportunity exists to fill knowledge gaps by combining observations of vertically resolved NPF events with one-dimensional modeling. The small unmanned aerial vehicles and tethered balloons used in many studies have limited payloads, thus limiting the amount of potential data that can be used for modeling; however, this limitation is balanced by their ability to provide more frequent vertical profiles of the atmosphere, often extending from the surface up to ~1000 m. In contrast,

larger aircraft with greater payload capacity can provide a large suite of data products that are useful for modeling; however, the logistics of larger aircraft operations reduce flight frequency and the ability to collect data near the surface. Given this limitation, few studies have utilized the wealth of data from larger-capacity aircraft, such as the aircraft flown during the Holistic Interactions of Shallow Clouds, Aerosols, and Land Ecosystems (HI-SCALE) campaign, in conjunction with a one-dimensional model to investigate the vertical profile and drivers of NPF in the PBL.

This work aims to test our understanding of the vertical profile of NPF in the lower troposphere and utilizes data from the Holistic Interactions of Shallow Clouds, Aerosols, and Land Ecosystems (HI-SCALE) field campaign in north-central Oklahoma, USA. We use the data from HI-SCALE to constrain and inform a mechanistic chemical and microphysical column model of the PBL in order to analyze the dominant drivers of NPF and probe uncertainties in our understanding of NPF vertically. We find that even using vertically informed field data and a state-of-the-science model, many limitations remain in our analysis, and we highlight these throughout. Section 2 outlines the observations from HI-SCALE and the modeling approach used. Section 3.1 shows the results from the HI-SCALE campaign, and Section 3.2 shows the subsequent modeling results. Section 3.3 is a discussion of relevant uncertainties/limitations in our work and suggestions for future approaches for field campaigns and modeling efforts. Conclusions and future work are outlined in Section 4.

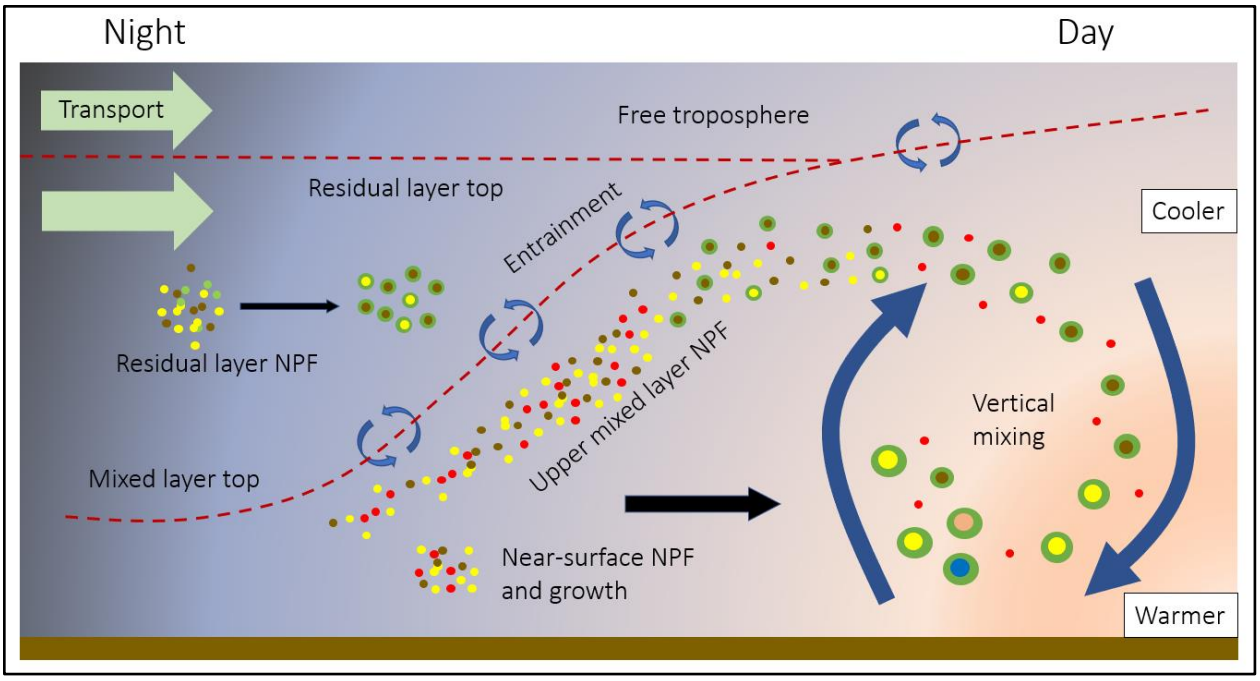

Figure 1. Schematic highlighting processes that may contribute to the vertical profile of NPF and growth in the lower troposphere. Green arrows indicate long range transport of air in the free troposphere and the residual layer. NPF and early particle growth may occur within the residual layer, and these particles may be entrained into the mixed layer. NPF may also occur near the surface and in the upper parts of the mixed layer. NPF may be favored in the upper part of the mixed layer due to lower temperatures. Vertical mixing of aerosol particles and gases in the mixed layer may influence NPF and particle growth.

CHAPTER 2

METHODS

2.1. AEROSOL AND CHEMICAL DATA

The Holistic Interactions of Shallow Clouds, Aerosols, and Land Ecosystems (HI-SCALE, Fast et al., 2019) campaign consisted of two intensive observational periods (IOPs) during the Spring and Summer of 2016 at the Atmospheric Radiation Measurement (ARM) Southern Great Plains (SGP) observatory in north-central Oklahoma (36.60°N and 97.48°W). The first IOP (IOP1) took place from 24 April to 21 May and the second IOP (IOP2) took place from 28 August to 23 September. During HI-SCALE, a large suite of instruments at the surface measured gas-phase organic and inorganic species, aerosol size and composition, and atmospheric state variables. Ground-based instruments were either located in the SGP central facility or the guest facility (~300 m apart), and this difference in location is considered to be unimportant for this work. The surface instrumentation was complemented by instruments aboard the ARM Aerial Facility (AAF) Gulfstream-159 (G-1) aircraft, which flew 38 research flights and collected similar, but not entirely identical, quantities as the surface instrumentation. The SGP site is mostly surrounded by agricultural land with intermittent seasonal agricultural fires, and several small towns are within 100 km of the site and Wichita, Oklahoma City, and Tulsa are located within 200 km of the site (Sheridan et al., 2001); hence, the SGP site is influenced by air-masses from a diversity of regions with a diversity of characteristics. More details on the SGP site and the air-masses influencing it during HI-SCALE can be found in Parworth et al. (2015) and Liu et al. (2019), respectively.

2.1.1 - SURFACE INSTRUMENTATION

The SGP surface sites had a suite of instrumentation to measure, among other quantities, aerosol size distributions, gas-phase organic species, and sulfur dioxide.. The ARM Mobile Facility (AMF3) Aerosol Observing System (AOS) operated during IOP1 and included an SMPS and a Nano-SMPS measuring mobility diameters in the range of 11-460 nm and 2.89-60 nm respectively (Uin et al., 2020). The AMF3 AOS SMPS system consisted of a long DMA with a model 3772 CPC and the Nano-SMPS system consisted of a nano-DMA with a model 3776 ultrafine CPC. The measurement cycle for the SMPS and Nano-SMPS was 5 minutes, and the sample flow was dried using a Nafion dryer. SMPS and Nano-SMPS size distributions were merged in their overlapping size range, accounting for diffusional loss corrections and uncertainties in instrument flow rate. For our analysis, it was important to have measurements of sub-14 nm particles for the understanding of early particle growth; thus, we prioritized the use of the merged SMPS system data. The AMF3 AOS system Nano-SMPS and SMPS were only operational during IOP1, so the remainder of this work will focus on results from IOP1. During NPF events, particle growth rates of freshly nucleated particles were calculated using the merged AMF3 AOS SMPS data by tracking the change in the maximum of the $dN/d\log D_p$ particle size distribution between 2 and 80 nm. Reported growth rates are time averages of the changes in the maximum of the $dN/d\log D_p$ distribution (more discussion in the results section). Additionally, an Aerosol Chemical Speciation Monitor (ACSM) was deployed as part of the AOS system, which measures the chemical mass concentration of non-refractory sub-micron aerosol species including sulfate, ammonium, chloride, nitrate, and organic matter (Uin et al., 2019; Parworth et al., 2015). The ACSM measured in the size range of 80 nm to 1 μm with a measurement accuracy of ± 30% (Ng, et al. 2011). Similar to the SMPS systems, samples were dried using a Nafion dryer.

Gas-phase concentrations of benzene, isoprene, monoterpenes, toluene, xylenes, trimethylbenzene and its isomers, and several other species (not used) were measured using a proton transfer reaction mass spectrometer (PTR-MS, Ionicon; Liu et al., 2021). The instrument was run in the mass-scan mode in which a mass spectrum from m/z = 21 to m/z = 250 was recorded with 1 s dwell time on each unit m/z resulting in a total time for each measurement cycle of ~4 min. Drift tube pressure was set at 2.2 mbar, chamber temperature at 60 °C, and SEM voltage at 3250 V. Instrument background concentrations were subtracted from each sample, which limits the accuracy of the resultant concentration when initial concentrations were below 1 ppbv for the 1 s data. Many of the concentrations were below the 1 s limit of detection (LOD), therefore, we employed averaging and substitutional methods in order to resolve species that were near the 1 s LOD, described below. For analysis days with detected NPF events (discussion of selection criteria is in Section 2.1.3), averages of the organic species were taken for the 6 h following the onset of the NPF event at the surface (Figure S1a-d). For days without detectable NPF events, where there is no definitive start to a NPF event, a full 10 h average of organic species concentrations was taken starting at 04:00 UTC (09:00 CDT; Figure S1e-f). Averaging the gas-phase concentrations improved the single-measurement LOD. After averaging, several of the measured concentrations were still below the new LOD, therefore, these values were substituted by 0.5*LOD. Additionally, gas-phase SO_2 was measured using a Thermo Fisher Scientific Sulfur Dioxide Analyzer (Model 43i trace level-enhanced pulsed fluorescence SO2 analyzer) during IOP1 only. For consistency, we employed similar averaging techniques for the SO_2 as we did for the PTR-MS data.

2.1.2 - AIRCRAFT INSTRUMENTATION

The ARM Aerial Facility (AAF) Gulfstream-159 (G-1) aircraft flew a total of 17 research flights during IOP1 and 21 during IOP2. The AAF was fitted with a complementary suite of

instruments that measured similar, but not identical, quantities as the surface. Two Condensation Particle Counters (CPC) were onboard the G-1 aircraft which measured the total number concentrations of aerosol particles in diameter ranges of 10 nm - 3 µm (CPC 3010; TSI) and 3 nm - 3 µm (CPC 3025; TSI). The flow rate for the CPC 3010 was 1 LPM and the flow rate for the CPC 3025 was 1.5 LPM; both CPCs were located behind the isokinetic inlet, which adjusts sample flow depending on aircraft speed, and temperature and pressure changes; however, during spiraling vertical segments of the flights, the isokinetic inlet was not able to maintain optimal sampling conditions, ultimately affecting the accuracy of the CPC measurements. Hence, we only use the airborne CPC measurements for a qualitative estimate of layers with potentially recent NPF. We estimate the total number concentration of 3-10 nm particles (i.e., nucleation-mode particles) by subtracting the CPC 3010 number concentration from the CPC 3025 number concentration. For this work, we assume that significantly higher concentrations of 3-10 nm particles were indicative of recent NPF. In addition to the CPCs, a Fast Integrating Mobility Spectrometer (FIMS) was onboard the aircraft to measure aerosol size distributions in the 10-400 nm diameter range. Particles entering the FIMS receive a bipolar charge, are size-separated based on their electrical mobility, grown in a supersaturation of a working liquid, and their final state is recorded using a high-speed camera.

The gas-phase oxidation products of several volatile organic compounds (VOCs) as well as ammonia (NH_3), sulfur dioxide (SO_2) and sulfuric acid were measured using the University of Washington high-resolution time-of-flight chemical ionization mass spectrometer (HRToF-CIMS). When operating in standard mode, the HRToF-CIMS uses iodide (I^-) as the reagent ion to selectively ionize and quantify the mixing ratios of SO_2, sulfuric acid, and several VOC oxidation products by adduct formation with the iodide. For the 13 IOP1 research flights occurring after 1

May, the HRToF-CIMS was also run in positive-mode for relatively shorter periods of time, where benzene and benzene cluster cations were used as the reagent ion. In positive-mode, the HRToF-CIMS is primarily sensitive to hydrocarbons such as isoprene, monoterpenes, dimethyl sulfide, and NH_3. Calibration was performed using a gravimetrically calibrated source of ^{13}C formic acid that was continuously added during all flights except for 20 May, and the subsequently derived sensitivities were used to correct the sensitivities to, and variability of, organics for each flight (variability within each flight was found to be ±10%). The sensitivity of the instrument to other organics was broadly estimated based on possible numbers of carboxyl, hydroxyl and hydroperoxide groups. Species co-measured by the PTR-MS and the HRToF-CIMS are limited, preventing the direct comparison of the aircraft and surface data. More details of how the HRToF-CIMS and PT-RMS data were harmonized and used for modeling are outlined in Section 2.2.

2.1.3 - CHOICE OF INCLUDED DATA AND ANALYSIS DAYS

To mitigate the influence of horizontal inhomogeneities in gas-phase and aerosol properties, only the ascending or descending sections of each flight path around the SGP ground site were used in this study to gain vertical-profile information on particles and precursor vapors. Despite only using the ascending and descending parts of the flights, we cannot fully discount the influence of localized emission sources (e.g. plumes from power plants, fire, or urban emissions) on our results. IOP2 had more constant-altitude transects in the middle of the mixed layer than IOP1 (Fast et al., 2019), which limited the available data for that period. Additionally, to limit the influence of urban emissions from Bartlesville and airport traffic, the takeoff and landing portions of each flight were not used. This approach limited the number of flights (discussed next) that could be adequately analyzed since many flight paths were largely horizontal. It should be noted that we largely ignore the horizontal variations in flight paths as we are assuming that NPF is

taking place regionally; however, some limitations of this assumption will be discussed in the results section and in Section 3.3.

In order to adequately constrain our modeling approach, we required data from the ground-based PTR-MS, SO_2 analyzer, the AOS SMPS system, and ACSM, in addition to HRToF-CIMS, CPC, and environmental-variable data from the aircraft. In conjunction with the flight-path constraints, only 4 NPF events (27 April, 28 April, 11 May, and 14 May 2016), all in IOP1, had sufficient data for our analysis. Further, we analyze two days without apparent NPF events detected at the surface (16 May and 19 May 2016) that meet these measurement criteria to aid in testing model fidelity.

2.2. METEOROLOGICAL DATA

Meteorological data used in this work included the height of the developing mixed layer, downwelling shortwave irradiance, temperature, and RH. We tested multiple data products for temperature, RH, and the height of the mixed layer for comparison and robustness; discussion on how the temperature, RH, and mixed layer height data were used in our model simulations is in Section 2.3.4. The height of the developing mixed layer was provided from radiosonde retrievals using the methods from Liu and Lang (2010), from doppler lidar retrievals at the SGP site, and from the MERRA-2 reanalysis dataset (Figure S2). Radiosondes were launched from the SGP site at 05:30, 11:30, 17:30 and 23:30 UTC (00:30, 06:30, 12:30, and 18:30 CST), giving the top of the mixed layer height at 6 h intervals. The doppler lidar product provided estimates of the mixed layer height every ten minutes. The final mixed layer height estimate was from the MERRA-2 reanalysis product which provided mixed layer depths every 3 h at 36.0° N 97.5° W, slightly departed from the SGP ground site. Broadband shortwave irradiance was provided from a value-added product derived from three radiometer systems located at the SGP central facility (Long, 2002).

Temperature and RH data were measured onboard the G-1 aircraft and on the radiosondes, giving some vertical information. Temperature and RH were also measured at the surface. Finally, the MERRA-2 reanalysis product provides 3 h temperature and RH data at 72 hybrid-sigma levels extending from the surface to 0.015 hPa.

2.3. MODELS

2.3.1 - SOM-TOMAS

In this work, we use a one-dimensional (column) model, SOM-TOMAS, which is a coupling of the Statistical Oxidation Model of organic chemistry (SOM; Cappa and Wilson, 2012) with the Two Moment Aerosol Sectional microphysics model (TOMAS; Adams and Seinfeld, 2002; Pierce and Adams, 2009a,b; Riipinen et al., 2011). SOM-TOMAS allows for the representation of semi-explicit gas-phase chemistry and partitioning thermodynamics coupled to kinetic aerosol microphysics. SOM-TOMAS has been used to model chamber studies of SOA formation in laboratory experiments (He et al., 2020, 2021 2022; Akherati et al., 2020; Garofalo et al., 2021), as well as organic aerosol (OA) evolution in biomass burning plumes (Akherati et al., 2022). For this work, we have expanded SOM-TOMAS into a vertical one-dimensional framework in order to represent the chemistry, aerosol dynamics, and mixing in the PBL.

The basic architecture of SOM is a two-dimensional carbon and oxygen grid that is used to track the multigenerational oxidation chemistry, thermodynamics, and gas-particle partitioning of SOA precursors and their oxidation products. SOM is coupled to the SAPRC-11 chemical mechanism (Carter, 2010; Jathar et al., 2015) which explicitly represents the gas-phase reactions of the precursor species measured by the PTR-MS (isoprene, trimethylbenzene isomers, benzene, xylenes, toluene, and monoterpenes) with the hydroxyl radical (OH). Reactions between the

precursor species and other oxidants (e.g. ozone) are ignored for simplicity (and OH concentrations are scaled based on changes in OA mass - discussed later). Ignoring reactions with oxidants, such as ozone and nitrate radical (NO_3), could potentially reduce the relative contribution of isoprene and monoterpenes, which react quickly with ozone, to the SOA mass; however, these species still generally dominate our simulated SOA production in our scaled-OH approach. The SAPRC-11 mechanism also includes the production of sulfuric acid from the reaction of SO_2 with OH. The oxidation products from the organic precursor reactions are assigned to one of five carbon-oxygen grids used within SOM that are representative of five compounds or compound classes: benzene, toluene, xylenes, isoprene, and *a*-pinene. Additionally, reactions between the organic precursor species and OH create HOMs (more details in the following paragraph); the HOMs do not enter a SOM grid, and they are assumed to be non-volatile and non-reactive. Each carbon-oxygen grid cell emulates the average properties (e.g., volatility) of all organics species with the corresponding number of carbon and oxygen atoms. For each precursor class, the model utilizes parameters to simulate SOA formation, as described later, determined from fitting to chamber experiments (Akherati et al., 2020; He et al., 2022) with the parameters used here given in Table S1. The molecular weight of each species in the grid is given by the formula $C_{Nc}H_{2*Nc+2-No}O_{No}$ where *No* is the number of oxygen atoms and *Nc* is the number of carbon atoms in the molecule. The molecular weight formula assumes that oxygen atoms have a single covalent bond to the carbon backbone and the remaining valence electrons bond with hydrogen. HOMs are assumed to have a molecular weight of 300 g mol^{-1}, representative of larger, low-volatility, HOMs (e.g., $C_{10}H_{16}O_{10}$; Peräkylä et al., 2020).

Each SOM grid has 6 pre-fitted parameters (outlined in Table S1) that track the movement of species through the grid (Bilsback et al., in prep). The ΔLVP (logarithmic change in vapor

pressure) value determines the associated reduction in volatility with the addition of one oxygen atom. The P1, P1, P3, and P4 values are the molar yields of the functionalized products with either one, two, three, or four oxygen atoms added to the existing molecule, respectively. mFRAG is a tunable parameter that dictates the probability of fragmentation (P_{frag}). P_{frag} is defined as $P_{frag} = (N_O : N_C)^{mFRAG}$. The volatility (C*) of the species in each grid cell is determined by $C^* = 10^{(-0.0337 * MW\_hc + 11.56 - No * \Delta LVP)}$, where MW_hc is the molecular weight of the hydrocarbon backbone (including only the carbon and hydrogen atoms). Finally, f_{HOM} is the yield of HOMs formed directly from the reaction of precursor species with OH. f_{HOM} yields for SOA precursors in this work are based on yields compiled in Bianchi et al. (2019). Again, for this work, HOMs are considered to be completely non-volatile and non-reactive.

TOMAS is set up as 40 logarithmically spaced, mass-doubling size bins that represent the dry diameter of particles in the 1.0 nm to 10 μm range. The total number of particles and the mass of sulfuric acid, water, and each of the particle-phase organic species from SOM are tracked within each size range. TOMAS represents the changes in particle number and species mass concentrations in each size bin due to (1) nucleation, (2) coagulation, (3) irreversible condensation of sulfuric acid and HOM vapors, and (4) reversible condensation/evaporation of organic species within the SOM carbon-oxygen grid. Condensation/evaporation rates are size, volatility, and particle-phase-diffusivity dependent following He et al. (2021) TOMAS simulates the coagulational loss and growth of particles between and within each size section. Numerical details of the condensation and coagulation routines can be found in Adams and Seinfeld (2002). As there was an abundance of gas-phase ammonia observed on our simulated days, we assume that all sulfate is ammonium sulfate. The median nitrate and chloride concentrations measured by the

ACSM were 0.122 [μg m^{-3}] and 0.008 [μg m^{-3}] respectively, significantly lower than sulfate and organic concentrations, so we do not consider these species in our modeling (Liu et al., 2021).

The inorganic NPF rates are from Dunne et al. (2016), and the organic-sulfuric acid NPF rates are from Riccobono et al. (2014) with the inclusion of the temperature-dependent adjustment from Yu et al. (2017b). The organic-sulfuric acid nucleation scheme includes sulfuric acid and low-volatility organic clusters, which are assumed to be composed solely of HOM vapors. We tested our model with 1%, 10%, 20%, and 100% of the gas-phase HOMs contributing directly to organic-sulfuric acid nucleation (Figure S3) and found that 10% of HOMs participating in organic-sulfuric acid nucleation agreed well with observations. Assuming 10% of HOMs participating in organic-sulfuric acid nucleation may align with previous work from Lehtipalo et al. (2018), who had only HOM dimers participating in organic nucleation. Hence, our base simulation assumed that 10% of HOMs contribute to organic-sulfuric acid nucleation, but we show sensitivity simulations using other HOM fractions for nucleation. The inorganic nucleation scheme represents, both neutral and ion-induced, binary (sulfuric acid-water) and ternary (sulfuric acid-ammonia-water) nucleation, although the RH (H_2O) dependence is not included in this scheme. For the ion-mediated inorganic NPF schemes, we used an ion-recombination coefficient of 8.0 cm^{-3} s^{-1}, which is representative of the lower troposphere (Franchin et al., 2015; Zauner-Wieczorek et al., 2021). Output from the organic-sulfuric acid and inorganic NPF schemes are recorded in addition to the total nucleation rate. Nucleated particles are assumed to have diameters of 1 nm and are added to the smallest size bin in TOMAS.

Previous versions of SOM-TOMAS (Akherati et al., 2020; He et al., 2020, 2021, 2022; Garofalo et al., 2021) were zero-dimensional (i.e., a single box); however, we have updated SOM-TOMAS to represent a one-dimensional vertical column. The version of SOM-TOMAS used in

this work consisted of 20 vertical pressure levels between 700 hPa and the surface that are linearly spaced in pressure coordinates (i.e., same mass of air in each box). For this work, we assumed that rapid vertical mixing of aerosol particles and gas-phase species takes place only within the mixed layer, and not in the residual layer or free troposphere. Details of how the mixed layer heights are used in the model can be found in Section 2.3.4. In our base simulations we assumed a diffusional mixing coefficient (K_Z) of 2000 $m^2 s^{-1}$ in the mixed layer (Du et al., 2020; Lai et al., 2022). We also tested K_Z values of 500 $m^2 s^{-1}$, 75 $m^2 s^{-1}$, and 0.0 $m^2 s^{-1}$ (see vertical sensitivity cases). Our assumption of a constant vertical diffusivity coefficient within the mixed layer is a limitation of this work, as the rate of vertical mixing in the mixed layer is largely tied to the intensity of insolation as well as synoptic weather patterns. Additionally, our assumption of a simple mixed layer is a limiting factor of this work, as other studies (e.g. Schobesberger et al. 2013) have found enhancements of ultrafine particles at several levels within the mixed layer. In this study, water vapor does not mix vertically in the model, and the vertical profiles of RH are derived from the MERRA-2 specific humidity reanalysis data product (Section 2.3.4) in order to resolve the diurnal cycle and maintain consistency between the coupling of temperature and RH. We do not consider the deposition of gas- and particle-phase species in this study, which is a limitation of this work; however, dry deposition is likely to have only a small effect (<5%) on our results (Hodzic et al., 2013, 2016). We also do not consider emissions of primary aerosol particles (e.g. dust, biomass burning, and vehicle exhaust).

Table 1. Gas-phase species inputs for the surface layer of the model for each simulation day. Also included are the initial condensation sink (CS) values at the surface and the OH scale factor used in the base simulation.

Species [ppb]	April 27	April 28	May 11	May 14	May 16	May 19
SO_2	0.241	0.246	0.277	0.275	0.243	0.296
Benzene	0.028	0.029	0.017	0.011	0.004	0.022
Trimethyl -benzene	0.011	0.012	0.046	0.026	0.032	0.006
Toluene	0.029	0.033	0.047	0.024	0.084	0.070
Xylenes	0.083	0.041	0.012	0.013	0.057	0.008
Isoprene	0.079	0.046	0.132	0.048	0.136	0.011
Terpenes	0.039	0.014	0.005	0.005	0.019	0.003
NH_3	5.0	5.0	5.0	2.0	0.3	0.3
1/CS [min]	12.07	22.37	8.59	17.47	4.00	4.38
OH scale	0.9016	0.4888	0.9800	1.3114	1.7403	0.3258

2.3.2 - INCORPORATING GAS-PHASE OBSERVATIONS IN THE MODEL

For all of the days simulated, the SO_2 and organic species measured by the PTR-MS showed little or no change throughout the simulation period; therefore, we held the column abundance of each gas-phase species in Table 1 fixed throughout each model run (i.e., these parent species are not removed through chemical reactions), but the species do mix vertically. This formulation was done to allow for the vertical mixing of the species while conserving the total column concentration and keeping surface concentrations roughly constant. Emissions of gas-phase species are not represented in the model; thus, simulations that allowed the precursor species to be chemically removed via reactions with OH led to many of the species to be rapidly depleted

(to ~0.0 ppbv), inconsistent with observations. Additionally, NH_3 concentrations were measured by the HRToF-CIMS while operating in 'positive mode' for short periods of time. We estimated the NH_3 concentrations for each day based on the available data (Table 1), and we assumed a constant vertical profile of NH_3 mixing ratios for each day. We also assumed that the mixing ratio of NH_3 does not change during the simulation period. The constant vertical mixing ratio and the lack of depletion of NH_3 is a limiting factor in this work.

We tested several methods of obtaining initial vertical profiles of SO_2 and the six organic SOA precursors needed for the modeling (Table 1). This was done because of the limited species co-measured by the HRToF-CIMS aboard the G-1 aircraft and the PTR-MS at the surface. The HRToF-CIMS was operated in standard mode for all six analysis days chosen, and it was occasionally switched to 'positive mode' for relatively shorter periods of time during the four analysis flights in May. With the exception of 14 May, the isoprene and monoterpene data collected in 'positive mode' were sparse, with vertical profiles covering only several hundred meters of PBL. To derive full profiles of the organic species outlined in Table 1, we assumed that the relative-enhancements vertically of isoprene, benzene, and toluene followed the relative enhancements of two assumed products of isoprene oxidation ($C_5H_{10}O_3$ and $C_5H_{10}O_5$) measured by the HRToF-CIMS in standard mode. Similarly, we assumed that the relative enhancements of trimethylbenzene and its isomers, xylenes, and monoterpenes followed the relative enhancements of two 3-4 hydr(per)oxy group molecules ($C_9H_{14}O_4$ and $C_8H_{12}O_5$). This assumption provides separate vertical profiles for smaller (~C_5) and larger (~C_8) organic species, but the lumping of different precursors to two groups of oxidized molecules is a limitation of our work that will be discussed later. Previous work (Sprung et al., 2001) has found strong correlations between species (acetone and acetonitrile) measured using a PTR-MS and a CIMS instrument aboard an aircraft;

however, this work is not entirely comparable as the instruments were measuring the same species. The enhancement profiles of isoprene oxidation products and the 3-4 hydr(per)oxy group molecules were derived by dividing each vertical profile by the average concentration in the lowest 200 m of the profile (Figure S4). This was done so that the relative enhancements closest to the surface had a value of 1. The enhancement profiles were then extrapolated to the surface (i.e., vertical enhancements were equal to one from the surface to the lowest part of each profile). To initialize the species outlined in Table 1, the derived vertical enhancements were multiplied by the surface concentration of each species measured by the PTR-MS. For consistency, we employed the same technique using the SO_2 analyzer on the aircraft and the SO_2 instrument at the surface. This method may lead to erroneous concentrations of gas-phase organic species (and SO_2) in the column since we assumed no gradient between the surface and the lowest part of each profile (~500 m). We recognize the large uncertainties in using the oxidation products of certain species as a proxy for the parent species, and we also recognize the limitations in using the relative enhancements of isoprene oxidation products as a proxy for non-biogenic organic species. This is a limitation owing to not having the same instrumentation at the surface and aboard the G-1 aircraft. Comparisons of PTR-MS and CIMS instruments can be found in Riva et al., 2019.

2.3.3 - INITIALIZING AEROSOL SIZE DISTRIBUTIONS

We tested two methods of initializing the aerosol size distribution in SOM-TOMAS. The first method used a tri-modal lognormal fit of the merged SMPS aerosol surface area distribution for the 20-min average (~four samples) prior to detection of a NPF event at the surface. For this first method, all model levels were initialized with the fits to the ground-level merged SMPS data (accounting for volume, pressure, and temperature differences). The second method is the same as the first method within the initial mixed layer, above which, the initial aerosol size distribution

was set based on lognormal fits to the FIMS aerosol size distribution (Figure S5a-f). Using the FIMS data, we found little difference in the modeled NPF rate and aerosol growth rate at the surface; however, using the FIMS data often led to erroneous aerosol modes appearing at the surface after mixing down to the surface. Thus, we used the first method as part of our base simulation (see Section 3.2.1 for discussion). We found that fitting to the surface-area distribution led to the best agreement with both the observed aerosol mass and particle number distribution. It should be noted that the particle growth rates were calculated using the same method employed for the merged SMPS data.

The initial aerosol composition was set using the ratio of observed sulfate and total organic mass measured by the ACSM. We assumed that the initial aerosol size distribution was composed only of ammonium sulfate and organic material, and we assumed that the initial organic mass was completely non-volatile. Assuming the initial aerosols were non-volatile is a limitation of this work, as we will not capture potential evaporation of the initial aerosol particles as the mixed layer develops; however, the simulation periods generally coincide with an increase in aerosol mass loading observed by the ACSM (Figure S6). Note that the initial aerosol mass concentrations were set based on the SMPS-fit size distributions and assumed densities of 1770 and 1400 [kg m^{-3}] for sulfate and organics, respectively; hence, the initial mass concentrations in the model may not match those of the ACSM. Additionally, the ACSM only measures sulfate, ammonium, nitrate, chloride, and organic aerosol mass, while the merged SMPS would also include contributions from refractory species, such as fine-mode dust or soot.

2.3.4 - METEOROLOGY IN THE MODEL

We tested using observational and reanalysis temperature, RH, and mixed layer height data in the model. MERRA-2 temperature and RH data have a horizontal resolution of 0.5° lat x 0.625°

lon; therefore, we used data from 36.0° N 97.5° W. Typically, 15 MERRA-2 layers exist within the height of our 20 model layers; therefore, we linearly interpolate temperature and RH data between MERRA-2 vertical layers to avoid adjacent SOM-TOMAS levels artificially having the same values. Vertical profiles of temperature and RH data from the aircraft during the HI-SCALE campaign provided snapshots of the state of the atmosphere from ~500-2500 m; however, to better represent the diurnal changes in temperature and RH as well as data extending to the surface, we used data from the MERRA-2 dataset for our simulations. We also tested mixed layer height data derived from the radiosondes launched at the SGP ground site, doppler lidar, and the MERRA-2 dataset (Figure S2). Mixed layer height data from the radiosondes are reported every 6 hours, doppler lidar data are reported every 10 minutes, and MERRA-2 reanalysis provides data every 3 h. On most days, we found little difference between the MERRA-2 mixed layer height data and the radiosonde data; however, some days showed non-trivial differences in the mixed layer height, with MERRA-2 having a significantly higher mixed layer height on 16 May. Similarly, mixed layer heights from the doppler lidar, excluding even intermediate quality data, were unphysically variable, and many time periods lacked data altogether. Given the inconsistency of the MERRA-2 and doppler lidar mixed layer height data, we used mixed layer heights from the radiosondes for our modeling.

2.3.5 - HYDROXYL RADICAL CONCENTRATIONS

The OA production in SOM-TOMAS is sensitive to the OH concentrations; therefore, we tested three OH proxies with varying magnitudes and vertical fidelity, as well as scaling an assumed OH concentration to constrain the OA production rate to match observations (discussed in the following paragraph). The first OH proxy (Pietikäinen et al. 2014; hereafter OH-1) estimates OH from downwelling shortwave radiation only, and it predicted the lowest average maximum

OH concentrations of ~1×10^6 molec cm^{-3}. The second OH proxy (Stevens et al. 2012; hereafter OH-2) predicts OH from both downwelling shortwave radiation and NO_x concentrations. OH-2 had the highest average maximum OH concentrations of ~5×10^7 molec cm^{-3}. Both OH-1 and OH-2 provide no vertical information, so for these proxies, we applied constant OH concentrations vertically. Finally, we also used OH concentration output from the three-dimensional atmospheric chemistry model, GEOS-Chem (v12.9.3), run at 0.25°x0.3125° resolution in a nested-grid simulation over the central US (hereafter OH-3). The average maximum OH concentrations from GEOS-Chem were ~1×10^7 molec cm^{-3}, in the middle of the other proxies. Importantly, GEOS-Chem produced vertical profiles of OH concentrations, contrasting the two proxies. We generally found slightly increasing OH concentrations with increasing height within the mixed layer, and steadily decreasing OH concentrations in the residual layer and free troposphere. OH concentrations at the surface from each proxy for each day can be found in the supplementary material (Figure S7). As mentioned earlier, we do not consider ozone chemistry in our simulations; while we scale OH to match observed OH changes (below), we recognize this as a potential limitation of this work.

The OA production rate is sensitive to the OH concentration in the model. To better match the observed OA change during the simulation periods, we scaled the OH-3 concentrations for each day by the ratio of the observed OA production rate (ACSM) to the modeled OA production rate using the original OH-3. The scale factors are listed in the last row of Table 1, and the scaled OH concentrations at the surface are shown in the supplementary material (Figure S7). Scaling the OH concentration led to the best agreement between observed and modeled aerosol mass concentrations; however, the aerosol particle number concentrations showed mixed results with this approach (see results). It should be noted that observed OA changes are often partially

attributable to changes/variability in advection over the SGP site, and this was not accounted for in this work. Additionally, scaling the OH concentrations in this way assumes a linear relationship between the OA production rate and OH concentrations, which may not be strictly correct. We used the simulations with scaled OH in our base simulations, from which we tested a variety of other uncertainties and model sensitivities (discussed later).

2.3.6 - MODEL UNCERTAINTY ANALYSIS

In order to best match the observations of NPF during HI-SCALE using the SOM-TOMAS model, we tested a variety of uncertain inputs to the model. Our goal was to test the model sensitivity to OH concentrations, particle-phase diffusivity (or viscosity), and fraction of HOMs contributing to organic-sulfuric acid nucleation, from which we derived our base simulation (bolded combination of variables as shown in Table 2: *Model Uncertainties*). As previously described, we tested three different OH concentrations in the model in addition to scaling OH to match the observed OA production rate. We also tested several particle phase diffusivity coefficients (D_b) that represented liquid to semi-solid aerosol particles He et al., 2021; Zaveri et al., 2014, 2018; Reid et al., 2018; Manabu et al., 2017). We found that representing the particles as semi-solid ($D_b = 10^{-20}$ cm^2 s^{-1}) gave the best agreement with observations, so this is used as a base assumption with sensitivities (discussed later). As previously stated, we also tested assumptions about the fraction of HOMs contributing to organic-sulfuric acid nucleation, and we found that assuming that 10% of HOMs directly contributing to organic-sulfuric acid nucleation led to the best agreement with observations, so this is our base assumption.

Table 2. Outline of the different model uncertainty simulations (top section) and the vertical sensitivity simulations (bottom section). The parameter being changed is in the left column, a description of the sensitivity simulation is in the middle

column, and the difference values (if applicable) are in the right column. Bold values denote the values in our base simulations.

Model Uncertainties

Parameter/Name:	Description:	Values:
OH	OH-1 - Pietikäinen et al., 2014 OH-2 - Stevens et al., 2012 OH-3 - GEOS-Chem output **'Scaled' - GEOS-Chem output scaled to match the observed OA production rate**	
HOM	Percent of HOMs contributing to organic-sulfuric acid NPF	1% **10%** 20% 100%
D_b	Particle phase diffusivity coefficient	1×10^{-10} cm^2 s^{-1} 3×10^{-19} cm^2 s^{-1} **1×10^{-20} cm^2 s^{-1}**

Vertical Sensitivity Analysis

Parameter/Name:	Description:	Values:
K_Z	Vertical turbulent diffusivity	0 m^2 s^{-1} 75 m^2 s^{-1} 500 m^2 s^{-1} **2000 m^2 s^{-1}**
RH	Relative humidity	**MERRA-2** 50%
$T_{nucleation}$	Temperature used in the nucleation routine	**MERRA-2** Surface Temperature
T_{C^*}	Temperature used in the organic species volatility calculation	**MERRA-2** Surface Temperature
Const. Prec.	Initial vertical profile of gas-phase species in Table 1	Constant **Observations**

2.3.7 - VERTICAL SENSITIVITY ANALYSIS

Additionally, we ran a series of sensitivity simulations to elucidate contributors to the vertical profile of NPF and growth in the model (Table 2: *Vertical Sensitivity Analysis*). We tested the sensitivity of our model results to the vertical profile of vertical turbulent diffusivity, RH,

temperature dependence of the nucleation routines, the temperature dependence of the volatility calculation for the organic species in the SOM grid, and the height of the developing mixed layer. During HI-SCALE, RH generally increased with height within the mixed layer, and then decreased significantly in the residual layer and free troposphere. To understand how this vertical profile and diurnal cycle of RH affects the model results, we set the RH for all levels in the model to 50% for the duration of the simulation. We tested the influence of the vertical mixing rate by running the model with slower mixing timescales (K_Z = 500 m^2 s^{-1}, and K_Z = 75 m^2 s^{-1}) as well as no vertical mixing (K_Z = 0 m^2 s^{-1}). The influence of the temperature dependence in the nucleation routines on the model results was tested by setting the temperature in the nucleation routines at all levels in the model to the surface temperature. Lower temperatures favor NPF, therefore, our goal was to test how temperature contributes to faster nucleation at higher altitudes. Similarly, we tested the influence of temperature on the volatility of organic species by, again, setting the temperature at all model levels to the surface temperature for the volatility calculation. This tested for enhanced new-particle growth with altitude due to colder temperatures. We tested initializing all model levels with the surface mixing ratio of the gas-phase species outlined in Table 1. The goal of this vertical sensitivity simulation was to understand how the initial vertical profiles of gas-phase species derived from HI-SCALE data influences the results at the surface. Finally, we tested the influence of the developing mixed layer height on the surface aerosol size distribution by imposing a constant mixed layer height throughout each simulation. For the fixed mixed layer simulations, we used the average height of the mixed layer during each simulation period, leading to higher mixed layer heights early in the simulation and lower heights later in the experiment, relative to the base simulation.

2.3.8 - HYSPLIT

To assess the recent influences on the air masses associated with the four NPF events observed at the surface and the two non-NPF events, we ran 48 h back trajectories using the HYbrid Single-Particle Lagrangian Integrated Trajectory (HYSPLIT) model (Draxler and Rolph, 2012; Rolph, 2012). We ran 24 ensemble back trajectories using North American Model (NAM) meteorology initialized 10 m above the surface at the SGP site for all six analysis days. Additionally, to assess the origin of observed enhancements of gas-phase species and aerosol particle number by the aircraft, we ran 48 h back trajectories initialized at 10, 500, and 2000 m above the SGP site. This second set of HYSPLIT trajectories can be found in the supplementary material (Figures S5).

CHAPTER 3

RESULTS

3.1 NPF DURING HI-SCALE

3.1.1 - OVERVIEW OF SURFACE OBSERVATIONS FROM 4 NPF EVENTS AND THE 2 NON-NPF EVENTS DURING IOP1

During HI-SCALE IOP1, we identified a total of 8 significant NPF and growth events at the surface; however, as previously stated, our analysis focuses on four days (27, 28 April and 11, 14 May), with concurrent aircraft flights and complete data, as well as two non-nucleation days with flights and complete data (16, 19 May). Figure 2 shows the ground-based aerosol size distributions for the four NPF-events days and the two non-NPF days in addition to the ensemble HYSPLIT back trajectories initialized at 10 m above the surface at SGP. The aerosol size distributions for 27 April, 28 April, and 14 May show typical NPF and growth events, with the exception of 27 April which shows interrupted growth early in the event. The condensation sink prior to the detection of NPF for each was 1.38×10^{-3}, 7.45×10^{-4}, and 9.54×10^{-4} [s^{-1}] for 27 April, 28 April, and 14 May, respectively. The air masses on 27 and 28 April and 14 May largely originate from the north in the 48 hr prior to arriving at the SGP site. These air masses were modeled to have spent most of the previous 48 hr within 1000 m of the surface. Air masses approaching from the north largely pass over grass and cropland (Trishchenko et al., 2004), and are therefore associated with weaker biogenic emissions than air masses associated with forested areas and likely had minor urban influence.

Conversely, for the 11 May NPF day, the air mass largely arrived from the south, having been at the Gulf coast of Texas 48 hours prior to the NPF event. The 11 May air mass passed over the SGP observatory the night before the NPF event and then shifted from a northward to a southward trajectory to then arrive again at the SGP site at 18:00 UTC (13:00 CDT). These trajectories were estimated to be within 500 m of the surface during the 48 hr prior to arrival. These air masses may have been more influenced by anthropogenic emissions from cities like Houston and Oklahoma City than the three trajectories from the north discussed above. However, the concentrations of potentially anthropogenic gases (e.g., SO_2, benzene) are not clearly enhanced over the other study days (Table 1). The NPF and growth event on 11 May shows some particles appearing at larger sizes (~10 nm), indicating that the initial particle formation and growth occurred either elsewhere at the surface or aloft and then mixed down (hence, it is possible that the anthropogenic influence may be limited to the residual layer). 11 May had the largest condensation sink of 1.94×10^{-3} [s^{-1}] prior to the detection of the NPF event.

On the two non-NPF days (16 and 19 May), the back trajectories are similar to each other, both arriving at SGP from the east, having passed through Missouri and Arkansas in the previous 48 hours, generally staying within 500 m of the surface. The regions to the east of the SGP observatory are generally more forested and may have larger biogenic influences compared to the air masses originating from other directions, but the monoterpenes and isoprene concentrations in Table 1 do not clearly show this. It should be noted that 16 May coincided with the passage of a warm front over the SGP observatory, and both 16 and 19 May had substantial cloud cover that likely contributed to suppressed mixed layer photochemistry and NPF. These two days both had a prevalent pre-existing accumulation ($D_p \approx 0.1$-1.0 μm) mode leading to larger condensation sink values (4.16×10^{-3} and 3.80×10^{-3} for 16 May and 19 May, respectively) than the nucleation days

(Table 1) and acting to suppress nucleation. The ground-based particle size distribution on 19 May also showed potential influences of a smoke or emission plume in the afternoon, indicated by the enhanced number concentration of Aitken mode ($D_p \approx$ 10-100 nm) particles around 16:00 CDT. These two non-NPF event days also had lower observed NH_3 concentrations (Table 1).

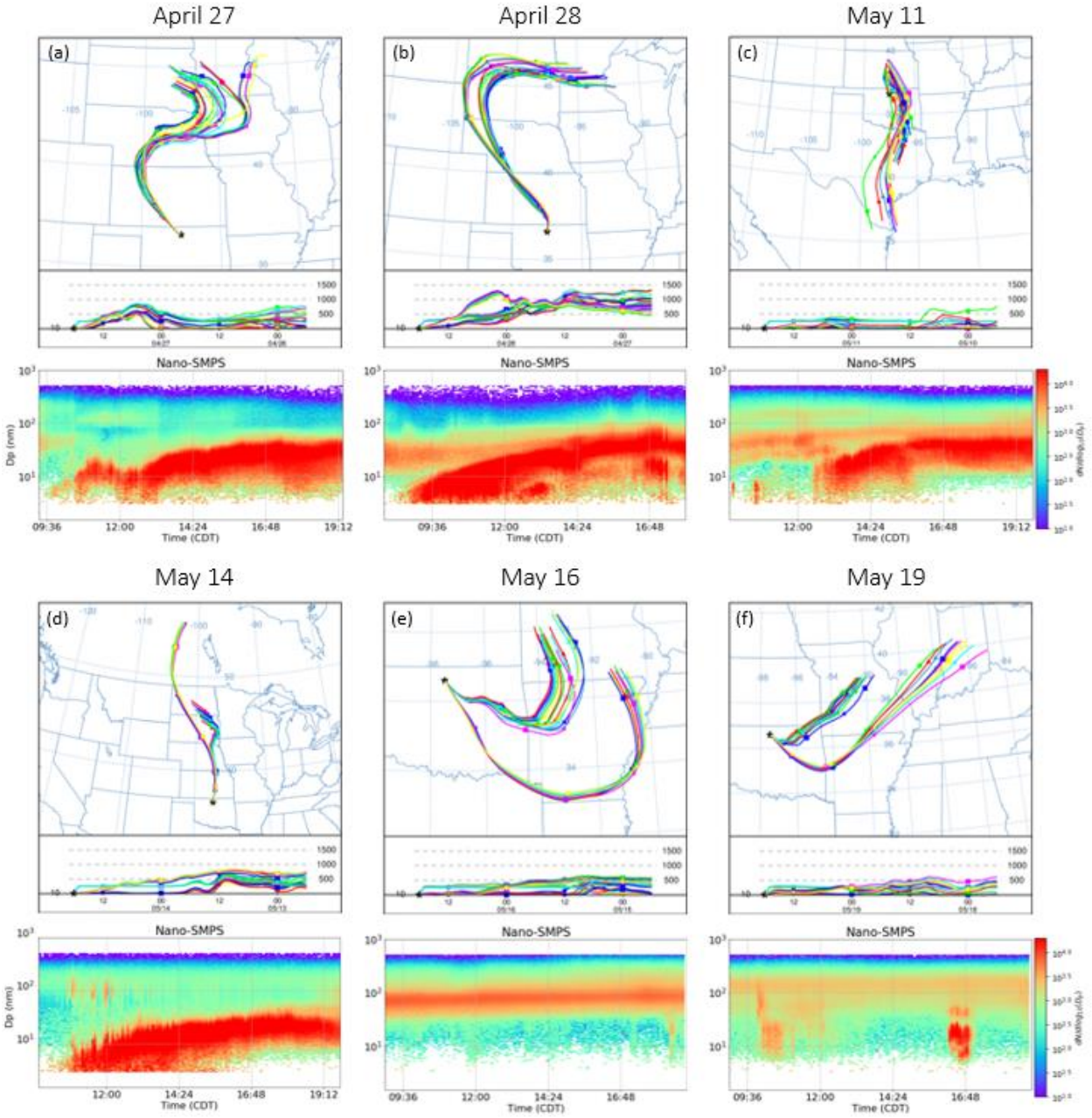

Figure 2. (a-f) 48 h ensemble HYSPLIT back trajectories using NAM meteorology initialized at 18:00 UTC (13:00 CDT) 10 meters a.g.l. at SGP (top panels). The SGP ground site location is denoted by the black star. (a-f) bottom panels show the aerosol size distributions measured by the merged SMPS at the SGP observatory for the four NPF events (a-d) and the two non-NPF events (e-f).

3.1.2 - EVIDENCE FOR NPF EVENTS OCCURRING ALOFT DURING HI-SCALE.

During the four NPF events analyzed here (Figure 2), we found NPF occurring at a variety of vertical layers (sometimes shallow) within the mixed layer and the residual layer. Figure 3 shows the vertical profiles of the total number concentration of particles with diameters between 3-10 nm derived from the two airborne CPCs. The observed NPF is largely occurring within the mixed layer (as measured by the radiosondes) and sometimes within the residual layer; however, the exact location of the mixed layer top, and thus the residual layer bottom, is variable depending on the mixed layer height estimate method (Figure S2). Additionally, NPF observed by the aircraft often illustrated strong horizontal inhomogeneities (Figure S8). We found a significant enhancement in 3-10 nm particles on 11 May (Figure 3(c), orange line) in the residual layer (Figure S8c) upwind of the SGP observatory. This enhancement was observed after the NPF event was detected at the SGP observatory; however, the 11 May merged SMPS data (Fig. 2(c)) show that the aerosol particles appear at diameters of ~10 nm, indicating the onset of NPF was not fully captured at the SGP observatory. Similarly, the NPF observed by the aircraft on 14 May indicates the potential influence of a plume, potentially from the 1138 megawatt Redrock Power Plant (36.45°N, 97.05°W; Liu et al., 2021; Fast et al., 2019), due to the steep horizontal and vertical gradients of ultrafine particles (Figure S8d). Finally, Figure 3 (e-f) shows that the two non-NPF event days show little NPF at any level in the lower troposphere. Overall, the strongest observational evidence for regional NPF initiating aloft is on 11 May with little direct

observational evidence on other days, which may be partly due to the challenge of timing aircraft vertical profiles with NPF initialization.

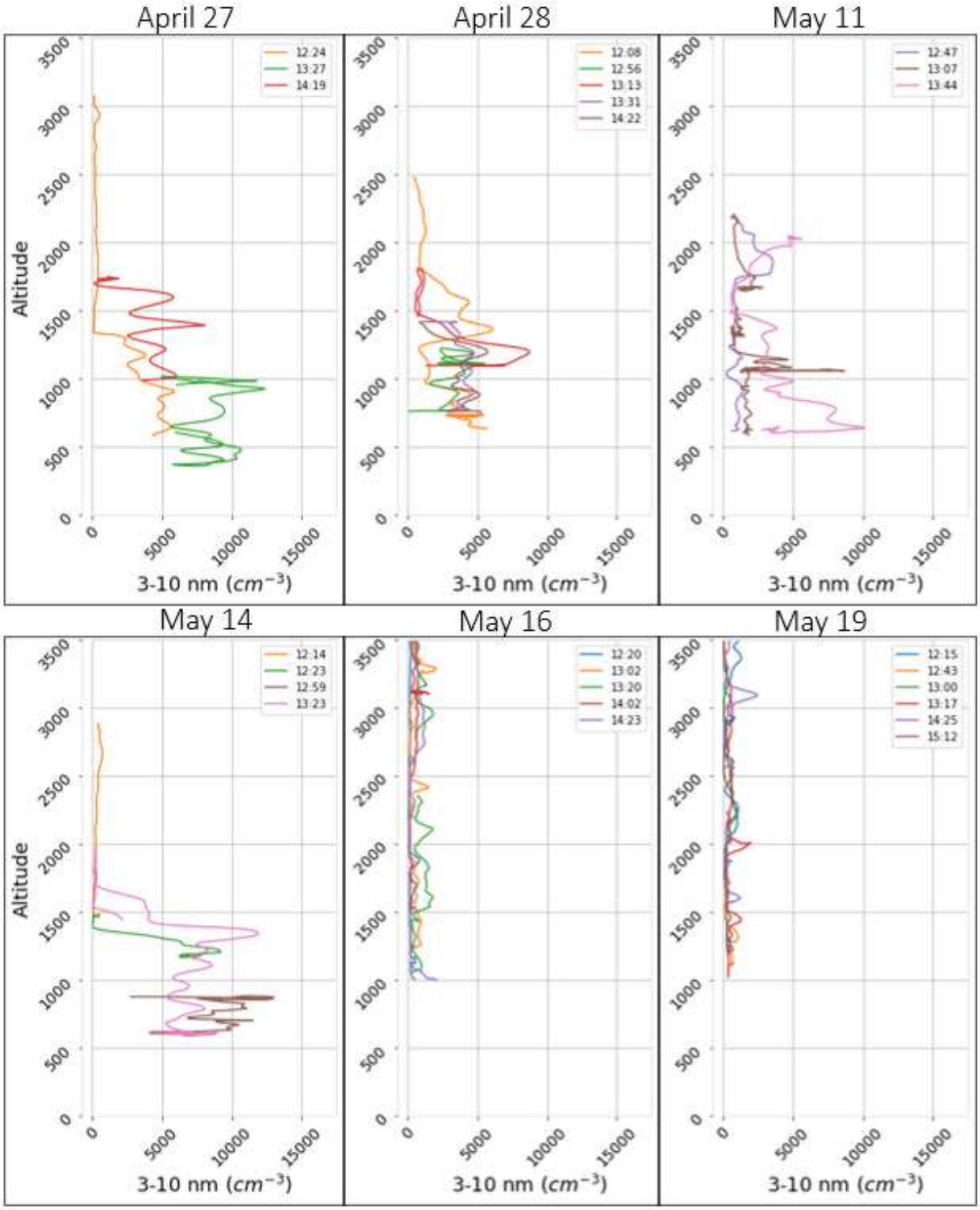

Figure 3. Vertical profiles of the particle number concentrations in the 3-10 nm diameter range derived from the two CPCs during selected ascending and descending transects of the flights on the four NPF event days (a-d) and the two non-event days (e-f). Transects selected are those closest to the onset of the NPF event. The aircraft often measured the NPF events well after the event was detected at the surface, leading to profiles of 3-10 nm particle number concentrations with little information about the onset of NPF; therefore, these profiles were excluded from these figures. Times listed correspond to the time at the beginning of each vertical transect in CDT. Horizontal dashed lines correspond to the average height of the mixed layer during the vertical transect. The colored 'X's at the bottom of each plot correspond to the average number concentration of particles in the 3-10 nm diameter range measured by the merged SMPS at the surface.

Each analysis day had different vertical profiles of organic and inorganic gas-phase species; however, most days had some vertical level that had substantially higher concentrations of organic or inorganic species than the surface (based on our method of connecting the airborne gas-phase measurements to the surface; Figure S4). From our analysis using the HYSPLIT model, we cannot elucidate the specific influences that near- versus far-field sources had on the observed profiles. We conclude, however, from back trajectory initiated at 2000 m above the SGP site, that the air mass with enhanced gas-phase organics, SO_2, and aerosol mass observed between 2500 and 3000 m on 28 April may have originated from close to ground level in Texas 48 h prior to arrival at SGP (Figure S5). The sulfate-rich aerosol in this air mass originating from the south aligns with the observations from Liu et al., (2021), who found a larger sulfate aerosol fraction in air masses originating from Texas, indicating that the observed enhancements are perhaps not attributable to power plant or urban emissions close to the SGP observatory. In contrast, other flights (e.g. 14 May; Figure S8d) appeared to intercept power plant plumes or urban emissions from surrounding cities. The direct influence of these localized sources on observations at the SGP observatory are out of the scope of this study.

3.2. MODEL RESULTS

3.2.1 - MODEL RESULTS OF NPF EVENTS AND NON-NPF EVENTS AT THE SURFACE

SOM-TOMAS is largely able to represent the observed NPF, particle growth, and organic aerosol (OA) production rate across the four NPF days. Figure 4 (a-d) shows the aerosol size distributions from the surface model layer (top panels) and from the merged SMPS surface measurements (bottom panels) for the four NPF events analyzed. The black horizontal dashed lines indicate the diameter corresponding to the mode that nucleated particles have grown to. From Figure 4, we see that the surface model layer of SOM-TOMAS predicts the observed particle diameters, after several hours of growth, to within ~10 nm for all four NPF events. Further discussion on the particle growth rates and aerosol number concentrations can be found later in this section. On 27 April, 28 April, and 14 May, particles appear in the smallest mode and in the merged SMPS observations, indicating nucleation and early particle growth is occurring in the lowest model level and at the surface at the SGP observatory, respectively. Conversely, the model and the merged SMPS observations on 11 May show particles appearing at larger sizes at the surface, indicating that nucleation and early particle growth is occurring elsewhere in the model domain and atmosphere, respectively. The details of the vertical profiles of NPF and early particle growth in the model will be discussed in Section 3.2.2. Figure S6 (a-d) compares the modeled sulfate and total organic mass to corresponding observations by the ACSM on the four NPF event days. Since the OH concentrations in SOM-TOMAS were scaled based on the observed OA production rate, the model reasonably predicts the observed changes in OA mass during the simulation periods. We found that the OA mass produced came from a range of precursors (Figure S9), with no one precursor class dominating the changes in OA mass.

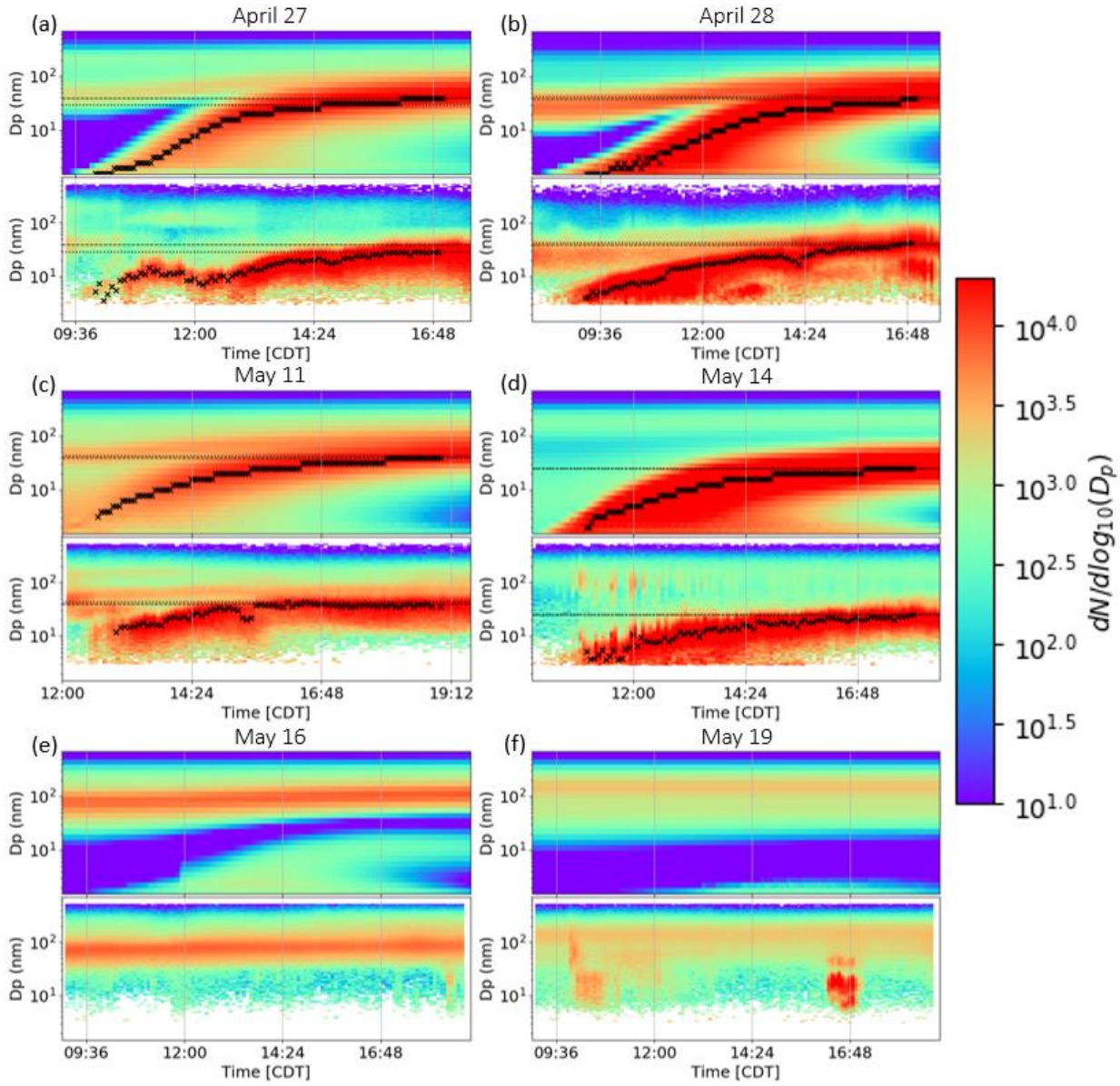

Figure 4. (a-f) Comparisons of the simulated and observed aerosol size distributions. For each panel (a-f), the top figure shows the resultant size distribution from the base simulation in SOM-TOMAS, and the bottom figure shows the aerosol size distribution measured by the merged SMPS at the SGP observatory. (a-d) The black x-markers indicate the maximum of the size distribution at the corresponding time, and the horizontal dotted lines indicate the diameter of the last black x-marker.

For the two non-NPF-event days, SOM-TOMAS predicts weak NPF and growth (Figure 4e,f; growth rates are not calculated for the non-NPF event days). Several factors contributing to

the prediction of weak NPF and growth on 16 May will be discussed in later sections. In short, 16 May had the highest OH concentrations due to the high OH scale factor (Table 1) based on the increase in OA mass observed by the ACSM (Figure S6e). The observed OA mass increase is likely due to an air mass change associated with the passage of a warm front over the SGP observatory on 16 May; hence, the high OH concentrations used in the model to match the OA increase are likely too high. The model results from 16 May highlight the complications of potential airmass changes when simulating nucleation events at an observation site with a fixed-location model, scaling OH by the OA production rate and not accounting for air mass changes. Additionally, 16 May had the second-highest monoterpene concentrations at the surface of any analysis day (Figure S1), promoting HOM production and organic-sulfuric acid nucleation in the model. On 19 May, low number concentrations of nucleation mode particles appear in the smallest model bins, but these nucleated particles do not grow beyond ~10 nm and are mostly scavenged by existing aerosol particles.

3.2.2 - ANALYSIS OF UNCERTAIN MODEL PARAMETERS

Figure 5a shows a comparison of the modeled and observed particle growth rates for the four NPF days at the surface. The base simulation, indicated by the black markers, used OH from GEOS-Chem that was scaled by the values outlined in Table 1. Overall, the base simulation overpredicts the particle growth rate by around 50% on 27 April, 11 May, and 14 May, but underpredicts the growth rate by about 40% on 28 April. Figure 5a also includes the model results from using the other three unscaled OH proxies, where OH-1 (low OH) and OH-2 (high OH) are based on downwelling irradiance and OH-3 is the raw OH output from GEOS-Chem (not scaled to match observed OA changes). Using OH-1 led to higher growth rates than the base simulation for all days, with the exception of 14 May, which had identical growth rates to the base simulation.

Similarly, OH-2 yielded growth rates that were higher than the base simulation for all days, likely due to the magnitude of the OH concentrations and potentially highlighting the importance of the vertical OH information provided by the GEOS-Chem output. We found that the GEOS-Chem output used in the OH-3 and the base simulations generally has lower OH concentrations in the residual layer; therefore, the OH-2 proxy overpredicts the OH concentrations in the residual layer, which may partially contribute to the higher growth rates. Finally, using OH-3, the unscaled OH from GEOS-Chem, led to better agreement with observations than the base simulation of particle growth rates; however, comparing other metrics, such as OA production and particle number concentration, OH-3 shows worse agreement with observations than the base simulation.

Figure 5b shows the comparison of the modeled and observed aerosol particle number concentrations for the four event days at the surface (note: particle number concentrations are compared at the time of the last black 'x' for each day in Figure 4). The relationship between particle number concentration and OH concentration seems more straightforward than that of OH with growth rates, with higher OH concentrations generally leading to higher particle number concentrations. The base simulation, using scaled GEOS-Chem OH, underpredicts the particle number concentration on 27 April, 28 April, and 11 May, but overpredicts the number concentration on 14 May (opposite of the growth rates). Using OH-1 yields higher number concentrations than the base simulation on 28 April and 14 May, but lower number concentrations on 27 April and 11 May. Using OH-2 led to higher particle number concentrations than the base simulation for all days except for 27 April, where using OH-2 led to lower particle number concentrations than the base simulation, despite OH-2 having the highest OH concentrations of any proxy for that day (Figure S7). Finally, using OH-3 led to higher particle number

concentrations than the base simulation on 27 April, 28 April, and 11 May, and slightly lower concentrations on 14 May.

Our base simulation assumes that 10% of HOMs are contributing directly to the organic-sulfuric acid nucleation scheme; however, we also tested 1%, 20% and 100% of HOMs participating in organic-sulfuric acid nucleation to understand the model sensitivity to this assumption. Figure 5 includes comparisons of the particle growth rates (5a) and particle number concentrations (5b) for the three HOM-sensitivity cases with observations, in addition to the base simulations. Additionally, Figure S3 shows the particle size distributions for each HOMs sensitivity case for all six analysis days. In general, increasing the fraction of HOMs contributing to organic-sulfuric acid nucleation leads to increased NPF rates and slower growth rates as there are more particles to distribute the condensable material onto (and the amount of condensable material produced does not change across these sensitivity simulations). The uncertainty in the amount of HOMs contributing to the organic-sulfuric acid nucleation scheme, along with the OH sensitivities already discussed, are the largest contributors to the uncertainties in the predicted nucleation and particle growth rates.

Through testing assumptions about the particle-phase diffusivity, we found that representing aerosol particles as our most-solid assumption ($D_b = 1 \times 10^{-20}$ cm^2 s^{-1}) led to the best agreement with observations. Figure S10 shows the particle size distributions from simulations with particle phase diffusivity coefficients of 1×10^{-10}, 3×10^{-19}, and 1×10^{-20} (base simulations) cm^2 s^{-1}. Assuming particles to be higher diffusivity (semi-solid: $D_b = 3 \times 10^{-19}$ cm^2 s^{-1}) and liquid ($D_b = 1 \times 10^{-10}$ cm^2 s^{-1}) led to increased condensational growth in the pre-existing Aitken mode and decreased growth of the nucleation mode ($D_p \approx$ 1-10 nm), which is inconsistent with observations. The increased condensation on larger particle sizes led to a reduction in the NPF

rate. Conversely, treating particles as our most-solid assumption led to slower growth in the Aitken mode and more NPF relative to the liquid and semi-solid particle assumptions, consistent with the findings from other work (He et al., 2021; Zaveri et al., 2014, 2018; Reid et al., 2018; Manabu et al., 2017).

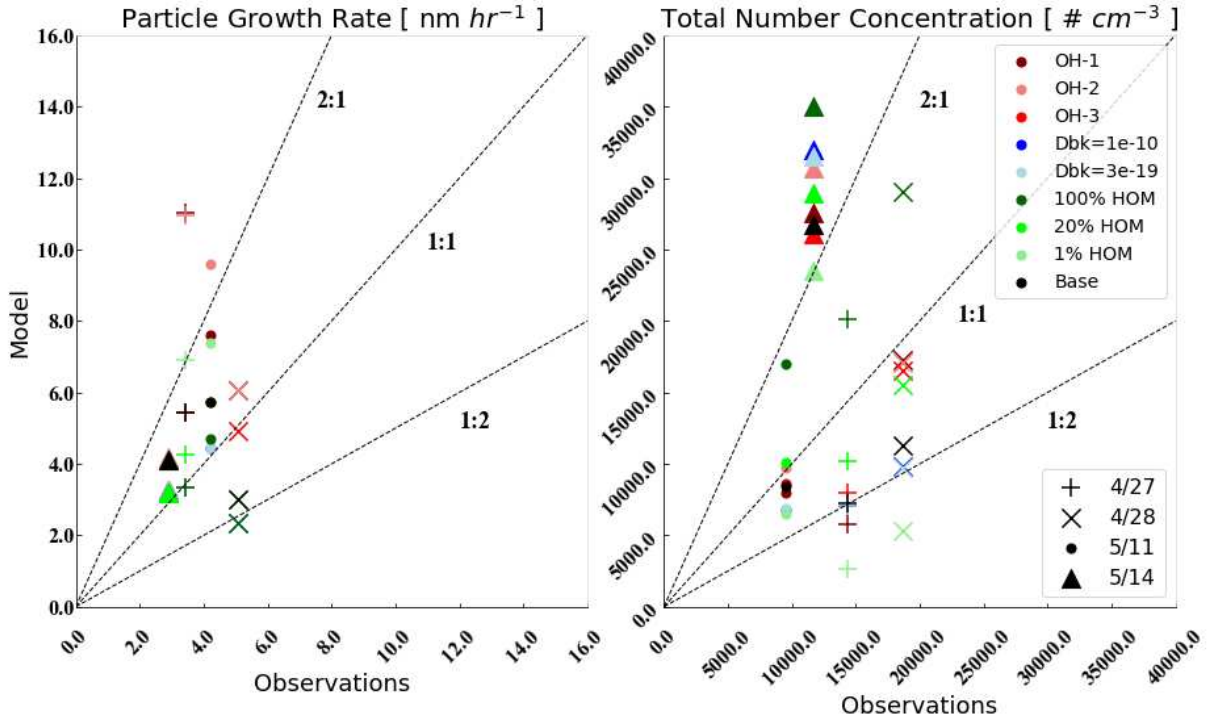

Figure 5. (a) Comparison of the simulated particle growth rates and the observed particle growth rates at the SGP observatory for the four NPF event days. The different colors indicate different simulation assumptions, and the marker shape indicates the NPF event day. **(b)** Comparison of the simulated and observed aerosol number concentrations after the majority of particle growth has occurred (compared at the time of the last black 'x' for each day in Figure 4). Colors and marker shape are the same as panel (a).

3.2.3 - NPF INITIATING ALOFT IN THE MODEL

Results from the base simulation show that SOM-TOMAS favors NPF occurring in the upper half of the developing mixed layer for all simulated NPF events (Figure 6). Similarly, the NPF simulated on 16 May, a non-event day, is largely occurring in the upper half of the shallow mixed layer and in the residual layer. The higher NPF rates on 27 April are primarily just below

the height of the mixed layer throughout the simulation, likely due to the lower temperatures in the upper parts of the mixed layer making nucleation more favorable and leading to lower saturation vapor pressures for NPF precursors; this pattern fits with previous work that found enhanced NPF at the interface between the mixed layer and residual layer (Wehner et al., 2010). The pattern is less clear for the other three NPF events, in part because the top of the mixed layer does not get as high on these days, leading to less lofting of NPF precursors to lower temperatures aloft and less entrainment of air from the residual layer. The patterns of the 1.5-25 nm particle number concentrations in the mixed layer are also less clear due to the rapid mixing that homogenizes these values; however, there is evidence of NPF and particle growth occurring at distinct levels within the residual layer that either remain there or get entrained into the mixed layer as it develops. Similarly, there are levels within the residual layer with lower number concentrations of 1.5-25 nm particles which serve to dilute the 1.5-25 nm particle number concentrations in the mixed layer.

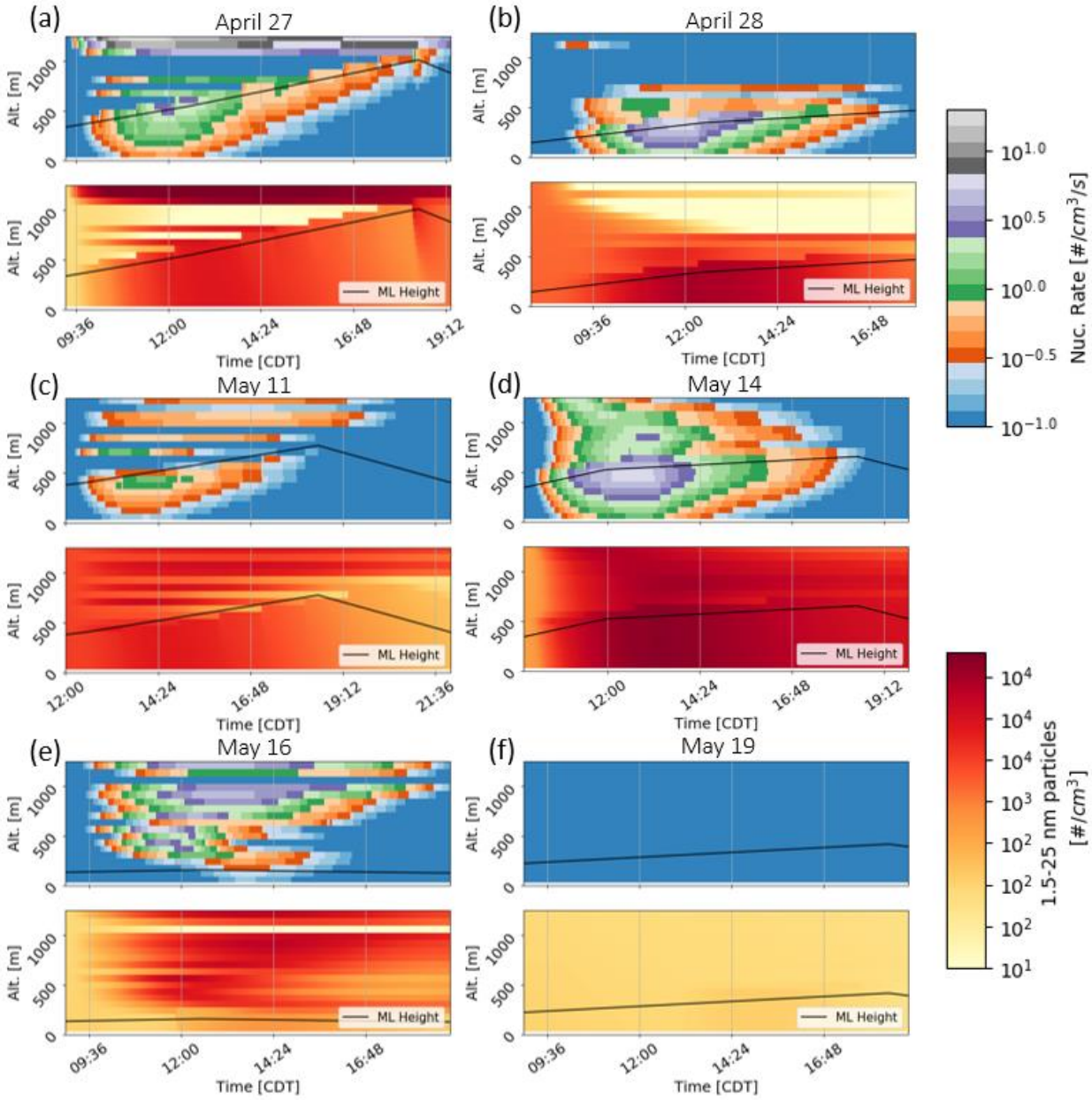

Figure 6. For each sub-panel (a-f), the top panel shows the simulated total nucleation rate (# cm^{-3} s^{-1}) from the surface layer to 2500 m (y-axis) for each simulation period. Additionally, the bottom panels show the simulated total number concentration of particles within the diameter range of 1.5-25 nm (note: colorbar scales for top and bottom panels are different). The height of the mixed layer is shown by the black line.

3.2.4 - ANALYSIS OF POTENTIAL DRIVERS OF NPF ALOFT AND THEIR INFLUENCE ON SURFACE NUMBER CONCENTRATIONS AND PARTICLE GROWTH RATES

In this section, we discuss the results from the six vertical sensitivity simulations (Table 2: *Vertical Sensitivity Analysis*) and how the results influence nucleation rates and number concentration at the surface relative to the base simulation. Figure 7a shows bar plots of the total particle number concentrations at the surface for the base simulations (black bars, 'Base') and the sensitivity simulations (colored bars) compared at the time of the last black 'x' in Figure 4 for each NPF event day. Similarly, Figure 7b shows bar plots of the simulated particle growth rates [nm h^{-1}] between 2 and 80 nm at the surface for the four NPF event days.

The gray bars labeled 'Nuc. Temp.' in Figure 7a illustrate the effect of implementing a constant vertical temperature profile (set to the surface temperature) for the nucleation routine, leading to significantly decreased particle number concentrations at the surface due to the decreased NPF in the upper parts of the model domain, including the top of the mixed layer and regions of the residual layer that mix into the growing mixed layer. Contrarily, Figure 7b shows that changing the temperature profile in the nucleation routines results in either unchanged (27 April, 28 April, and 14 May) or enhanced (11 May) particle growth rates due to the decrease in the number of aerosol particles sharing condensable material. These sensitivity simulations show that the temperature dependence of the nucleation routines is a significant driver of enhanced NPF in the upper parts of the mixed layer in the model; consequently, this temperature dependence leads to enhancements of the total aerosol particle number concentrations at the surface.

Sensitivity simulations using a constant vertical temperature profile (set to the surface temperature) only in the organic-species volatility calculations leads to enhancements in the aerosol particle number concentrations on three of the four NPF event days and a decrease in the particle growth rate for all four days (Figure 7; green bars, 'C* Temp.'). The artificially higher

temperatures in the upper parts of the model domain lead to organic species with higher volatility in these locations (relative to the base simulation) that are less likely to partition to new and existing aerosol particles, leading to slower particle growth rates. The slower growth rates mean freshly nucleated particles cannot grow as quickly to sizes where coagulational loss rates are slower, leading to a reduction in the total number concentration. Conversely, the reduced particle growth rates lead to fewer larger particles, in turn, reducing the coagulational sink for smaller particles and leading to enhanced particle number concentrations relative to the base simulation. The increases in particle number concentration on 27 April, 28 April, and 14 May relative to the base simulation indicate that the reduction in the coagulation sink was more significant than the reduction in the growth rates of freshly nucleated particles. Conversely, 11 May showed a decrease in the particle number concentration, indicating that the slower growth rate of the small particles was more powerful than the decrease in the coagulation sink. Additionally, a reduced condensation sink led to slightly enhanced and prolonged NPF rates for all days; however, the net effect on the surface aerosol size distribution was dependent on the competing processes discussed above (note that the HOMs are assumed to be nonvolatile in all simulations).

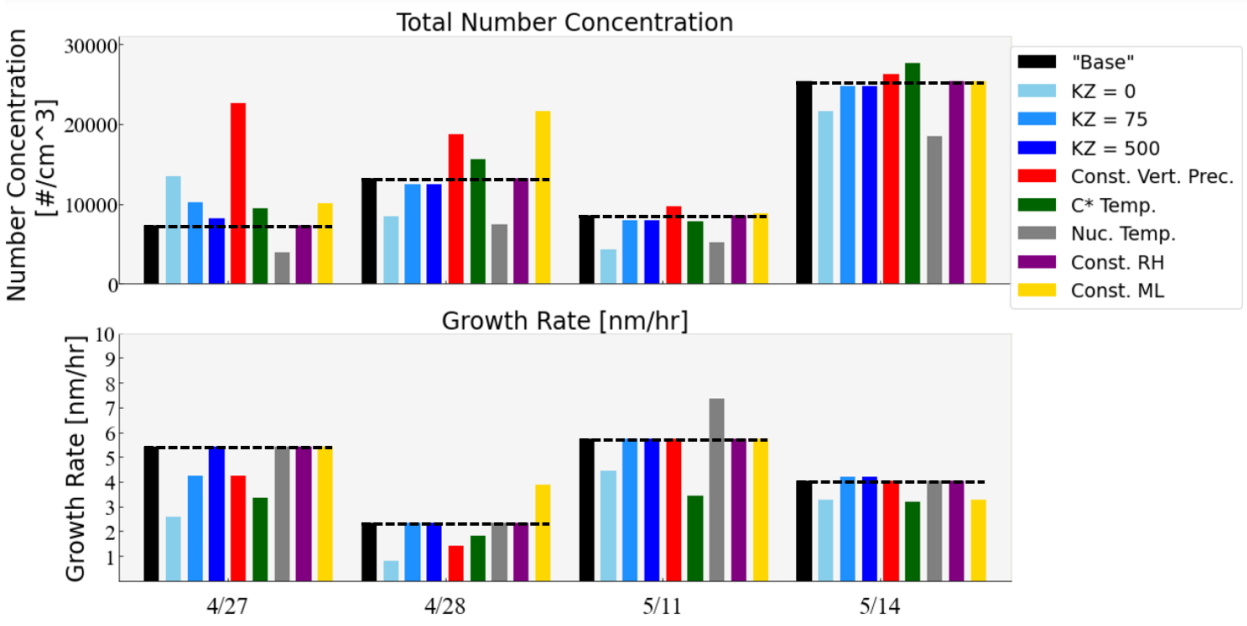

Figure 7. (a) Total number concentration of particles at the surface for the base simulation and the vertical sensitivity simulations for each NPF event. (b) Particle growth rate of nucleated particles at the surface for the base simulation and the sensitivity simulations for each day. (a-b) Base simulation is shown by the black bar, and the red-dashed line indicates the height of the black bar for comparison with the sensitivity simulations. 'KZ = 0' or light-blue bars correspond to the simulations with no vertical mixing. 'KZ = 75' or middle-blue bars correspond to the simulations with a vertical mixing coefficient of K_Z = 75 m^2 s^{-1}. 'KZ = 500' or dark-blue bars correspond to the simulations with a vertical mixing coefficient of K_Z = 500 m^2 s^{-1}. 'Const. Vert. Prec.' (constant vertical precursors) or red bars correspond to the simulations with constant mixing ratios of the gas-phase NPF precursors outlined in Table 1. 'C* Temp.' or green bars correspond to simulations using a constant vertical temperature profile for only the organic species volatility calculation. 'Nuc. Temp.' or gray bars correspond to simulations using a constant vertical temperature profile only for the nucleation routines. 'Const. RH' corresponds to the simulations using 50% RH for all vertical layers and for the duration of the simulations. 'Const. ML' corresponds to the simulations using a constant mixed layer height during the simulation period.

To test the influence of the vertical mixing rate on NPF and particle growth at the surface, we ran simulations with no vertical mixing (K_Z = 0.0 m^2 s^{-1}) and with slower vertical mixing rates (K_Z = 500 m^2 s^{-1} and K_Z = 75 m^2 s^{-1}) than the base simulation (K_Z = 2000 m^2 s^{-1}). The slower vertical mixing rate of K_Z = 500 m^2 s^{-1} resulted in similar particle number concentrations and growth rates as the base simulation (Figure 7: dark blue bars, 'KZ = 500'). Similarly, the slower vertical mixing rate of K_Z = 75 m^2 s^{-1} (Figure 7; middle blue) resulted in similar growth rates and number concentrations as the K_Z = 500 m^2 s^{-1} simulations for three of the four simulation days. On 27 April, the slower vertical mixing (K_Z = 75 m^2 s^{-1}) resulted in growth rates and number concentrations in between those from the K_Z = 500 m^2 s^{-1} and K_Z = 0.0 m^2 s^{-1} simulations, indicating that the results at the surface are more sensitive to vertical mixing on that day, Overall, we find that our results are not greatly sensitive to a range of reasonable vertical diffusivities. Simulations with no vertical mixing resulted in lower surface total particle number concentrations on 28 April, 11 May, and 14 May, and lower surface particle growth rates on all four days (Figure

7; light blue, 'KZ = 0'). The lower particle number concentrations observed at the surface are attributable to the enhanced NPF taking place in the upper mixed layer and residual layer not mixing downwards to the surface. Contrarily, the number concentration at the surface in the 27 April non-mixing simulation is higher than the number concentration at the surface in the base simulation, indicating that vertical mixing serves to spread the freshly nucleated particles and NPF precursors from the surface level to the levels higher up in the mixed layer. The initial vertical profile of SO_2 on 27 April is relatively constant within the mixed layer, and vertical profiles of isoprene, benzene, and toluene show a significant increase above the surface in the mixed layer (Figure S5a); however, the initial profiles of trimethylbenzene, xylenes and monoterpenes, which have relatively large HOM yields, steadily decline throughout the mixed layer. The lack of vertical mixing means the surface layer has the highest concentration of organic species with high HOM yields, leading to substantial organic-sulfuric acid nucleation at the surface on 27 April. As previously mentioned, the surface layer particle growth rates for all simulated days were lower with vertical mixing switched off. The suppression of particle growth is partially due to the lack of mixing from upper model layers where condensational growth is favored due to the lower intrinsic volatility of gas-phase species at lower temperatures. The lower growth rates are also potentially attributable to enhancements of organic and inorganic species in the upper levels of the model (Figure S5) that are not allowed to mix downwards and contribute to particle growth. From our analysis of four NPF events, we find that vertical mixing primarily serves to enhance the total aerosol particle number concentrations and particle growth rates at the surface because of the generally faster NPF rates at the top of the mixed layer.

To investigate the influence of the vertical profiles of gas-phase species, derived from HI-SCALE data (Figure S5a-b), on NPF and particle growth, we initialized all model layers with the

mixing ratio of gas-phase species at the surface outlined in Table 1. These simulations resulted in higher particle number concentrations at the surface for all four NPF events (Figure 7: red bars, 'Const. Vert. Prec.'), and slower particle growth rates for 27 April and 28 April (11 May and 14 May were negligibly different from the base simulation). The largest change, relative to the base simulation, in particle number concentration and particle growth rate is on 27 April and 28 April, indicating that the initial vertical profiles of the gas-phase species have the net effect of reducing the surface number concentrations relative to simulations with our best estimates of initial gas-phase vertical profiles. The changes in surface particle number concentration on 11 May and 14 May were less pronounced, indicating that the initial vertical profiles of precursors used in the base simulation have a reduced effect on the NPF and growth observed at the surface. Similar to other scenarios previously discussed, the reductions in particle growth rates on 27 April and 28 April are largely attributable to the higher particle number concentrations participating in condensational growth. With the smaller relative change in the surface layer particle number concentration on 11 May and 14 May relative to the base simulation, the negligible change in particle growth rate is expected. It should be noted that many of the vertical enhancements in gas-phase precursors (Figure S5a-d) are at levels that the mixed layer does not reach (Figure S2); therefore, the effects that these enhancements have on NPF rates and particle growth are only realized in the upper parts of the model domain and not at the surface.

In order to test the influence of the vertical profile of RH (i.e., water vapor equilibrium partitioning with the aerosol) on the surface aerosol population, we used a constant relative RH of 50% for all model layers for the entire simulation period (Figure 7: purple bars). Using a constant RH value will test the influence of the vertical profile on particle water uptake, and thus the RH influence on the condensation sink and on the vertical profile of NPF. We found that using a

constant RH value led to virtually no change in the particle number concentration and growth rate at the surface. In the base simulation, we expect the vertical profile of RH to change the size-resolved dry composition due to changes in water vapor condensation vertically. A caveat to these results is that we do not explicitly consider any effects of water uptake on chemistry in the aerosol-phase, which has been found to increase simulated particle growth (Hodshire et al., 2016; Chen et al., 2018; Hamed et al., 2011), nor do we include an effect of water vapor on nucleation rates, following the Dunne et al. (2016) and Riccobono et al. (2014) schemes.

In order to investigate the influence of the height of the developing mixed layer on the surface aerosol size distribution, we set the mixed layer height in each simulation to the average height of the mixed layer, measured from radiosondes, during the simulation periods. Using a constant mixed layer height partially eliminates the time-dependent influence of entrainment of gases and particles from the residual layer on the surface aerosol size distribution. However, the timing and intensity of NPF and growth in the mixed layer is altered due to the mixed layer height being higher than the base simulation at the beginning of the simulation period and lower than the base simulation near the end of the test simulation. With the exception of 28 April, there is little change in the surface aerosol size distribution from using a constant mixed layer height (Figure 7: yellow bars, 'Const. ML'). This limited change in the surface size distribution indicates that our results are not heavily reliant on NPF and growth in the residual layer entraining into the mixed layer. On 28 April, using a constant mixed layer height led to enhanced apparent NPF at the surface, and an enhanced apparent particle growth rate.

3.3. DISCUSSION ON THE NECESSARY CONSTRAINTS TO BETTER UNDERSTAND THE VERTICAL PROFILE OF NUCLEATION AND GROWTH

While our base simulations in this work did an adequate job of reproducing the observed nucleation and growth at the surface, a number of key details of the vertical profile of nucleation and growth were not fully constrained in our work. The limitations in our constraints stem partially from the measurements taken during the HI-SCALE campaign and partially from uncertainties and an incomplete representation of all relevant processes in our modeling approach. These details regarding our analysis of HI-SCALE measurements include (but are not limited to) the following aspects of the measurements: (1) the precise vertical profile of precursors that were not directly measured both at the surface and by the aircraft, (2) the flight timing and path, and (3) the role of airmass changes on the observed aerosol size and composition evolution. Details relating to constraints that could come from either measurements or models include: (4) the poorly constrained OH concentrations, and (5) uncertainties in vertical mixing rates on nucleation and growth. Modeling limitations include: (6) the precise relative mixture of fully inorganic nucleation versus nucleation involving organic molecules, (7) the role of aerosol water on chemistry and gas-particle partitioning, (8) the lack of RH dependence in the nucleation routines, (9) the lack of representation of the role of amines and other species in NPF, and (10) the intrinsic limitations of 1-D modeling approach. Below, we expand on these limitations to help guide future campaigns and modeling focused on the understanding of NPF and growth vertically in the lower troposphere. The following recommendations are not organized by priority, and the implementation of, sometimes mutually exclusive, recommendations depends on research goals and the constraints of different field campaign operations.

Measurement limitations:

(1) Regarding differences in species, when run in standard mode, the HRToF-CIMS aboard the aircraft measured a variety of gas-phase species (notably the oxidation products of isoprene and monoterpenes), but these species were different from those measured at the surface by the PT-RMS (generally non-oxidized, primary VOCs). This discrepancy in the measured gas-phase species led us to test several assumptions about the vertical profiles of the gas-phase species (Table 1) needed for our modeling (including assuming the species concentrations at the lowest aircraft altitude are the same as at the surface and that the relative profile of oxidation products match that of the parent VOC), and these assumptions contribute to our ability to understand the vertical profile of NPF. The uncertainty in the absolute gas concentrations is particularly important in the initial residual layer, where NPF may occur with these particles later being entrained into the mixed layer. Given the variability in timing and spatial extent of NPF events and the broad scope of the HI-SCALE campaign, we find harmonization and congruency between surface and airborne observations to be of great importance, especially for gas-phase species that contribute to NPF. While logistics, funding, and other constraints may make it difficult for future field campaigns, we recommend having instruments at the surface and in the air (e.g., tethered balloon) that measure identical or similar quantities with the same degree of accuracy. To better constrain the oxidation chemistry driving the gas- and aerosol-processes in the mixed layer and residual layer, we recommend measurements of OH at the surface and in the air (Heard and Pilling, 2003). Additionally, measurements of amines and NH_3 are highly useful for understanding NPF under ambient conditions (note: NH_3 was measured intermittently on flights and amines were measured during IOP2).

(2) As mentioned, a notable characteristic of the HI-SCALE campaign that limits our analysis is flight timing and flight path being primarily horizontal and often not capturing the pre-nucleation atmosphere (and also generally do not go below ~500 m, contributing to the previous issue of vertical profiles). The flight path constraint does not directly affect our modeling, but it does limit the robustness of our conclusions due to the low number of available analysis flights. Additionally, flights often occurred after NPF had been detected at the surface site (it is challenging to know when NPF will start and to plan profiles accordingly), thus limiting the ability to understand the characteristics of the atmosphere prior to NPF occurring and/or being observed at the surface. These are all inherent challenges of airborne sampling with a fixed-wing crewed aircraft, and particularly in a field campaign with multiple objectives beyond understanding NPF and growth. It is near impossible to counter these limitations given the constraints of a larger aircraft and the variability in NPF event occurrences. For studies investigating the vertical profile of NPF, we recommend using smaller aerial vehicles that can sample more frequently to counter the inability to predict the onset of NPF in real-time (in addition to large, crewed aircraft if funding allows). Several studies have utilized unmanned aerial vehicles and tethered balloons to capture more frequent vertical profiles of aerosol particle data from the ground to ~1 km (Chen et al., 2018; Platis et al., 2016; Qi et al., 2019; Carnerero et al., 2018; Creamean et al., 2018); however, these studies are limited by payload constraints that prevent more comprehensive measurements, such as gas-phase species, to be taken. It should be noted that aircraft observations can be complemented by measurements from particle flux towers, such as one installed at the SGP observatory since HI-SCALE.

(3) It appears likely that some observed fluctuations in the ground-based size distributions during our examined days may be due to advection of air with different aerosol/gas properties, including plumes. Again, this is an inherent challenge of field analysis that relies heavily on a single field site, but contributes to our limitations. Some smaller platforms (e.g. blimps) can take pseudo-Lagrangian measurements, thus limiting the influence of other factors such as air mass changes on the measurements. Additionally, a large aircraft could perform pseudo-Lagrangian transects of the atmosphere based on the mean wind speed at a given altitude; however, this approach would deliver little vertical information about the atmosphere. Overall, to counter issues related to NPF initiation and flight timing, we recommend utilizing smaller aerial platforms in order to characterize the pre-NPF atmosphere, either by more-frequent vertical sampling or through Lagrangian drifting (note: pseudo-Lagrangian sampling works to sample the pre-NPF atmosphere, but comparison with other measurements is hard because it assumes the Lagrangian sample is representative of the surrounding airmass).

Modeling and measurement limitations:

(4) Our modeling analysis is hindered by a variety of factors beyond the measurement limitations described above, the first of which is our use of poorly constrained OH concentrations. The NPF rate and OA production in SOM-TOMAS is sensitive to OH concentrations; however, the OH concentrations tested in this work can span two orders of magnitude (Figure S7) for the same time period leading to a high degree of uncertainty in our results. As mentioned previously, measurements of OH concentrations would help to constrain this problem. We recommend that if utilizing a model that represents reactions with OH, an appropriate OH measurement or OH proxy that is representative of the region

in question should be used; however, many available proxies do not provide vertical information, therefore, measurements would help to constrain OH concentrations at different vertical levels. Alternatively, we could have used a gas-phase chemical mechanism to estimate OH concentrations but this would have placed an even higher burden on knowing the gas-phase concentrations for a larger number of species (e.g., reactive nitrogen, VOCs) at the surface and aloft.

(5) Another factor influencing our model analysis is the use of simple vertical mixing schemes in the mixed layer and residual layer. While we did not find substantial differences between $K_z = 500\ m^2\ s^{-1}$ and $K_z = 2000\ m^2\ s^{-1}$ in our work, our assumption of a well-mixed and rapidly overturning mixed layer may lead to erroneous results on days where this is not the case (Du et al., 2020; Lai et al., 2022). For future work, we recommend parameterizing vertical mixing based on observations of vertical turbulent kinetic energy, data from particle flux towers, or output from a meso- or micro-scale model that resolves small turbulent eddies.

Modeling limitations:

(6) A significant limiting factor in our model analysis is our estimated fraction of HOMs contributing directly to organic-sulfuric acid NPF. We assumed that 10% of HOMs contribute directly to the organic-sulfuric acid nucleation scheme as this assumption lead to results that agreed best with observations (Figure S3); however, this assumption will likely break down in different environments that are influenced by a different mixture of precursors to HOMs (Ehn et al., 2017; Bianchi et al., 2019) and colocated species (e.g., NO_X) (Roldin et al., 2019). For future modeling efforts, we need an improved

understanding of the organic species that participate in NPF, and we need modeling frameworks that explicitly predict the formation of these species.

(7) Another factor influencing our model analysis is the lack of representation of the role of aerosol water on aerosol partitioning and aqueous-phase chemistry. The version of SOM-TOMAS used in this work does not represent the effects of aerosol water uptake on aerosol-phase partitioning, potentially leading to inaccurate particle growth rates. Similarly, the lack of aqueous-phase chemistry is likely to influence the model-to-measurement comparison at the SGP site. For better representation of aerosol particle partitioning in the atmosphere and its effect on NPF and growth in the mixed layer and residual layer, we recommend future work in modeling this process in the atmosphere based on laboratory experiments (e.g. DeRieux et al., 2019; Tong et al., 2021; Yu et al., 2017b). We also recommend not discounting the role of aqueous-phase chemistry in influencing NPF (via precursor concentrations and condensation sinks) at the SGP observatory.

(8) Our model results are impacted by the assumption in the native NPF schemes from Riccobono et al. (2014) and Dunne et al. (2016) that there is no RH dependence (a simple RH correction is suggested by Dunne et al. (2016), but it is not a function of the NH_3 concentration). The aircraft measured ammonia concentrations is >5.0 ppbv in the mixed layer for the four NPF events analyzed; therefore, the influence of RH on NPF is likely to be small (Merikanto et al., 2007) in the mixed layer and residual layer, but it remains uncertain. We recommend the inclusion of updated parameterizations for the dependence

of NPF rates on ambient RH in models, as this could influence NPF rates vertically due to the steep RH gradients between the mixed layer, residual layer, and free troposphere (e.g. Yu et al., 2017b; Merikanto et al., 2007).

(9) Our model results are impacted by not representing the role of amines and other compounds in NPF, which may hinder our representation of observed NPF at the SGP observatory, where amine concentrations may be non-trivial due to nearby agriculture. We recommend the inclusion of NPF and growth mechanisms involving amines, nitric acid (although the median aerosol nitrate concentration was 0.122 [μg m^{-3}] during IOP1, so unlikely to be a factor in our analysis; Liu et al., 2021), and other compounds involved in tropospheric NPF, in order to better represent the full breadth of NPF pathways in the mixed layer and the residual layer.

(10) Finally, our model results are influenced by the 1-D model configuration. We do not explicitly consider emissions (though we implicitly have by holding precursor vapor burdens fixed following the relatively constant observed concentrations) or consider advection in the model; therefore, in attempting to match observations that are likely influenced by emissions and advection, we are potentially over- or under-weighting the influence of vertical factors on results at the surface. Our results indicate that changes in vertical quantities, such as temperature and gas-phase species, have the potential to dramatically change the observed NPF and growth at the surface. However, elucidating the actual influence of non-vertical factors on NPF observed at the surface is difficult given our model framework. Our work serves as a useful test to understand the potential

influences of different vertical quantities, but we recommend future work consider emissions and horizontal advection when trying to understand NPF and growth at the surface.

CHAPTER 4

CONCLUSIONS

This paper presents an analysis of the vertical profile of NPF in the lower troposphere using field campaign data and 1D modeling. Firstly, we analyzed aircraft and ground-based data from four NPF events and two non-NPF events observed during IOP1 of the HI-SCALE campaign at the ARM SGP observatory. Secondly, we utilized a 1D model that represents semi-explicit gas-phase chemistry and thermodynamics along with advanced aerosol microphysical mechanisms to help elucidate the driving mechanisms behind observed NPF during HI-SCALE.

Our analysis of the HI-SCALE aircraft data yielded observations of enhanced number concentrations of particles in the diameter range of 3-10 nm at various, often distinct, levels within the mixed layer and residual layer during the four NPF events analyzed. Relating these aircraft observations to surface observations proved difficult due to a variety of factors including steep vertical and horizontal gradients of ultrafine particles, as well as the flight path and timing. The strongest evidence for NPF occurring aloft is on 11 May where enhancements of 3-10 nm particles were observed upwind of the SGP ground site near the top of the developing mixed layer, albeit after NPF was already observed at the SGP ground site (Figure 3c). Additionally, we often observed enhancements in gas-phase organic species and SO_2 within the mixed layer and residual layer, but attribution of these enhancements proves difficult through our back-trajectory analysis as we cannot distinguish between localized and distant sources. Our analysis of the HI-SCALE campaign aligns with previous analyses (Fast et al., 2019; Liu et al., 2021), and previous work at the SGP observatory (Hodshire et al., 2016; Chen et al., 2018). The aircraft and ground-based

observations of gas-phase NPF precursors and aerosol size distributions from the HI-SCALE campaign were used as inputs for our modeling approach.

The 1D model, SOM-TOMAS, correctly predicts the occurrence of the four NPF events, and predicts very weak NPF and growth on the two days where no NPF was observed. For the NPF event days, SOM-TOMAS captures the observed particle growth rates and number concentrations; however, the model performance is largely dependent on assumptions for OH concentrations, the fraction of HOMs contributing to organic-sulfuric acid nucleation (10% of HOMs formed), and the particle-phase diffusivity (i.e., semi-solid with a Db of 10^{-20} cm^2 s^{-1}). SOM-TOMAS predicts NPF occurring primarily in the upper half of the developing mixed layer for the four NPF events, where air from the residual layer is being entrained into the mixed layer and where temperatures are coldest. These findings are consistent with those from Hellmuth (2006), but our results differ from those of Boy et al. (2006) and Lauros et al. (2011). The NPF rate is dominated by organic-sulfuric acid nucleation on 27 and 28 April, while 11 and 14 May show slightly more inorganic NPF occurring than organic-sulfuric acid NPF.

We ran a variety of vertical sensitivity simulations including different vertical mixing rates, constant vertical mixing ratio of precursors, constant vertical temperature in the vapor pressure calculation for organic species, constant vertical temperature in the nucleation schemes, and a constant vertical profile of 50% RH. We found that the vertical mixing in the base simulations enhanced the surface level particle number concentrations and particle growth rates on three of the four NPF days, values that were most consistent with observations. Assuming a constant vertical mixing ratio of the organic and inorganic NPF precursors (set to surface values) led to enhanced number concentrations at the surface for all days and decreased or unchanged growth rates for all days. This pattern indicates that the vertical profiles of gas-phase species taken from HI-SCALE

served to reduce the number concentrations and increase the particle growth rate at the surface for the simulated NPF events. Using the surface temperature in the organic species volatility calculation for all vertical levels generally led to an increase in particle number concentrations and a decrease in particle growth rates. This general behavior shows that a decrease in the survival probability of small particles due to slower condensational growth was overpowered by a decrease in the coagulation sink for small particles due to fewer larger particles. Using the surface temperature in the nucleation scheme led to decreases in particle number concentration and either no change or increases in the particle growth rate at the surface. This pattern shows that, in the base simulation, the lower temperatures in the upper mixed layer drive increased nucleation at those levels, which corresponds to an increase in the total particle number concentration at the surface. Finally, using an RH value of 50% for all levels led to virtually no change in the total particle number concentration and particle growth rate at the surface.

While our work illustrates a novel approach to understanding the vertical profile of NPF, we are limited by several key model assumptions and a lack of observational constraints that hinder our ability to find closure between our model simulations and the observations from HI-SCALE (details in Section 3.3). The variability in the timing and spatial extent of NPF events make vertical observations difficult; however, we find that harmonized (i.e., equivalent or similar instruments) observations of both gas-phase and aerosol properties at the surface and in the air throughout the duration of NPF events is crucial for our understanding of the vertical profile and dynamics of NPF. Similarly, we encourage observations of OH concentrations to better constrain and connect the chemical and aerosol microphysical properties in the atmosphere. We also encourage better constraints on vertical mixing through the use of particle flux towers and vertical turbulent kinetic

energy data; however, we also find, through observations and 1D modeling, that horizontal transport of and inhomogeneities in air masses cannot be ignored.

This work has built upon previous studies on the vertical extent of NPF using one-dimensional column models (e.g. Boy et al., 2006; Hellmuth, 2006; Lauros et al., 2011) and observations of turbulence- and mixing-induced NPF (e.g. Nilsson et al., 2001; Wehner et al., 2010) by using (1) constraints from airborne and surface-based observations and (2) updated, complex representations of chemical and aerosol processes. Our results generally align with previous work, but our framework allows us to look closer at the impacts of observational constraints, gas-phase chemistry, partitioning thermodynamics, particle phase state, and a variety of other factors on the vertical profile of NPF. Yet, even with these constraints and updates, open questions remain. Understanding these impacts will improve our mechanistic representation of NPF in models, a necessity for understanding past and future NPF and its contribution to CCN and aerosol number concentrations.

BIBLIOGRAPHY

Adams, P. J.; Seinfeld, J. H.: Predicting Global Aerosol Size Distributions in General Circulation Models. *J. Geophys. Res.: Atmos.*, *107* (D19), AAC 4-1-AAC 4-23. doi:10.1029/2001JD001010, 2002

Akherati, A.; He, Y.; Coggon, M. M.; Koss, A. R.; Hodshire, A. L.; Sekimoto, K.; Warneke, C.; de Gouw, J.; Yee, L.; Seinfeld, J. H.; Onasch, T. B.; Herndon, S. C.; Knighton, W. B.; Cappa, C. D.; Kleeman, M. J.; Lim, C. Y.; Kroll, J. H.; Pierce, J. R.; Jathar, S. H.: Oxygenated Aromatic Compounds Are Important Precursors of Secondary Organic Aerosol in Biomass-Burning Emissions. *Environ. Sci. Technol.*, *54* (14), 8568–8579. doi:10.1021/acs.est.0c01345, 2020.

Albrecht, B. A.: Aerosols, cloud microphysics, and fractional cloudiness, *Science*, 245(4923), 313 1227–1230, 1989.

Ball, S. M.; Hanson, D. R.; Eisele, F. L.; McMurry, P. H.: Laboratory Studies of Particle Nucleation: Initial Results for H2SO4, H2O, and NH3 Vapors. *J. Geophys. Res.: Atmos.*, *104* (D19), 23709–23718. doi:10.1029/1999JD900411, 1999.

Bianchi, F.; Tröstl, J.; Junninen, H.; Frege, C.; Henne, S.; Hoyle, C. R.; Molteni, U.; Herrmann, E.; Adamov, A.; Bukowiecki, N.; Chen, X.; Duplissy, J.; Gysel, M.; Hutterli, M.; Kangasluoma, J.; Kontkanen, J.; Kürten, A.; Manninen, H. E.; Münch, S.; Peräkylä, O.; Petäjä, T.; Rondo, L.; Williamson, C.; Weingartner, E.; Curtius, J.; Worsnop, D. R.; Kulmala, M.; Dommen, J.; Baltensperger, U.: New Particle Formation in the Free Troposphere: A Question of Chemistry and Timing. *Science*, *352* (6289), 1109–1112. doi:10.1126/science.aad5456, 2016.

Bianchi, F.; Kurtén, T.; Riva, M.; Mohr, C.; Rissanen, M. P.; Roldin, P.; Berndt, T.; Crounse, J. D.; Wennberg, P. O.; Mentel, T. F.; Wildt, J.; Junninen, H.; Jokinen, T.; Kulmala, M.; Worsnop, D. R.; Thornton, J. A.; Donahue, N.; Kjaergaard, H. G.; Ehn, M.: Highly Oxygenated Organic Molecules (HOM) from Gas-Phase Autoxidation Involving Peroxy Radicals: A Key Contributor to Atmospheric Aerosol. *Chem. Rev.*, *119* (6), 3472–3509. doi:10.1021/acs.chemrev.8b00395, 2019.

Bilsback, K. R.; He, Y.; Cappa, C. D.; Chang, R. Y.; Croft, B.; Martin, R. V.; Ng, N. L.; Seinfeld, J. H.; Pierce, J. R.; Jathar, S. H.: Vapors are Lost to Walls, Not to Particles on the Wall: Development of Artifact-Corrected Parameters from Chamber Experiments and Implications for Global Secondary Organic Aerosol. *In Prep.*

Birmili, W.; Wiedensohler, A.: New Particle Formation in the Continental Boundary Layer: Meteorological and Gas Phase Parameter Influence. *Geophys. Res. Lett.*, *27* (20), 3325–3328. doi:10.1029/1999GL011221, 2000.

Boucher, O., Randall, D., Artaxo, P., Bretherton, C., Feingold, G., Forster, P., Kerminen, V.M., Kondo, Y., Liao, H., Lohmann, U., Rasch, P., Satheesh, S. K., Sherwood, S., Stevens, B., and Zhang, X. Y.: Clouds and Aerosols, in: Climate Change 2013: The Physical Science Basis. Contribution of Working Group I to the Fifth Assessment Report of the Intergovernmental Panel on Climate Change, edited by: Stocker, T. F., Qin, D., Plattner, G.K., Tignor, 55 M., Allen,S. K., Boschung, J., Nauels, A., Xia, Y., Bex, V., and Midgley, P. M., *Cambridge University Press*, Cambridge, UK, and New York, NY, USA, 2013.

Boulon, J.; Sellegri, K.; Hervo, M.; Picard, D.; Pichon, J.-M.; Fréville, P.; Laj, P.: Investigation of Nucleation Events Vertical Extent: A Long Term Study at Two Different Altitude Sites. *Atmos. Chem. Phys.*, *11* (12), 5625–5639. doi:10.5194/acp-11-5625-2011, 2011.

Boy, M.; Hellmuth, O.; Korhonen, H.; Nilsson, E. D.; ReVelle, D.; Turnipseed, A.; Arnold, F.; Kulmala, M.: MALTE – Model to Predict New Aerosol Formation in the Lower Troposphere. *Atmos. Chem. Phys.*, *6* (12), 4499–4517. doi:10.5194/acp-6-4499-2006, 2006.

Cappa, C. D.; Wilson, K. R.: Multi-Generation Gas-Phase Oxidation, Equilibrium Partitioning, and the Formation and Evolution of Secondary Organic Aerosol. *Atmos. Chem. Phys.*, *12* (20), 9505–9528. doi:10.5194/acp-12-9505-2012, 2012.

Carnerero, C.; Pérez, N.; Reche, C.; Ealo, M.; Titos, G.; Lee, H.-K.; Eun, H.-R.; Park, Y.-H.; Dada, L.; Paasonen, P.; Kerminen, V.-M.; Mantilla, E.; Escudero, M.; Gómez-Moreno, F. J.; Alonso-Blanco, E.; Coz, E.; Saiz-Lopez, A.; Temime-Roussel, B.; Marchand, N.; Beddows, D. C. S.; Harrison, R. M.; Petäjä, T.; Kulmala, M.; Ahn, K.-H.; Alastuey, A.; Querol, X.: Vertical and Horizontal Distribution of Regional New Particle Formation Events in Madrid. *Atmos. Chem. Phys.*, *18* (22), 16601–16618. doi:/10.5194/acp-18-16601-2018, 2018.

Carter, W. P. L.: Development of the SAPRC-07 chemical mechanism - ScienceDirect, available at: https://www.sciencedirect.com/science/article/pii/S1352231010000646.

Charlson, R. J.; Schwartz, S. E.; Hales, J. M.; Cess, R. D.; Coakley, J. A.; Hansen, J. E., and Hofmann, D. J.: Climate forcing by anthropogenic aerosols, *Science*, 255, 423430, 1992.

Chen, H.; Hodshire, A. L.; Ortega, J.; Greenberg, J.; McMurry, P. H.; Carlton, A. G.; Pierce, J. R.; Hanson, D. R.; Smith, J. N.: Vertically Resolved Concentration and Liquid Water Content of

Atmospheric Nanoparticles at the US DOE Southern Great Plains Site. *Atmos. Chem. Phys.*, *18* (1), 311–326. doi:/10.5194/acp-18-311-2018, 2018.

Clement, A. C.; Burgman, R.; Norris, J. R.: Observational and Model Evidence for Positive Low-Level Cloud Feedback. *Science*, *325* (5939), 460–464. doi:10.1126/science.1171255, 2009

Creamean, J. M.; Primm, K. M.; Tolbert, M. A.; Hall, E. G.; Wendell, J.; Jordan, A.; Sheridan, P. J.; Smith, J.; Schnell, R. C.: HOVERCAT: A Novel Aerial System for Evaluation of Aerosol–Cloud Interactions. *Atmos. Meas. Tech.*, *11* (7), 3969–3985. doi:/10.5194/amt-11-3969-2018, 2018.

DeRieux, W.-S. W.; Lakey, P. S. J.; Chu, Y.; Chan, C. K.; Glicker, H. S.; Smith, J. N.; Zuend, A.; Shiraiwa, M.: Effects of Phase State and Phase Separation on Dimethylamine Uptake of Ammonium Sulfate and Ammonium Sulfate–Sucrose Mixed Particles. *ACS Earth Space Chem.*, *3* (7), 1268–1278. doi:10.1021/acsearthspacechem.9b00142, 2019.

Draxler, R. R. and Rolph, G. D.: HYSPLIT (HYbrid Single-Particle Lagrangian Integrated Trajectory) Model access via NOAA ARL READYWebsite, NOAA Air Resources Laboratory, Silver Spring, MD, 2012.

Du, Q.; Zhao, C.; Zhang, M.; Dong, X.; Chen, Y.; Liu, Z.; Hu, Z.; Zhang, Q.; Li, Y.; Yuan, R.; Miao, S.: Modeling Diurnal Variation of Surface $PM_{2.5}$ Concentrations over East China with WRF-Chem: Impacts from Boundary-Layer Mixing and Anthropogenic Emission. *Atmos. Chem. Phys.*, *20* (5), 2839–2863. doi:/10.5194/acp-20-2839-2020, 2020.

Dunne, E. M.; Gordon, H.; Kürten, A.; Almeida, J.; Duplissy, J.; Williamson, C.; Ortega, I. K.; Pringle, K. J.; Adamov, A.; Baltensperger, U.; Barmet, P.; Benduhn, F.; Bianchi, F.;

Breitenlechner, M.; Clarke, A.; Curtius, J.; Dommen, J.; Donahue, N. M.; Ehrhart, S.; Flagan, R. C.; Franchin, A.; Guida, R.; Hakala, J.; Hansel, A.; Heinritzi, M.; Jokinen, T.; Kangasluoma, J.; Kirkby, J.; Kulmala, M.; Kupc, A.; Lawler, M. J.; Lehtipalo, K.; Makhmutov, V.; Mann, G.; Mathot, S.; Merikanto, J.; Miettinen, P.; Nenes, A.; Onnela, A.; Rap, A.; Reddington, C. L. S.; Riccobono, F.; Richards, N. A. D.; Rissanen, M. P.; Rondo, L.; Sarnela, N.; Schobesberger, S.; Sengupta, K.; Simon, M.; Sipilä, M.; Smith, J. N.; Stozkhov, Y.; Tomé, A.; Tröstl, J.; Wagner, P. E.; Wimmer, D.; Winkler, P. M.; Worsnop, D. R.; Carslaw, K. S.: Global Atmospheric Particle Formation from CERN CLOUD Measurements. *Science*, *354* (6316), 1119–1124. doi:/10.1126/science.aaf2649=, 2016.

Ehn, M.; Berndt, T.; Wildt, J.; Mentel, T.: Highly Oxygenated Molecules from Atmospheric Autoxidation of Hydrocarbons: A Prominent Challenge for Chemical Kinetics Studies. *Int. J. Chem. Kinetics*, *49* (11), 821–831. doi:10.1002/kin.21130, 2017.

Fast, J. D.; Berg, L. K.; Alexander, L.; Bell, D.; D'Ambro, E.; Hubbe, J.; Kuang, C.; Liu, J.; Long, C.; Matthews, A.; Mei, F.; Newsom, R.; Pekour, M.; Pinterich, T.; Schmid, B.; Schobesberger, S.; Shilling, J.; Smith, J. N.; Springston, S.; Suski, K.; Thornton, J. A.; Tomlinson, J.; Wang, J.; Xiao, H.; Zelenyuk, A.: Overview of the HI-SCALE Field Campaign: A New Perspective on Shallow Convective Clouds. *Bull. Am. Meteorol. Soc.*, *100* (5), 821–840. doi:/10.1175/BAMS-D-18-0030.1, 2019.

Franchin, A.; Ehrhart, S.; Leppä, J.; Nieminen, T.; Gagné, S.; Schobesberger, S.; Wimmer, D.; Duplissy, J.; Riccobono, F.; Dunne, E. M.; Rondo, L.; Downard, A.; Bianchi, F.; Kupc, A.; Tsagkogeorgas, G.; Lehtipalo, K.; Manninen, H. E.; Almeida, J.; Amorim, A.; Wagner, P. E.; Hansel, A.; Kirkby, J.; Kürten, A.; Donahue, N. M.; Makhmutov, V.; Mathot, S.; Metzger, A.;

Petäjä, T.; Schnitzhofer, R.; Sipilä, M.; Stozhkov, Y.; Tomé, A.; Kerminen, V.-M.; Carslaw, K.; Curtius, J.; Baltensperger, U.; Kulmala, M.: Experimental Investigation of Ion–Ion Recombination under Atmospheric Conditions. *Atmos. Chem. Phys., 15* (13), 7203–7216. doi:10.5194/acp-15-7203-2015, 2015.

Garofalo, L. A.; He, Y.; Jathar, S. H.; Pierce, J. R.; Fredrickson, C. D.; Palm, B. B.; Thornton, J. A.; Mahrt, F.; Crescenzo, G. V.; Bertram, A. K.; Draper, D. C.; Fry, J. L.; Orlando, J.; Zhang, X.; Farmer, D. K.: Heterogeneous Nucleation Drives Particle Size Segregation in Sequential Ozone and Nitrate Radical Oxidation of Catechol. *Environ. Sci. Technol.*, *55* (23), 15637–15645. doi:/10.1021/acs.est.1c02984, 2021.

Gordon, H.; Kirkby, J.; Baltensperger, U.; Bianchi, F.; Breitenlechner, M.; Curtius, J.; Dias, A.; Dommen, J.; Donahue, N. M.; Dunne, E. M.; Duplissy, J.; Ehrhart, S.; Flagan, R. C.; Frege, C.; Fuchs, C.; Hansel, A.; Hoyle, C. R.; Kulmala, M.; Kürten, A.; Lehtipalo, K.; Makhmutov, V.; Molteni, U.; Rissanen, M. P.; Stozkhov, Y.; Tröstl, J.; Tsagkogeorgas, G.; Wagner, R.; Williamson, C.; Wimmer, D.; Winkler, P. M.; Yan, C.; Carslaw, K. S.: Causes and Importance of New Particle Formation in the Present-Day and Preindustrial Atmospheres. *J. Geophys. Res.: Atmos.*, *122* (16), 8739–8760. doi:10.1002/2017JD026844, 2017.

Gryspeerdt, E.; Stier, P.; Partridge, D. G.: Satellite Observations of Cloud Regime Development: The Role of Aerosol Processes. *Atmos. Chem. Phys.*, *14* (3), 1141–1158. doi:10.5194/acp-14-1141-2014, 2014.

Hamed, A.; Korhonen, H.; Sihto, S.-L.; Joutsensaari, J.; Järvinen, H.; Petäjä, T.; Arnold, F.; Nieminen, T.; Kulmala, M.; Smith, J. N.; Lehtinen, K. E. J.; Laaksonen, A.: The Role of Relative

Humidity in Continental New Particle Formation. *J. Geophys. Res.: Atmos.*, *116* (D3). doi:/10.1029/2010JD014186, 2011.

He, Y.; King, B.; Pothier, M.; Lewane, L.; Akherati, A.; Mattila, J.; K. Farmer, D.; L. McCormick, R.; Thornton, M.; R. Pierce, J.; Volckens, J.; H. Jathar, S.: Secondary Organic Aerosol Formation from Evaporated Biofuels: Comparison to Gasoline and Correction for Vapor Wall Losses. *Environ. Sci.: Processes & Impacts*, *22* (7), 1461–1474. doi:/10.1039/D0EM00103A, 2020.

He, Y.; Akherati, A.; Nah, T.; Ng, N. L.; Garofalo, L. A.; Farmer, D. K.; Shiraiwa, M.; Zaveri, R. A.; Cappa, C. D.; Pierce, J. R.; Jathar, S. H.: Particle Size Distribution Dynamics Can Help Constrain the Phase State of Secondary Organic Aerosol. *Environ. Sci. Technol.*, *55* (3), 1466–1476. doi:/10.1021/acs.est.0c05796, 2021.

He, Y.; Lambe, A. T.; Seinfeld, J. H.; Cappa, C. D.; Pierce, J. R.; Jathar, S. H.: Process-Level Modeling Can Simultaneously Explain Secondary Organic Aerosol Evolution in Chambers and Flow Reactors, *Env. Sci. Technol.*, in press, 2021.

Heard, D. E.; Pilling, M. J.: Measurement of OH and HO2 in the Troposphere. *Chem. Rev.*, *103* (12), 5163–5198. doi:/10.1021/cr020522s, 2003.

Hellmuth, O.: Columnar Modelling of Nucleation Burst Evolution in the Convective Boundary Layer – First Results from a Feasibility Study
 Part I: Modelling Approach. *Atmos. Chem. Phys.*, *6* (12), 4175–4214. doi:/10.5194/acp-6-4175-2006, 2006.

Hodshire, A. L.; Lawler, M. J.; Zhao, J.; Ortega, J.; Jen, C.; Yli-Juuti, T.; Brewer, J. F.; Kodros, J. K.; Barsanti, K. C.; Hanson, D. R.; McMurry, P. H.; Smith, J. N.; Pierce, J. R.: Multiple New-

Particle Growth Pathways Observed at the US DOE Southern Great Plains Field Site. *Atmos. Chem. Phys.*, *16* (14), 9321–9348. doi:/10.5194/acp-16-9321-2016, 2016.

Hodzic, A.; Kasibhatla, P. S.; Jo, D. S.; Cappa, C. D.; Jimenez, J. L.; Madronich, S.; Park, R. J.: Rethinking the Global Secondary Organic Aerosol (SOA) Budget: Stronger Production, Faster Removal, Shorter Lifetime. *Atmos. Chem. Phys.*, *16* (12), 7917–7941. doi:/10.5194/acp-16-7917-2016, 2016.

Hodzic, A.; Madronich, S.; Aumont, B.; Lee-Taylor, J.; Karl, T.; Camredon, M.; Mouchel-Vallon, C.: Limited Influence of Dry Deposition of Semivolatile Organic Vapors on Secondary Organic Aerosol Formation in the Urban Plume. *Geophys. Res. Lett.*, *40* (12), 3302–3307. doi:/10.1002/grl.50611, 2013.

Jathar, S. H.; Cappa, C. D.; Wexler, A. S.; Seinfeld, J. H.; Kleeman, M. J.: Multi-Generational Oxidation Model to Simulate Secondary Organic Aerosol in a 3-D Air Quality Model. *Geosci. Model Dev.*, *8* (8), 2553–2567. doi:/10.5194/gmd-8-2553-2015, 2015.

Kerminen, V.-M.; Chen, X.; Vakkari, V.; Petäjä, T.; Kulmala, M.; Bianchi, F.: Atmospheric New Particle Formation and Growth: Review of Field Observations. *Environ. Res. Lett.*, *13* (10), 103003. doi:10.1088/1748-9326/aadf3c, 2018.

Kirkby, J.; Duplissy, J.; Sengupta, K.; Frege, C.; Gordon, H.; Williamson, C.; Heinritzi, M.; Simon, M.; Yan, C.; Almeida, J.; Tröstl, J.; Nieminen, T.; Ortega, I. K.; Wagner, R.; Adamov, A.; Amorim, A.; Bernhammer, A.-K.; Bianchi, F.; Breitenlechner, M.; Brilke, S.; Chen, X.; Craven, J.; Dias, A.; Ehrhart, S.; Flagan, R. C.; Franchin, A.; Fuchs, C.; Guida, R.; Hakala, J.; Hoyle, C. R.; Jokinen, T.; Junninen, H.; Kangasluoma, J.; Kim, J.; Krapf, M.; Kürten, A.;

Laaksonen, A.; Lehtipalo, K.; Makhmutov, V.; Mathot, S.; Molteni, U.; Onnela, A.; Peräkylä, O.; Piel, F.; Petäjä, T.; Praplan, A. P.; Pringle, K.; Rap, A.; Richards, N. A. D.; Riipinen, I.; Rissanen, M. P.; Rondo, L.; Sarnela, N.; Schobesberger, S.; Scott, C. E.; Seinfeld, J. H.; Sipilä, M.; Steiner, G.; Stozhkov, Y.; Stratmann, F.; Tomé, A.; Virtanen, A.; Vogel, A. L.; Wagner, A. C.; Wagner, P. E.; Weingartner, E.; Wimmer, D.; Winkler, P. M.; Ye, P.; Zhang, X.; Hansel, A.; Dommen, J.; Donahue, N. M.; Worsnop, D. R.; Baltensperger, U.; Kulmala, M.; Carslaw, K. S.; Curtius, J.: Ion-Induced Nucleation of Pure Biogenic Particles. *Nature*, *533* (7604), 521–526. doi:/10.1038/nature17953, 2016.

Kulmala, M., Laaksonen, A., and Pirjola, L.: Parameterizations for sulfuric acid/water nucleation rates, *J. Geophys. Res.*, 103, 8301– 8307, 1998.

Kulmala, M., Vehkamäki, H., Petäjä, T., Dal Maso, M., Lauri, A., Kerminen, V.-M., Birmili, W. and McMurry, P. H.: Formation and growth rates of ultrafine atmospheric particles: a review of observations, *J. Aerosol Sci.*, 35(2), 143–176, doi:10.1016/j.jaerosci.2003.10.003, 2004.

Kulmala, M.; Kerminen, V.-M.: On the Formation and Growth of Atmospheric Nanoparticles. *Atmos. Res.*, *90* (2), 132–150. doi:10.1016/j.atmosres.2008.01.005, 2008.

Lai, S.; Hai, S.; Gao, Y.; Wang, Y.; Sheng, L.; Lupascu, A.; Ding, A.; Nie, W.; Qi, X.; Huang, X.; Chi, X.; Zhao, C.; Zhao, B.; Shrivastava, M.; Fast, J. D.; Yao, X.; Gao, H.: The Striking Effect of Vertical Mixing in the Planetary Boundary Layer on New Particle Formation in the Yangtze River Delta. *Science of The Total Environment*, *829*, 154607. doi:/10.1016/j.scitotenv.2022.154607, 2022.

Lampilahti, J.; Leino, K.; Manninen, A.; Poutanen, P.; Franck, A.; Peltola, M.; Hietala, P.; Beck, L.; Dada, L.; Quéléver, L.; Öhrnberg, R.; Zhou, Y.; Ekblom, M.; Vakkari, V.; Zilitinkevich, S.; Kerminen, V.-M.; Petäjä, T.; Kulmala, M.: Aerosol Particle Formation in the Upper Residual Layer[1] . *Atmos. Chem. Phys.*, *21* (10), 7901–7915. doi:/10.5194/acp-21-7901-2021, 2021.

Lampilahti, J.; Manninen, H. E.; Nieminen, T.; Mirme, S.; Ehn, M.; Pullinen, I.; Leino, K.; Schobesberger, S.; Kangasluoma, J.; Kontkanen, J.; Järvinen, E.; Väänänen, R.; Yli-Juuti, T.; Krejci, R.; Lehtipalo, K.; Levula, J.; Mirme, A.; Decesari, S.; Tillmann, R.; Worsnop, D. R.; Rohrer, F.; Kiendler-Scharr, A.; Petäjä, T.; Kerminen, V.-M.; Mentel, T. F.; Kulmala, M.: Zeppelin-Led Study on the Onset of New Particle [2] Formation in the Planetary Boundary Layer. *Atmos. Chem. Phys.*, *21* (16), 12649–12663. doi:/10.5194/acp-21-12649-2021, 2021.

Lauros, J.; Sogachev, A.; Smolander, S.; Vuollekoski, H.; Sihto, S.-L.; Mammarella, I.; Laakso, L.; Rannik, Ü.; Boy, M.: Particle Concentration and Flux Dynamics in the Atmospheric Boundary Layer as the Indicator of Formation Mechanism. *Atmos. Chem. Phys.*, *11* (12), 5591–5601. doi:/10.5194/acp-11-5591-2011, 2011.

Lawler, M. J.; Draper, D. C.; Smith, J. N.: Atmospheric Fungal Nanoparticle Bursts. *Science Advances*, *6* (3), eaax9051. doi:/10.1126/sciadv.aax9051, 2020.

Lee, S.-H.; Gordon, H.; Yu, H.; Lehtipalo, K.; Haley, R.; Li, Y.; Zhang, R.: New Particle Formation in the Atmosphere: From Molecular Clusters to Global Climate. *J. Geophys. Res.: Atmos.*, *124* (13), 7098–7146. doi:/10.1029/2018JD029356, 2019.

Lehtipalo, K.; Yan, C.; Dada, L.; Bianchi, F.; Xiao, M.; Wagner, R.; Stolzenburg, D.; Ahonen, L. R.; Amorim, A.; Baccarini, A.; Bauer, P. S.; Baumgartner, B.; Bergen, A.; Bernhammer, A.-K.;

Breitenlechner, M.; Brilke, S.; Buchholz, A.; Mazon, S. B.; Chen, D.; Chen, X.; Dias, A.; Dommen, J.; Draper, D. C.; Duplissy, J.; Ehn, M.; Finkenzeller, H.; Fischer, L.; Frege, C.; Fuchs, C.; Garmash, O.; Gordon, H.; Hakala, J.; He, X.; Heikkinen, L.; Heinritzi, M.; Helm, J. C.; Hofbauer, V.; Hoyle, C. R.; Jokinen, T.; Kangasluoma, J.; Kerminen, V.-M.; Kim, C.; Kirkby, J.; Kontkanen, J.; Kürten, A.; Lawler, M. J.; Mai, H.; Mathot, S.; Mauldin, R. L.; Molteni, U.; Nichman, L.; Nie, W.; Nieminen, T.; Ojdanic, A.; Onnela, A.; Passananti, M.; Petäjä, T.; Piel, F.; Pospisilova, V.; Quéléver, L. L. J.; Rissanen, M. P.; Rose, C.; Sarnela, N.; Schallhart, S.; Schuchmann, S.; Sengupta, K.; Simon, M.; Sipilä, M.; Tauber, C.; Tomé, A.; Tröstl, J.; Väisänen, O.; Vogel, A. L.; Volkamer, R.; Wagner, A. C.; Wang, M.; Weitz, L.; Wimmer, D.; Ye, P.; Ylisirniö, A.; Zha, Q.; Carslaw, K. S.; Curtius, J.; Donahue, N. M.; Flagan, R. C.; Hansel, A.; Riipinen, I.; Virtanen, A.; Winkler, P. M.; Baltensperger, U.; Kulmala, M.; Worsnop, D. R.: Multicomponent New Particle Formation from Sulfuric Acid, Ammonia, and Biogenic Vapors. *Sci. Adv.*, *4* (12), eaau5363. doi:10.1126/sciadv.aau5363, 2018.

Leino, K.; Lampilahti, J.; Poutanen, P.; Väänänen, R.; Manninen, A.; Buenrostro Mazon, S.; Dada, L.; Franck, A.; Wimmer, D.; Aalto, P. P.; Ahonen, L. R.; Enroth, J.; Kangasluoma, J.; Keronen, P.; Korhonen, F.; Laakso, H.; Matilainen, T.; Siivola, E.; Manninen, H. E.; Lehtipalo, K.; Kerminen, V.-M.; Petäjä, T.; Kulmala, M.: Vertical Profiles of Sub-3 Nm Particles over the Boreal Forest. *Atmos. Chem. Phys.*, *19* (6), 4127–4138. doi:/10.5194/acp-19-4127-2019, 2019.

Liu, J.; Alexander, L.; Fast, J. D.; Lindenmaier, R.; Shilling, J. E.: Aerosol Characteristics at the Southern Great Plains Site during the HI-SCALE Campaign. *Atmos. Chem. Phys.*, *21* (6), 5101–5116. doi:/10.5194/acp-21-5101-2021, 2021.

Liu, S.; Liang, X.-Z.: Observed Diurnal Cycle Climatology of Planetary Boundary Layer Height. *J. Climate*, *23* (21), 5790–5809. doi:/10.1175/2010JCLI3552.1, 2010.

Long, C.: *The ARM Southern Great Plains Central Facility Best Estimate Radiative Flux CD*; DOE/SC-ARM/TR-007, 1020734; p DOE/SC-ARM/TR-007, 1020734. doi:/10.2172/1020734, 2002.

Merikanto, J.; Napari, I.; Vehkamäki, H.; Anttila, T.; Kulmala, M.: New Parameterization of Sulfuric Acid-Ammonia-Water Ternary Nucleation Rates at Tropospheric Conditions. *J. Geophys. Res.: Atmos.*, *112* (D15). doi:/10.1029/2006JD007977, 2007.

Myhre, G.; Samset, B. H.; Schulz, M.; Balkanski, Y.; Bauer, S.; Berntsen, T. K.; Bian, H.; Bellouin, N.; Chin, M.; Diehl, T.; Easter, R. C.; Feichter, J.; Ghan, S. J.; Hauglustaine, D.; Iversen, T.; Kinne, S.; Kirkevåg, A.; Lamarque, J.-F.; Lin, G.; Liu, X.; Lund, M. T.; Luo, G.; Ma, X.; van Noije, T.; Penner, J. E.; Rasch, P. J.; Ruiz, A.; Seland, Ø.; Skeie, R. B.; Stier, P.; Takemura, T.; Tsigaridis, K.; Wang, P.; Wang, Z.; Xu, L.; Yu, H.; Yu, F.; Yoon, J.-H.; Zhang, K.; Zhang, H.; Zhou, C.: Radiative Forcing of the Direct Aerosol Effect from AeroCom Phase II Simulations. *Atmos. Chem. Phys.*, *13* (4), 1853–1877. doi:10.5194/acp-13-1853-2013, 2013.

Ng, N. L.; Herndon, S. C.; Trimborn, A.; Canagaratna, M. R.; Croteau, P. L.; Onasch, T. B.; Sueper, D.; Worsnop, D. R.; Zhang, Q.; Sun, Y. L.; Jayne, J. T.: An Aerosol Chemical Speciation Monitor (ACSM) for Routine Monitoring of the Composition and Mass Concentrations of Ambient Aerosol. *Aerosol Sci. Technol.*, *45* (7), 780–794. doi:/10.1080/02786826.2011.560211, 2011.

Nikandrova, A.; Tabakova, K.; Manninen, A.; Väänänen, R.; Petäjä, T.; Kulmala, M.; Kerminen, V.-M.; O'Connor, E.: Combining Airborne in Situ and Ground-Based Lidar Measurements for Attribution of Aerosol Layers. *Atmos. Chem. Phys.*, *18* (14), 10575–10591. doi:/10.5194/acp-18-10575-2018, 2018.

Nilsson, E. D.; Rannik, Ü.; Kumala, M.; Buzorius, G.; O'dowd, C. D.: Effects of Continental Boundary Layer Evolution, Convection, Turbulence and Entrainment, on Aerosol Formation. *Tellus-B: Chem. Phys. Meteorol.*, *53* (4), 441–461. doi:/10.3402/tellusb.v53i4.16617, 2001.

Park, D.-H.; Cho, C.; Kim, H.; Park, R. J.; Anderson, B.; Lee, T.; Huey, G. L.; Wennberg, P. O.; Weinheimer, A. J.; Yum, S. S.; Long, R.; Kim, S.-W.: Boundary Layer versus Free Tropospheric Submicron Particle Formation: A Case Study from NASA DC-8 Observations in the Asian Continental Outflow during the KORUS-AQ Campaign. *Atmos. Res.*, *264*, 105857. doi:/10.1016/j.atmosres.2021.105857, 2021.

Parworth, C.; Fast, J. D.; Mei, F.; Shippert, T.; Sivaraman, C.; Tilp, A.; Watson, T.; Zhang, Q.: Long-Term Measurements of Submicrometer Aerosol Chemistry at the Southern Great Plains (SGP) Using an Aerosol Chemical Speciation Monitor (ACSM). *Atmos. Enviro., 106*, 43–55. doi:10.1016/j.atmosenv.2015.01.060, 2015.

Pierce, J. R.; Adams, P. J.: Efficiency of Cloud Condensation Nuclei Formation from Ultrafine Particles. *Atmos. Chem. Phys.*, *7* (5), 1367–1379. doi:10.5194/acp-7-1367-2007, 2007.

Pierce, J. R.; Adams, P. J.: Can Cosmic Rays Affect Cloud Condensation Nuclei by Altering New Particle Formation Rates? *Geophys. Res. Lett.*, *36* (9). doi:/10.1029/2009GL037946, 2009.

Pierce, J. R.; Adams, P. J.: Uncertainty in Global CCN Concentrations from Uncertain Aerosol Nucleation and Primary Emission Rates. *Atmos. Chem. Phys.*, *9* (4), 1339–1356. doi:/10.5194/acp-9-1339-2009, 2009.

Pierce, J. R.; Leaitch, W. R.; Liggio, J.; Westervelt, D. M.; Wainwright, C. D.; Abbatt, J. P. D.; Ahlm, L.; Al-Basheer, W.; Cziczo, D. J.; Hayden, K. L.; Lee, A. K. Y.; Li, S.-M.; Russell, L. M.; Sjostedt, S. J.; Strawbridge, K. B.; Travis, M.; Vlasenko, A.; Wentzell, J. J. B.; Wiebe, H. A.; Wong, J. P. S.; Macdonald, A. M.: Nucleation and Condensational Growth to CCN Sizes during a Sustained Pristine Biogenic SOA Event in a Forested Mountain Valley. *Atmos. Chem. Phys.*, *12* (7), 3147–3163. doi:10.5194/acp-12-3147-2012, 2012.

Pietikäinen, J.-P.; Mikkonen, S.; Hamed, A.; Hienola, A. I.; Birmili, W.; Kulmala, M.; Laaksonen, A.: Analysis of Nucleation Events in the European Boundary Layer Using the Regional Aerosol–Climate Model REMO-HAM with a Solar Radiation-Driven OH-Proxy. *Atmos. Chem. Phys.*, *14* (21), 11711–11729. doi:/10.5194/acp-14-11711-2014, 2014.

Platis, A.; Altstädter, B.; Wehner, B.; Wildmann, N.; Lampert, A.; Hermann, M.; Birmili, W.; Bange, J.: An Observational Case Study on the Influence of Atmospheric Boundary-Layer Dynamics on New Particle Formation. *Boundary-Layer Meteorol*, *158* (1), 67–92. doi:/10.1007/s10546-015-0084-y, 2016.

Qi, X.; Ding, A.; Nie, W.; Chi, X.; Huang, X.; Xu, Z.; Wang, T.; Wang, Z.; Wang, J.; Sun, P.; Zhang, Q.; Huo, J.; Wang, D.; Bian, Q.; Zhou, L.; Zhang, Q.; Ning, Z.; Fei, D.; Xiu, G.; Fu, Q.: Direct Measurement of New Particle Formation Based on Tethered Airship around the Top of the Planetary Boundary Layer in Eastern China. *Atmos. Enviro.*, *209*, 92–101. doi:/10.1016/j.atmosenv.2019.04.024, 2019.

Qi, X.; Ding, A.; Nie, W.; Chi, X.; Huang, X.; Xu, Z.; Wang, T.; Wang, Z.; Wang, J.; Sun, P.; Zhang, Q.; Huo, J.; Wang, D.; Bian, Q.; Zhou, L.; Zhang, Q.; Ning, Z.; Fei, D.; Xiu, G.; Fu, Q.: Direct Measurement of New Particle Formation Based on Tethered Airship around the Top of the Planetary Boundary Layer in Eastern China. *Atmospheric Environment*, *209*, 92–101. doi:/10.1016/j.atmosenv.2019.04.024, 2019.

Reid, J. P.; Bertram, A. K.; Topping, D. O.; Laskin, A.; Martin, S. T.; Petters, M. D.; Pope, F. D.; Rovelli, G.: The Viscosity of Atmospherically Relevant Organic Particles. *Nat Commun*, *9* (1), 956. doi:/10.1038/s41467-018-03027-z, 2018.

Riccobono, F.; Schobesberger, S.; Scott, C. E.; Dommen, J.; Ortega, I. K.; Rondo, L.; Almeida, J.; Amorim, A.; Bianchi, F.; Breitenlechner, M.; David, A.; Downard, A.; Dunne, E. M.; Duplissy, J.; Ehrhart, S.; Flagan, R. C.; Franchin, A.; Hansel, A.; Junninen, H.; Kajos, M.; Keskinen, H.; Kupc, A.; Kürten, A.; Kvashin, A. N.; Laaksonen, A.; Lehtipalo, K.; Makhmutov, V.; Mathot, S.; Nieminen, T.; Onnela, A.; Petäjä, T.; Praplan, A. P.; Santos, F. D.; Schallhart, S.; Seinfeld, J. H.; Sipilä, M.; Spracklen, D. V.; Stozhkov, Y.; Stratmann, F.; Tomé, A.; Tsagkogeorgas, G.; Vaattovaara, P.; Viisanen, Y.; Vrtala, A.; Wagner, P. E.; Weingartner, E.; Wex, H.; Wimmer, D.; Carslaw, K. S.; Curtius, J.; Donahue, N. M.; Kirkby, J.; Kulmala, M.; Worsnop, D. R.; Baltensperger, U.: Oxidation Products of Biogenic Emissions Contribute to Nucleation of Atmospheric Particles. *Science*, *344* (6185), 717–721. doi:/10.1126/science.1243527, 2014.

Riipinen, I.; Pierce, J. R.; Yli-Juuti, T.; Nieminen, T.; Häkkinen, S.; Ehn, M.; Junninen, H.; Lehtipalo, K.; Petäjä, T.; Slowik, J.; Chang, R.; Shantz, N. C.; Abbatt, J.; Leaitch, W. R.; Kerminen, V.-M.; Worsnop, D. R.; Pandis, S. N.; Donahue, N. M.; Kulmala, M.: Organic

Condensation: A Vital Link Connecting Aerosol Formation to Cloud Condensation Nuclei (CCN) Concentrations. *Atmos. Chem. Phys.*, *11* (8), 3865–3878. doi:/10.5194/acp-11-3865-2011, 2011.

Riva, M.; Rantala, P.; Krechmer, J. E.; Peräkylä, O.; Zhang, Y.; Heikkinen, L.; Garmash, O.; Yan, C.; Kulmala, M.; Worsnop, D.; Ehn, M.: Evaluating the Performance of Five Different Chemical Ionization Techniques for Detecting Gaseous Oxygenated Organic Species. *Atmos. Meas. Tech.*, *12* (4), 2403–2421. doi:/10.5194/amt-12-2403-2019, 2019.

Rolph, G. D.: Real-time Environmental Applications and Display sYstem (READY), NOAA Air Resources Laboratory, Silver Spring, MD, 2012.

Rose, C.; Sellegri, K.; Moreno, I.; Velarde, F.; Ramonet, M.; Weinhold, K.; Krejci, R.; Andrade, M.; Wiedensohler, A.; Ginot, P.; Laj, P.: CCN Production by New Particle Formation in the Free Troposphere. *Atmos. Chem. Phys.*, *17* (2), 1529–1541. doi:/10.5194/acp-17-1529-2017, 2017.

Rosenfeld, D.; Andreae, M. O.; Asmi, A.; Chin, M.; de Leeuw, G.; Donovan, D. P.; Kahn, R.; Kinne, S.; Kivekäs, N.; Kulmala, M.; Lau, W.; Schmidt, K. S.; Suni, T.; Wagner, T.; Wild, M.; Quaas, J.: Global Observations of Aerosol-Cloud-Precipitation-Climate Interactions. *Rev. of Geophys.*, *52* (4), 750–808. doi:10.1002/2013RG000441, 2014

Ruiz-Jimenez, J.; Okuljar, M.; Sietiö, O.-M.; Demaria, G.; Liangsupree, T.; Zagatti, E.; Aalto, J.; Hartonen, K.; Heinonsalo, J.; Bäck, J.; Petäjä, T.; Riekkola, M.-L.: Determination of Free Amino Acids, Saccharides, and Selected Microbes in Biogenic Atmospheric Aerosols – Seasonal Variations, Particle Size Distribution, Chemical and Microbial Relations. *Atmos. Chem. Phys.*, *21* (11), 8775–8790. doi:10.5194/acp-21-8775-2021, 2021.

Schobesberger, S.; Väänänen, R.; Leino, K.; Virkkula, A.; Backman, J.; Pohja, T.; Siivola, E.; Franchin, A.; Mikkilä, J.; Paramonov, M.; Aalto, P.; Krejci, R.; Petaja, T.; Kulmala, M.: Airborne Measurements over the Boreal Forest of Southern Finland during New Particle Formation Events in 2009 and 2010. *Bor. Environ. Res.*, *18*, 145–163, 2013.

Seinfeld, J. H. and Pandis, S. N.: *Atmos. Chem. Phys.*, 2nd ed., John Wiley and Sons, New York, 2006.

Sheridan, P. J.; Delene, D. J.; Ogren, J. A.: Four Years of Continuous Surface Aerosol Measurements from the Department of Energy's Atmospheric Radiation Measurement Program Southern Great Plains Cloud and Radiation Testbed Site. *J. Geophys. Res.: Atmos.*, *106* (D18), 20735–20747. doi:/10.1029/2001JD000785, 2001.

Shiraiwa, M.; Li, Y.; Tsimpidi, A. P.; Karydis, V. A.; Berkemeier, T.; Pandis, S. N.; Lelieveld, J.; Koop, T.; Pöschl, U.: Global Distribution of Particle Phase State in Atmospheric Secondary Organic Aerosols. *Nat. Commun.*, *8* (1), 15002. doi:10.1038/ncomms15002., 2017.

Song, M.; Lee, M.; Kim, J. H.; Yum, S. S.; Lee, G.; Kim, K.-R.: New Particle Formation and Growth in Relation to Vertical Mixing and Chemical Species during ABC-EAREX2005. *Atmos. Res.*, *97* (3), 359–370. doi:/10.1016/j.atmosres.2010.04.013, 2010.

Sprung, D.; Jost, C.; Reiner, T.; Hansel, A.; Wisthaler, A.: Acetone and Acetonitrile in the Tropical Indian Ocean Boundary Layer and Free Troposphere: Aircraft-Based Intercomparison of AP-CIMS and PTR-MS Measurements. *J. Geophys. Res.: Atmos.*, *106* (D22), 28511–28527. doi:/10.1029/2000JD900599, 2001.

Stevens, B.; Feingold, G.: Untangling Aerosol Effects on Clouds and Precipitation in a Buffered System. *Nature*, *461* (7264), 607–613. doi:10.1038/nature08281, 2009.

Stevens, R. G.; Pierce, J. R.: The Contribution of Plume-Scale Nucleation to Global and Regional Aerosol and CCN Concentrations: Evaluation and Sensitivity to Emissions Changes. *Atmos. Chem. Phys.*, *14* (24), 13661–13679. doi:/10.5194/acp-14-13661-2014, 2014.

Stevens, R. G.; Pierce, J. R.; Brock, C. A.; Reed, M. K.; Crawford, J. H.; Holloway, J. S.; Ryerson, T. B.; Huey, L. G.; Nowak, J. B.: Nucleation and Growth of Sulfate Aerosol in Coal-Fired Power Plant Plumes: Sensitivity to Background Aerosol and Meteorology. *Atmos. Chem. Phys.*, *12* (1), 189–206. doi:/10.5194/acp-12-189-2012, 2012.

Subba, T.; Lawler, M. J.; Steiner, A. L.: Estimation of Possible Primary Biological Particle Emissions and Rupture Events at the Southern Great Plains ARM Site. *J. Geophys. Res.: Atmos.*, *126* (16), e2021JD034679. doi:/10.1029/2021JD034679, 2021.

Tong, H.; Liu, F.; Filippi, A.; Wilson, J.; Arangio, A. M.; Zhang, Y.; Yue, S.; Lelieveld, S.; Shen, F.; Keskinen, H.-M. K.; Li, J.; Chen, H.; Zhang, T.; Hoffmann, T.; Fu, P.; Brune, W. H.; Petäjä, T.; Kulmala, M.; Yao, M.; Berkemeier, T.; Shiraiwa, M.; Pöschl, U.: Aqueous-Phase Reactive Species Formed by Fine Particulate Matter from Remote Forests and Polluted Urban Air. *Atmos Chem Phys*, *21* (13), 10439–10455. doi:10.5194/acp-21-10439-2021, 2021.

Trishchenko, A. P., Luo, Y., Latifovic, R., and Li, Z.: Land cover type distribution over the ARM SGP area for atmospheric radiation and environmental research, in: Proceedings of the 14th ARM Science Team Meeting, Albuquerque, New Mexico, 22–26 March, 2004.

Tröstl, J.; Chuang, W. K.; Gordon, H.; Heinritzi, M.; Yan, C.; Molteni, U.; Ahlm, L.; Frege, C.; Bianchi, F.; Wagner, R.; Simon, M.; Lehtipalo, K.; Williamson, C.; Craven, J. S.; Duplissy, J.; Adamov, A.; Almeida, J.; Bernhammer, A.-K.; Breitenlechner, M.; Brilke, S.; Dias, A.; Ehrhart, S.; Flagan, R. C.; Franchin, A.; Fuchs, C.; Guida, R.; Gysel, M.; Hansel, A.; Hoyle, C. R.; Jokinen, T.; Junninen, H.; Kangasluoma, J.; Keskinen, H.; Kim, J.; Krapf, M.; Kürten, A.; Laaksonen, A.; Lawler, M.; Leiminger, M.; Mathot, S.; Möhler, O.; Nieminen, T.; Onnela, A.; Petäjä, T.; Piel, F. M.; Miettinen, P.; Rissanen, M. P.; Rondo, L.; Sarnela, N.; Schobesberger, S.; Sengupta, K.; Sipilä, M.; Smith, J. N.; Steiner, G.; Tomè, A.; Virtanen, A.; Wagner, A. C.; Weingartner, E.; Wimmer, D.; Winkler, P. M.; Ye, P.; Carslaw, K. S.; Curtius, J.; Dommen, J.; Kirkby, J.; Kulmala, M.; Riipinen, I.; Worsnop, D. R.; Donahue, N. M.; Baltensperger, U.: The Role of Low-Volatility Organic Compounds in Initial Particle Growth in the Atmosphere. *Nature*, *533* (7604), 527–531. doi:/10.1038/nature18271, 2016.

Twomey, S.: Pollution and the planetary albedo, *Atmos. Environ.*, 8(12), 1251–1256, doi:10.1016/0004-6981(74)90004-3, 1974.

Uin, J.; Aiken, A. C.; Dubey, M. K.; Kuang, C.; Pekour, M.; Salwen, C.; Sedlacek, A. J.; Senum, G.; Smith, S.; Wang, J.; Watson, T. B.; Springston, S. R.: Atmospheric Radiation Measurement (ARM) Aerosol Observing Systems (AOS) for Surface-Based In Situ Atmospheric Aerosol and Trace Gas Measurements. *J. Atmos. Oce. Technol.*, *36* (12), 2429–2447. doi:/10.1175/JTECH-D-19-0077.1, 2019.

Wang, J.; Krejci, R.; Giangrande, S.; Kuang, C.; Barbosa, H. M. J.; Brito, J.; Carbone, S.; Chi, X.; Comstock, J.; Ditas, F.; Lavric, J.; Manninen, H. E.; Mei, F.; Moran-Zuloaga, D.; Pöhlker, C.; Pöhlker, M. L.; Saturno, J.; Schmid, B.; Souza, R. A. F.; Springston, S. R.; Tomlinson, J. M.;

Toto, T.; Walter, D.; Wimmer, D.; Smith, J. N.; Kulmala, M.; Machado, L. A. T.; Artaxo, P.; Andreae, M. O.; Petäjä, T.; Martin, S. T.: Amazon Boundary Layer Aerosol Concentration Sustained by Vertical Transport during Rainfall, *Nature*, *539* (7629), 416–419. doi:10.1038/nature19819, 2016.

Wang, M.; Kong, W.; Marten, R.; He, X.-C.; Chen, D.; Pfeifer, J.; Heitto, A.; Kontkanen, J.; Dada, L.; Kürten, A.; Yli-Juuti, T.; Manninen, H. E.; Amanatidis, S.; Amorim, A.; Baalbaki, R.; Baccarini, A.; Bell, D. M.; Bertozzi, B.; Bräkling, S.; Brilke, S.; Murillo, L. C.; Chiu, R.; Chu, B.; De Menezes, L.-P.; Duplissy, J.; Finkenzeller, H.; Carracedo, L. G.; Granzin, M.; Guida, R.; Hansel, A.; Hofbauer, V.; Krechmer, J.; Lehtipalo, K.; Lamkaddam, H.; Lampimäki, M.; Lee, C. P.; Makhmutov, V.; Marie, G.; Mathot, S.; Mauldin, R. L.; Mentler, B.; Müller, T.; Onnela, A.; Partoll, E.; Petäjä, T.; Philippov, M.; Pospisilova, V.; Ranjithkumar, A.; Rissanen, M.; Rörup, B.; Scholz, W.; Shen, J.; Simon, M.; Sipilä, M.; Steiner, G.; Stolzenburg, D.; Tham, Y. J.; Tomé, A.; Wagner, A. C.; Wang, D. S.; Wang, Y.; Weber, S. K.; Winkler, P. M.; Wlasits, P. J.; Wu, Y.; Xiao, M.; Ye, Q.; Zauner-Wieczorek, M.; Zhou, X.; Volkamer, R.; Riipinen, I.; Dommen, J.; Curtius, J.; Baltensperger, U.; Kulmala, M.; Worsnop, D. R.; Kirkby, J.; Seinfeld, J. H.; El-Haddad, I.; Flagan, R. C.; Donahue, N. M.: Rapid Growth of New Atmospheric Particles by Nitric Acid and Ammonia Condensation. *Nature*, *581* (7807), 184–189. doi:10.1038/s41586-020-2270-4, 2020.

Wehner, B.; Siebert, H.; Ansmann, A.; Ditas, F.; Seifert, P.; Stratmann, F.; Wiedensohler, A.; Apituley, A.; Shaw, R. A.; Manninen, H. E.; Kulmala, M.: Observations of Turbulence-Induced New Particle Formation in the Residual Layer. *Atmos. Chem. Phys.*, *10* (9), 4319–4330. doi:/10.5194/acp-10-4319-2010, 2010.

Wehner, B.; Siebert, H.; Stratmann, F.; Tuch, T.; Wiedensohler, A.; PetäJä, T.; Dal Maso, M.; Kulmala, M.: Horizontal Homogeneity and Vertical Extent of New Particle Formation Events. *Tellus-B: Chem. Phys. Meteorol.*, *59* (3), 362–371. doi:/10.1111/j.1600-0889.2007.00260.x, 2007.

Yu, H.; Dai, L.; Zhao, Y.; Kanawade, V. P.; Tripathi, S. N.; Ge, X.; Chen, M.; Lee, S.-H.: Laboratory Observations of Temperature and Humidity Dependencies of Nucleation and Growth Rates of Sub-3 Nm Particles. *J. Geophys. Res.: Atmos. 122* (3), 1919–1929. doi:/10.1002/2016JD025619, 2017.

Zauner-Wieczorek, M.; Curtius, J.; Kürten, A.: The Ion-Ion Recombination Coefficient α: Comparison of Temperature- and Pressure-Dependent Parameterisations for the Troposphere and Lower Stratosphere. *Atmos. Chem. Phys. Dis.* 1–31. doi:10.5194/acp-2021-795, 2021.

Zaveri, R. A.; Easter, R. C.; Shilling, J. E.; Seinfeld, J. H.: Modeling Kinetic Partitioning of Secondary Organic Aerosol and Size Distribution Dynamics: Representing Effects of Volatility, Phase State, and Particle-Phase Reaction. *Atmos. Chem. Phys.*, *14* (10), 5153–5181. doi:/10.5194/acp-14-5153-2014, 2014.

Zaveri, R. A.; Shilling, J. E.; Zelenyuk, A.; Liu, J.; Bell, D. M.; D'Ambro, E. L.; Gaston, C. J.; Thornton, J. A.; Laskin, A.; Lin, P.; Wilson, J.; Easter, R. C.; Wang, J.; Bertram, A. K.; Martin, S. T.; Seinfeld, J. H.; Worsnop, D. R.: Growth Kinetics and Size Distribution Dynamics of Viscous Secondary Organic Aerosol. *Environ. Sci. Technol.*, *52* (3), 1191–1199. doi:10.1021/acs.est.7b04623, 2018.

Zhao, B.; Shrivastava, M.; Donahue, N. M.; Gordon, H.; Schervish, M.; Shilling, J. E.; Zaveri, R. A.; Wang, J.; Andreae, M. O.; Zhao, C.; Gaudet, B.; Liu, Y.; Fan, J.; Fast, J. D.: High Concentration of Ultrafine Particles in the Amazon Free Troposphere Produced by Organic New Particle Formation. *Proceedings of the National Academy of Sciences*, *117* (41), 25344–25351. doi:10.1073/pnas.2006716117, 2020.

APPENDIX A

OH PROXIES

Stevens et al. 2012

$$x = log([NO_x]) - 0.195 \quad (1)$$

$$y = \frac{dswrf}{S_0 \cdot T} \quad (2)$$

$$P1 = -0.014x^6 + 0.0027x^5 + 0.1713x^4 - 0.0466x^3 - 0.7893x^2 - 0.1739x + 6.9414 \quad (3)$$

$$P2 = (-1345y^3 + 4002y^2 - 471.8y + 42.72) \times 10^4 \quad (4)$$

$$[OH] = 0.82 \cdot 10^{P1 \times log(P2)/6.8} \quad [molec/cm^3] \quad (5)$$

Pietikäinen et al. 2014

$$[OH] = 3081.0 \cdot (SWF \downarrow)^{0.8397} \quad \text{[day time]} \quad (6)$$

$$[OH] = 6.033 \times 10^4 \quad \text{[night time]} \quad (7)$$

APPENDIX B

SUPPLEMENTAL MATERIALS

Table S1. We used the low NO_X (nitric oxide + nitrogen dioxide) SOM parameters for each species class from Bilsback et al., (in prep). ΔLVP: logarithmic change in vapor pressure from the addition of one oxygen atom (see C* calculation). P1-P4: molar yields of functionalized products from the addition of one to four oxygen atoms. mFRAG: tunable exponent used in fragmentation probability calculations. kOH: OH reaction coefficient [cm^{-3} $molec^{-1}$ s^{-1}]. fHOM: HOM mass yields from the five precursor classes (Bianchi et al., 2019).

SOM-Grid	ΔLVP	P1	P2	P3	P4	mFRAG	kOH	fHOM
Benzene	2.075	0.514	0.087	0.207	0.193	0.001	1.22E-12	0.002
Toluene	1.966	0.694	0.031	0.002	0.273	0.001	5.63E-12	0.001
Xylenes	1.755	0.440	0.128	0.016	0.416	0.061	2.31E-11	0.014
Isoprene	2.254	0.576	0.053	0.356	0.016	0.015	1.00E-10	0.000
Terpene	1.571	0.361	0.007	0.606	0.026	0.087	5.23E-11	0.034

Each SOM grid has 6 pre-fitted parameters (outlined in Table S1) that track the movement of species through the grid (Bilsback et al., in prep). The ΔLVP (logarithmic change in vapor pressure) value determines the associated reduction in volatility with the addition of one oxygen atom. The P1, P1, P3, and P4 values are the molar yields of the functionalized products with either one, two, three, or four oxygen atoms added to the existing molecule, respectively. mFRAG is a tunable parameter that dictates the probability of fragmentation (P_{frag}). P_{frag} is defined as $P_{frag} = (N_O : N_C)^{mFRAG}$. The volatility (C*) of the species in each grid cell is determined by $C^* = 10^{(-0.0337 * MW\_hc + 11.56 - No * \Delta LVP)}$, where MW_hc is the molecular weight of the hydrocarbon backbone (including only the carbon and hydrogen atoms). Finally, f_{HOM} is the yield of HOMs formed directly from the reaction of precursor species with OH. f_{HOM} yields for SOA precursors in this work are based on yields compiled in Bianchi et al. (2019). For this work, HOMs are considered to be completely non-volatile and non-reactive.

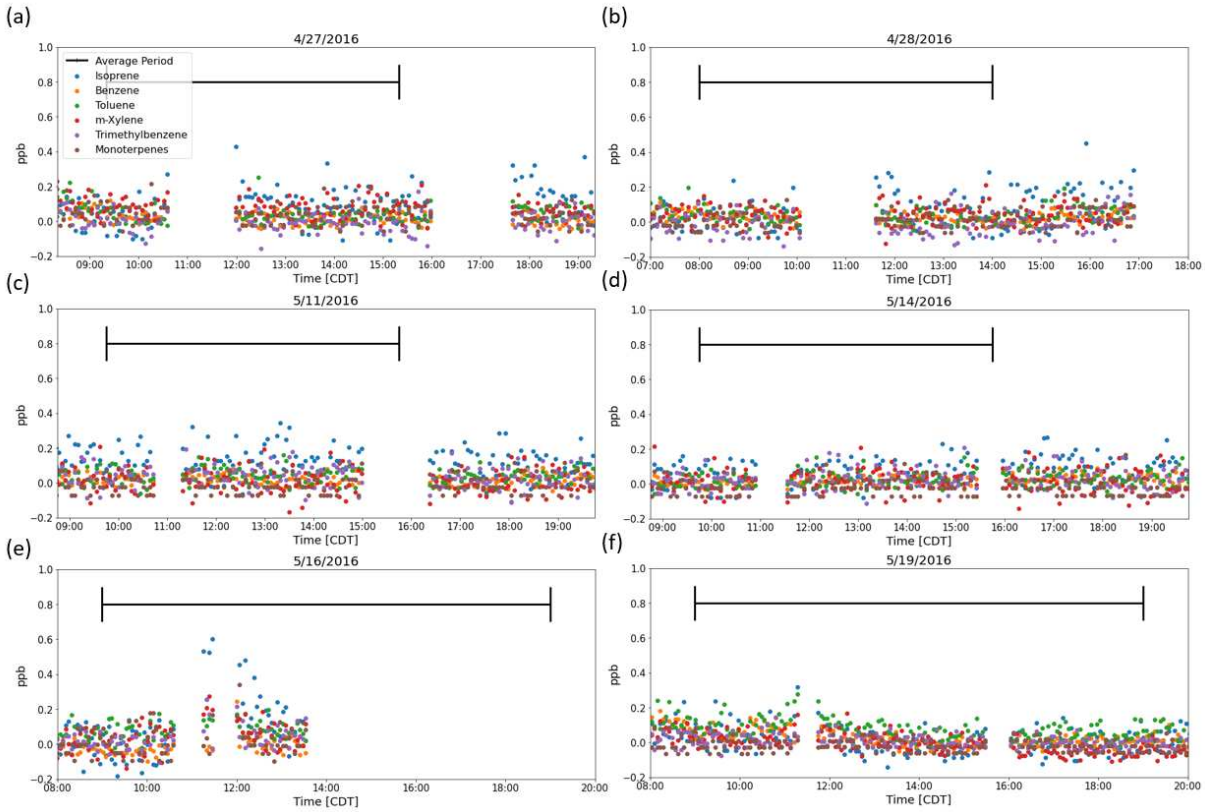

S1. (a-f) Time series of gas-phase organic species measured by the PT-RMS for each day simulated. Averaging periods are shown by the black lines.

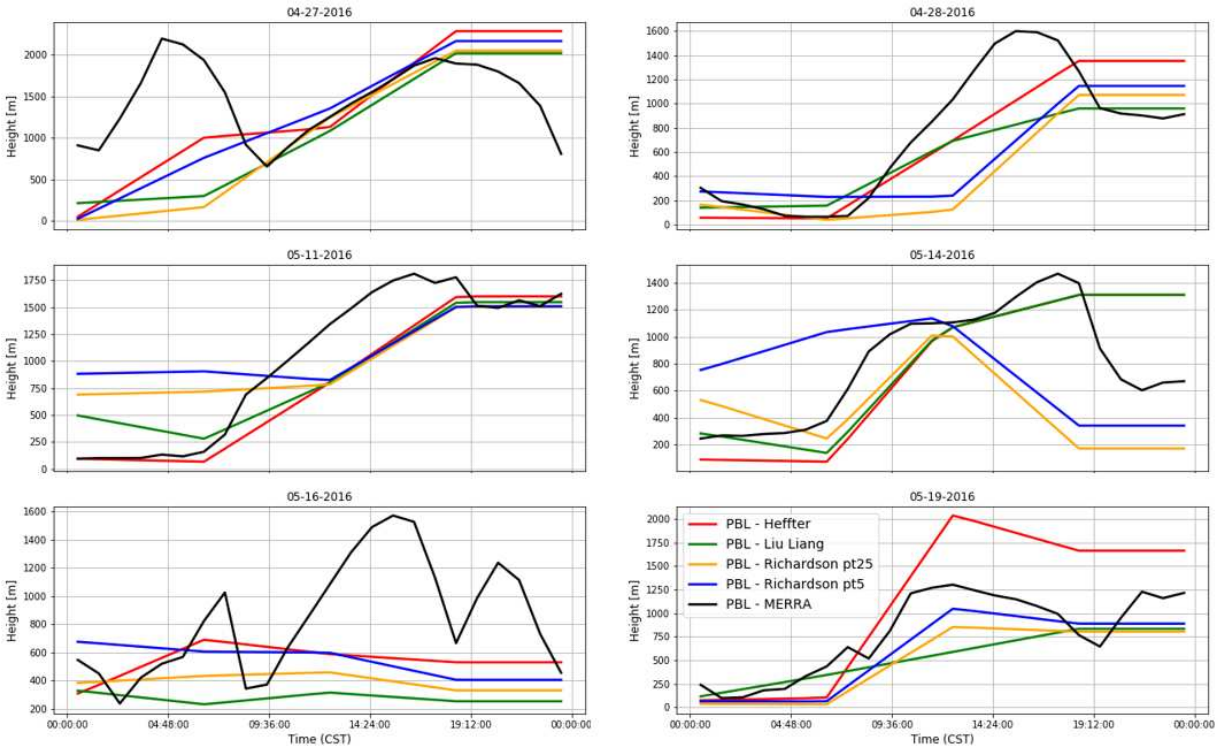

S2. mixed layer heights from MERRA-2 reanalysis data (black lines) and from radiosonde soundings at the SGP observatory. For this work, we used mixed layer heights derived from the radiosonde soundings using the method from Liu and Lang (2010: green lines).

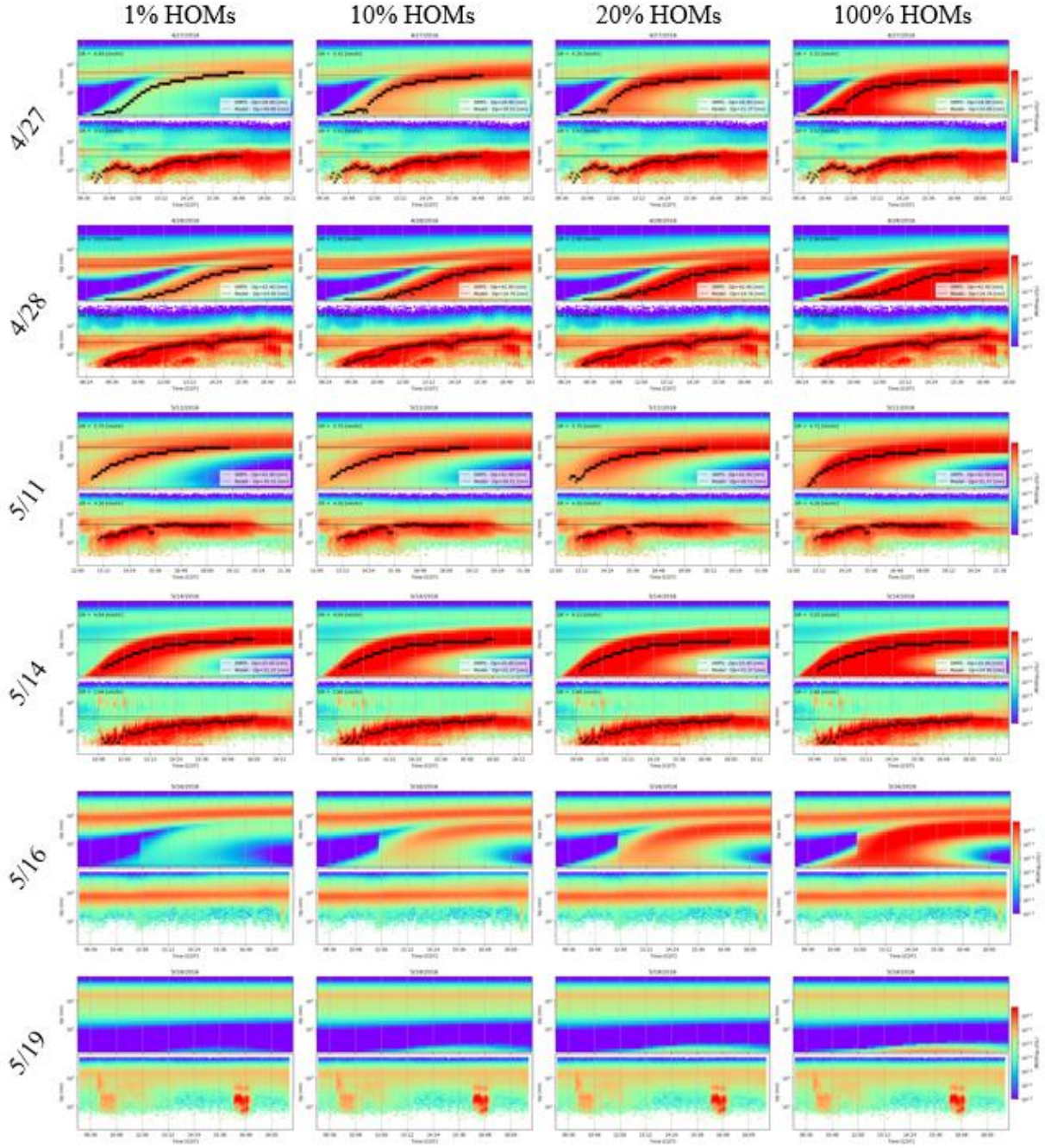

S3. Simulated (top panels) and observed (bottom panels) aerosol size distributions from sensitivity simulations testing the contribution of HOMs to the organic-sulfuric acid NPF scheme.

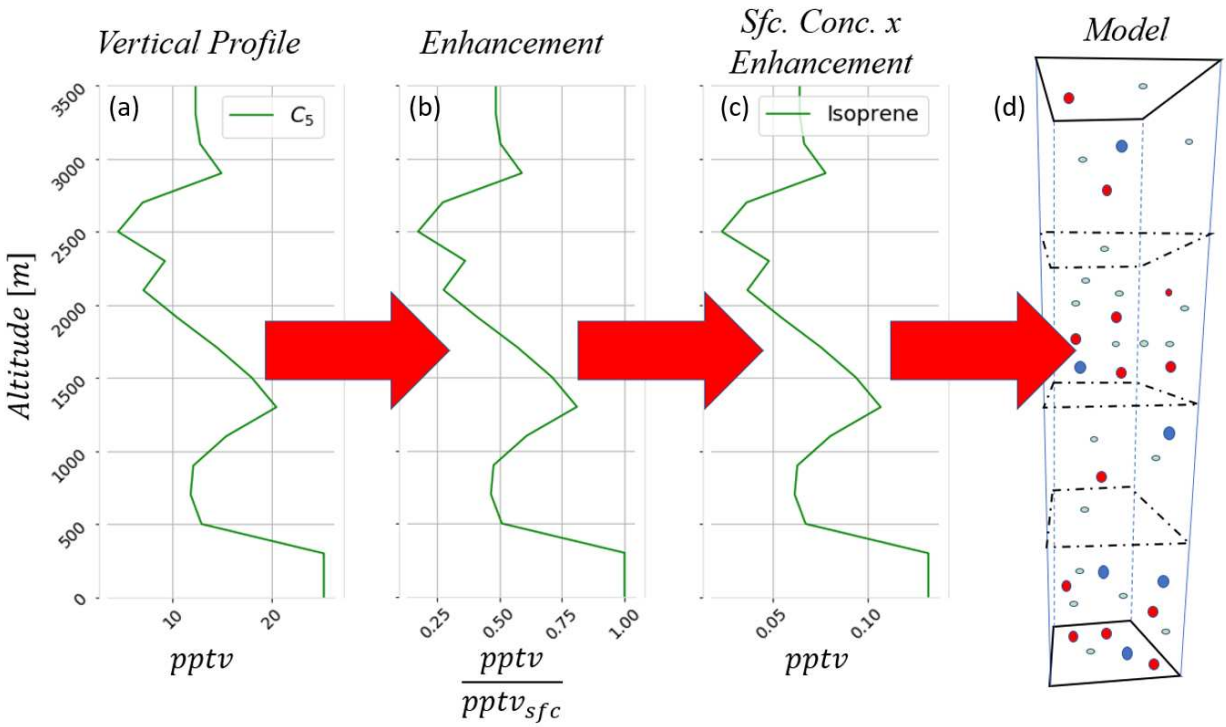

S4. (a) Example vertical profile of a C_5 species as measured by the HRToF-CIMS, interpolated to the surface. (b) Vertical profile of C_5 species normalized by the concentrations in the lowest 200 m of the profile. The multiple profiles of C_5 species are normalized to get relative vertical enhancements, and then the normalized enhancement profiles are averaged together. (c) The single normalized enhancement profile of C_5 species is then multiplied by the surface concentration of isoprene measured by the PTR-MS. (d) The corresponding model layers are initialized with the derived vertical profile of isoprene (and other gas-phase species indicated by the different colored dots).

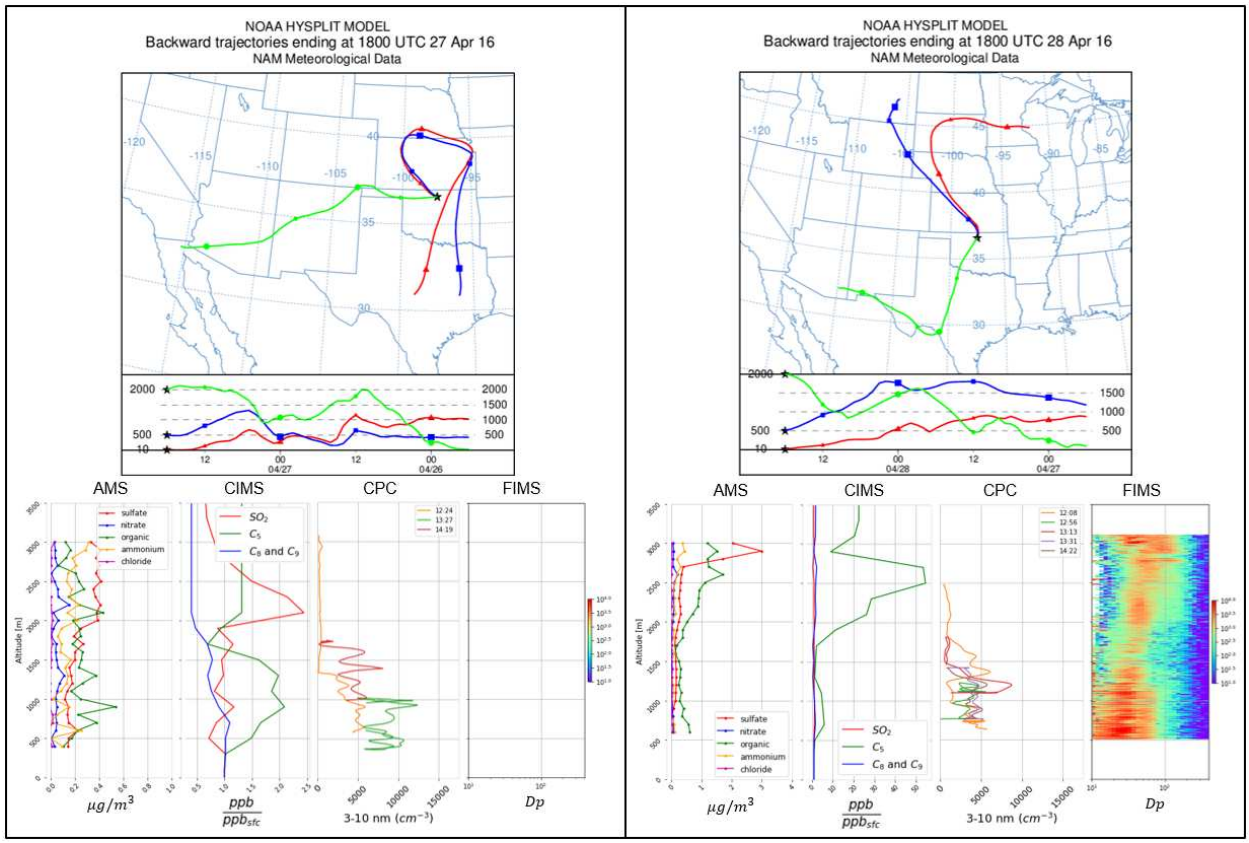

S5. (a-b) Top panels show HYSPLIT back trajectories starting at 10, 500, and 2000 m above the SGP ground site starting at 18:00 UTC (13:00 CDT). The leftmost bottom panels show the average vertical profiles of sulfate, nitrate, organic, ammonium, and chloride aerosol mass [µg m^{-3}] measured using an aerosol mass spectrometer (AMS) on the aircraft. The second from the left panels on the bottom show the derived vertical enhancement profiles of SO_2, C_5 species, and C_8+C_9 species measured by the HRToF-CIMS. The third from the left panels on the bottom show the vertical profiles of 3-10 nm particle number concentrations [# cm^{-3}]. Finally, the bottom right panels show the vertical profiles of FIMS data. All four panels on the bottom share a common y-axis for comparison.

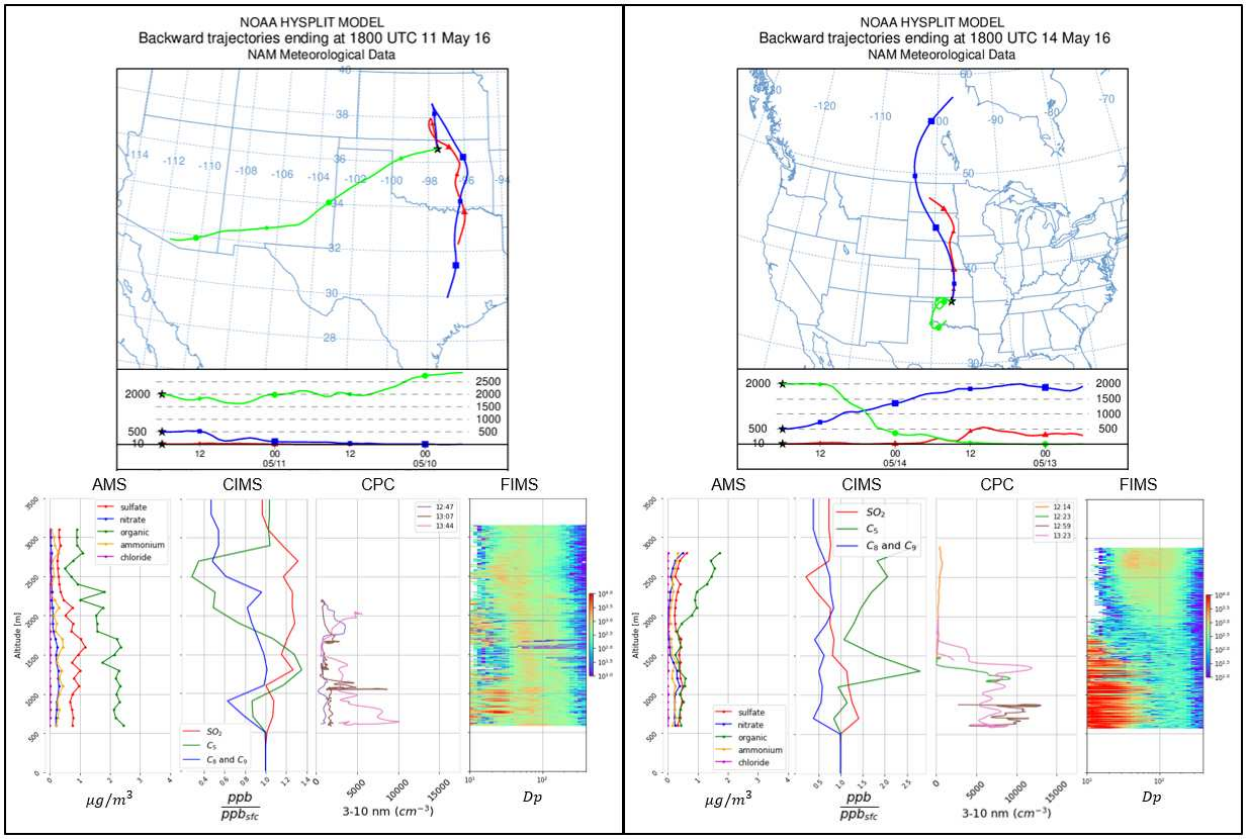

S5. (c-d) Top panels show HYSPLIT back trajectories starting at 10, 500, and 2000 m above the SGP ground site starting at 18:00 UTC (13:00 CDT). The leftmost bottom panels show the average vertical profiles of sulfate, nitrate, organic, ammonium, and chloride aerosol mass [μg m^{-3}] measured using an aerosol mass spectrometer (AMS) on the aircraft. The second from the left panels on the bottom show the derived vertical enhancement profiles of SO_2, C_5 species, and C_8+C_9 species measured by the HRToF-CIMS. The third from the left panels on the bottom show the vertical profiles of 3-10 nm particle number concentrations [# cm^{-3}]. Finally, the bottom right panels show the vertical profiles of FIMS data. All four panels on the bottom share a common y-axis for comparison.

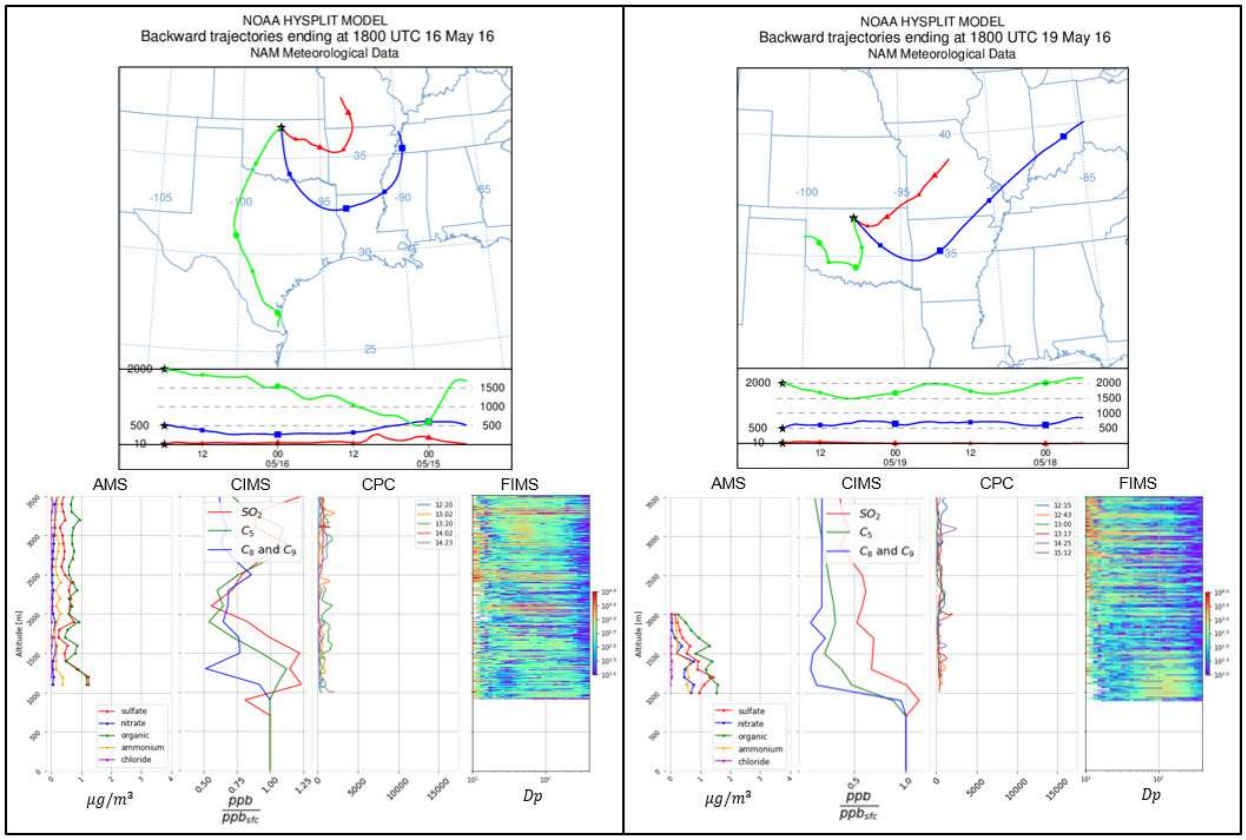

S5. (e-f) Top panels show HYSPLIT back trajectories starting at 10, 500, and 2000 m above the SGP ground site starting at 18:00 UTC (13:00 CDT). The leftmost bottom panels show the average vertical profiles of sulfate, nitrate, organic, ammonium, and chloride aerosol mass [µg m^{-3}] measured using an aerosol mass spectrometer (AMS) on the aircraft. The second from the left panels on the bottom show the derived vertical enhancement profiles of SO_2, C_5 species, and C_8+C_9 species measured by the HRToF-CIMS. The third from the left panels on the bottom show the vertical profiles of 3-10 nm particle number concentrations [# cm^{-3}]. Finally, the bottom right panels show the vertical profiles of FIMS data. All four panels on the bottom share a common y-axis for comparison.

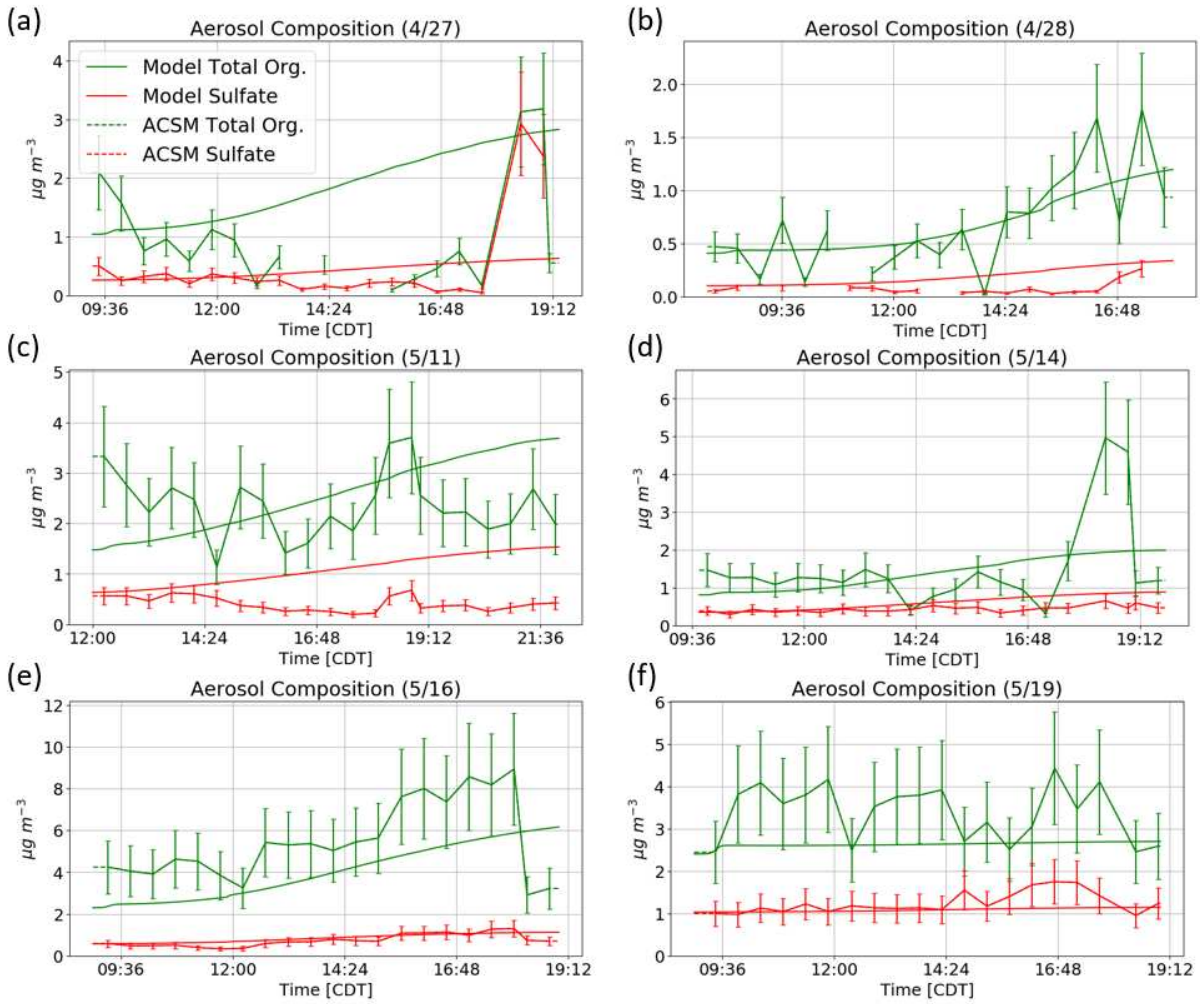

S6. (a-f) Lines with error bars show the total organic (green) and sulfate (red) aerosol mass observed by the ACSM at the SGP observatory. To be consistent with the instrument handbook, ± 30% error bars are included for the ACSM data. The solid lines indicate the simulated total organic (green) and sulfate (red) aerosol mass.

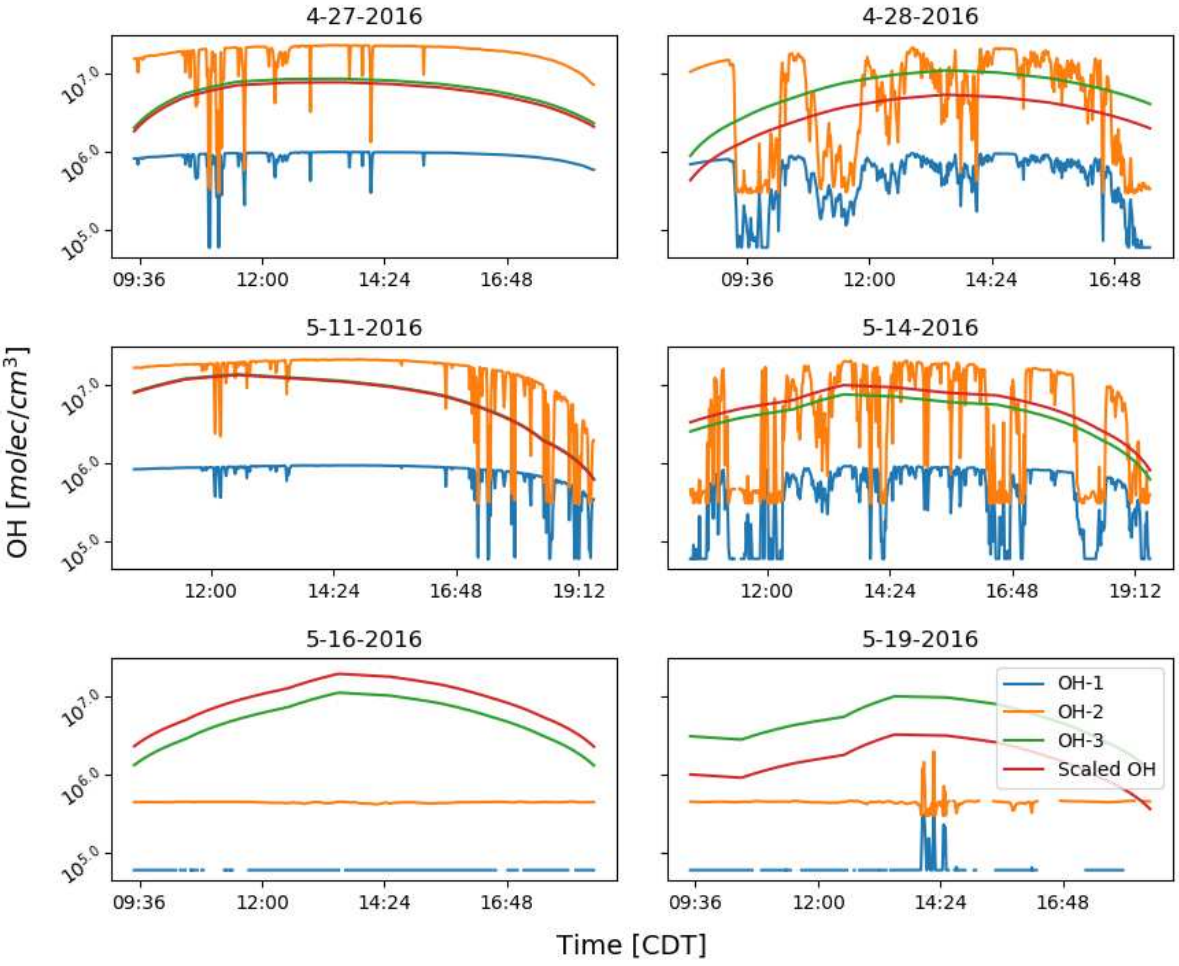

S7. OH concentrations at the surface for each simulation day. OH-1 (blue lines) is from Pietikäinen et al. (2014), and is based on downwelling shortwave irradiance. OH-2 (orange lines) is from Stevens et al. (2012), and is based on downwelling shortwave irradiance and NO_x concentrations. OH-3 is the raw output from a GEOS-Chem nested grid simulation over the central US. Finally, Scaled OH is OH-3 multiplied by the scale factors outlined in Table 1 which are based on the ratio of observed and modeled OA production rates.

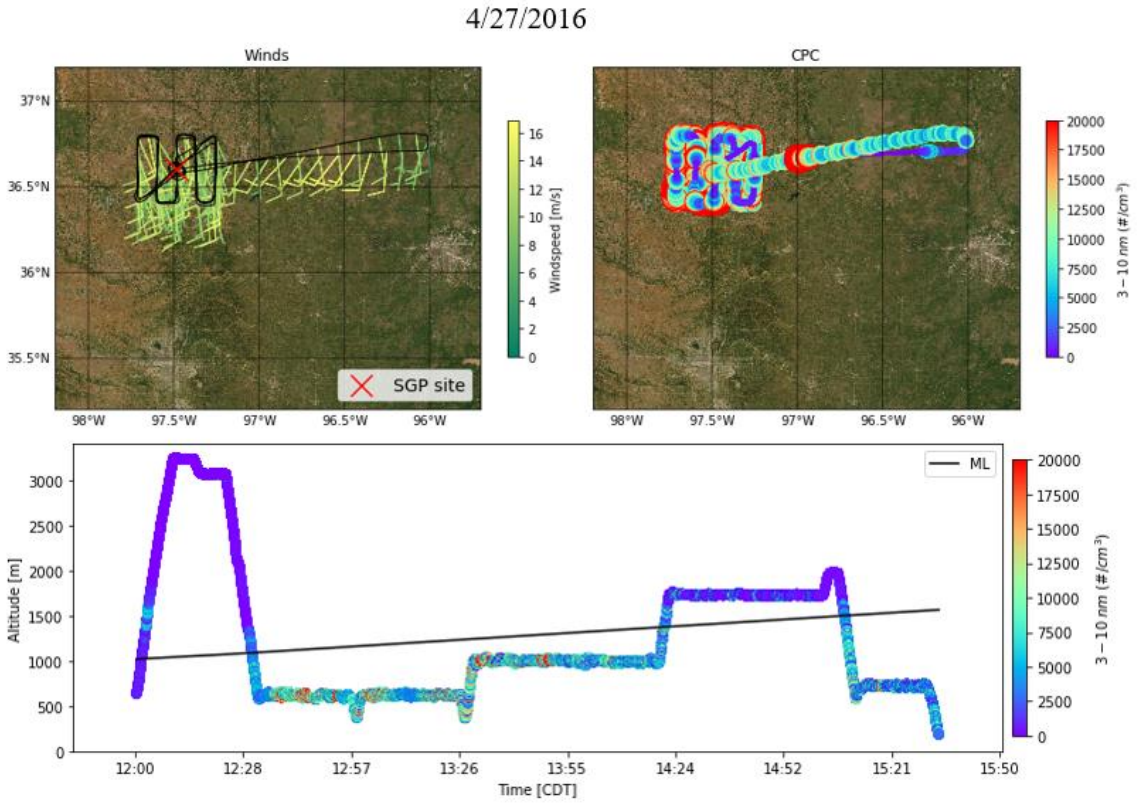

S8 (a). Top left panel shows the horizontal flight path (black line) and wind barbs for the flight on 27 April. The location of the SGP ground site is indicated by the red 'X'. Top right panel shows the horizontal flight path with the color and size of the markers indicating the 3-10 nm particle number concentration derived from the CPC data. The bottom panel shows the vertical flight path (y-axis) in time (x-axis), and the markers are colored using the same CPC data as the top right panel. Additionally, the height of the mixed layer (linearly interpolated between radiosonde launches) is shown by the black solid line.

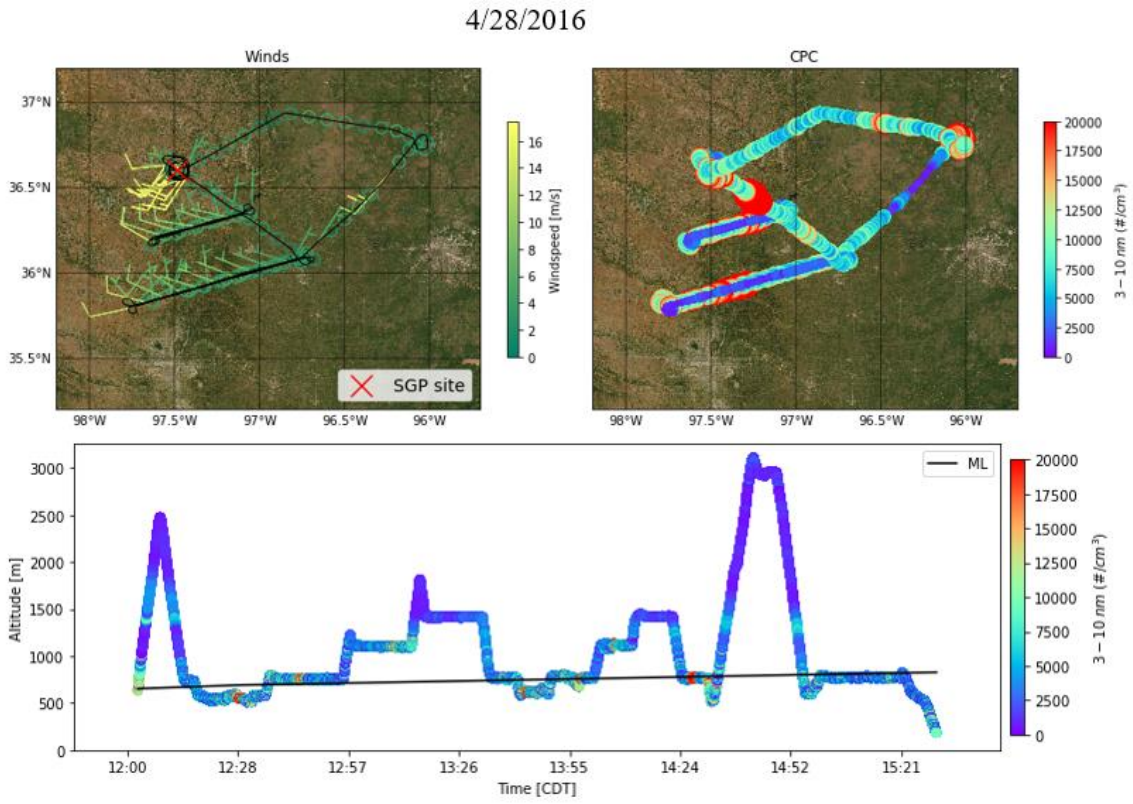

S8 (b). Top left panel shows the horizontal flight path (black line) and wind barbs for the flight on 28 April. The location of the SGP ground site is indicated by the red 'X'. Top right panel shows the horizontal flight path with the color and size of the markers indicating the 3-10 nm particle number concentration derived from the CPC data. The bottom panel shows the vertical flight path (y-axis) in time (x-axis), and the markers are colored using the same CPC data as the top right panel. Additionally, the height of the mixed layer (linearly interpolated between radiosonde launches) is shown by the black solid line.

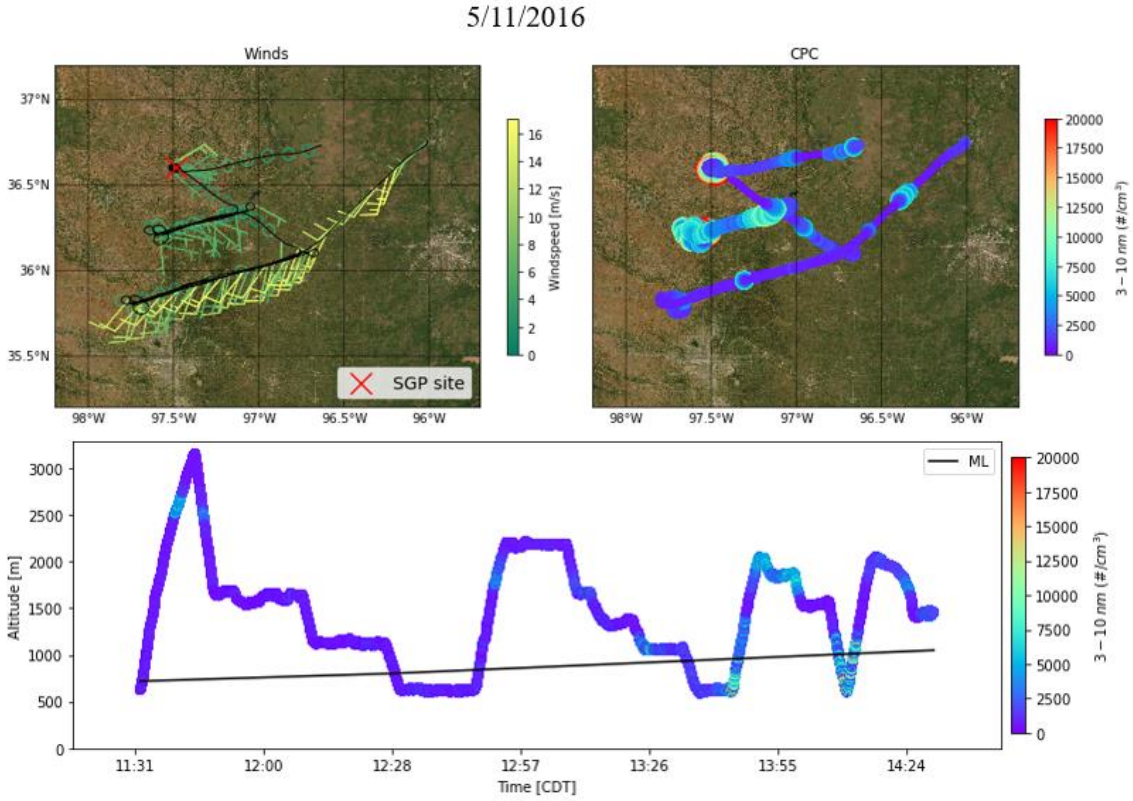

S8 (c). Top left panel shows the horizontal flight path (black line) and wind barbs for the flight on 11 May. The location of the SGP ground site is indicated by the red 'X'. Top right panel shows the horizontal flight path with the color and size of the markers indicating the 3-10 nm particle number concentration derived from the CPC data. The bottom panel shows the vertical flight path (y-axis) in time (x-axis), and the markers are colored using the same CPC data as the top right panel. Additionally, the height of the mixed layer (linearly interpolated between radiosonde launches) is shown by the black solid line.

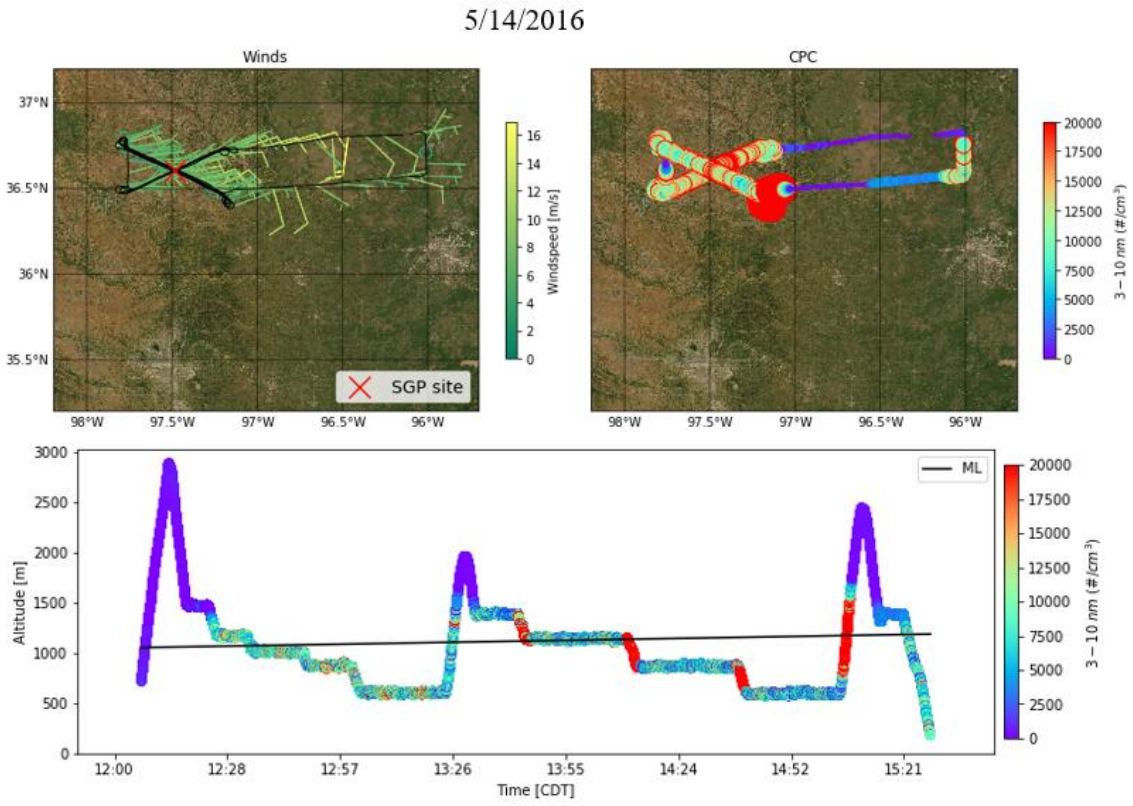

S8 (d). Top left panel shows the horizontal flight path (black line) and wind barbs for the flight on 14 May. The location of the SGP ground site is indicated by the red 'X'. Top right panel shows the horizontal flight path with the color and size of the markers indicating the 3-10 nm particle number concentration derived from the CPC data. The bottom panel shows the vertical flight path (y-axis) in time (x-axis), and the markers are colored using the same CPC data as the top right panel. Additionally, the height of the mixed layer (linearly interpolated between radiosonde launches) is shown by the black solid line.

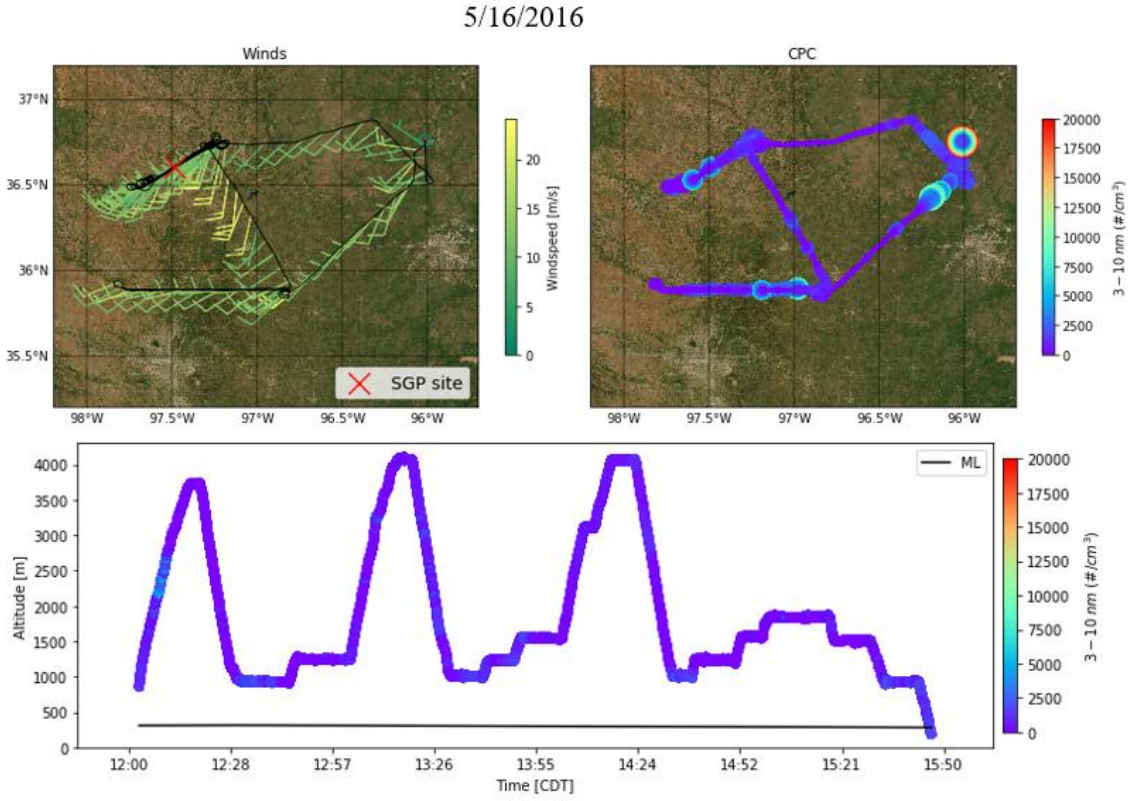

S8 (e). Top left panel shows the horizontal flight path (black line) and wind barbs for the flight on 16 May. The location of the SGP ground site is indicated by the red 'X'. Top right panel shows the horizontal flight path with the color and size of the markers indicating the 3-10 nm particle number concentration derived from the CPC data. The bottom panel shows the vertical flight path (y-axis) in time (x-axis), and the markers are colored using the same CPC data as the top right panel. Additionally, the height of the mixed layer (linearly interpolated between radiosonde launches) is shown by the black solid line.

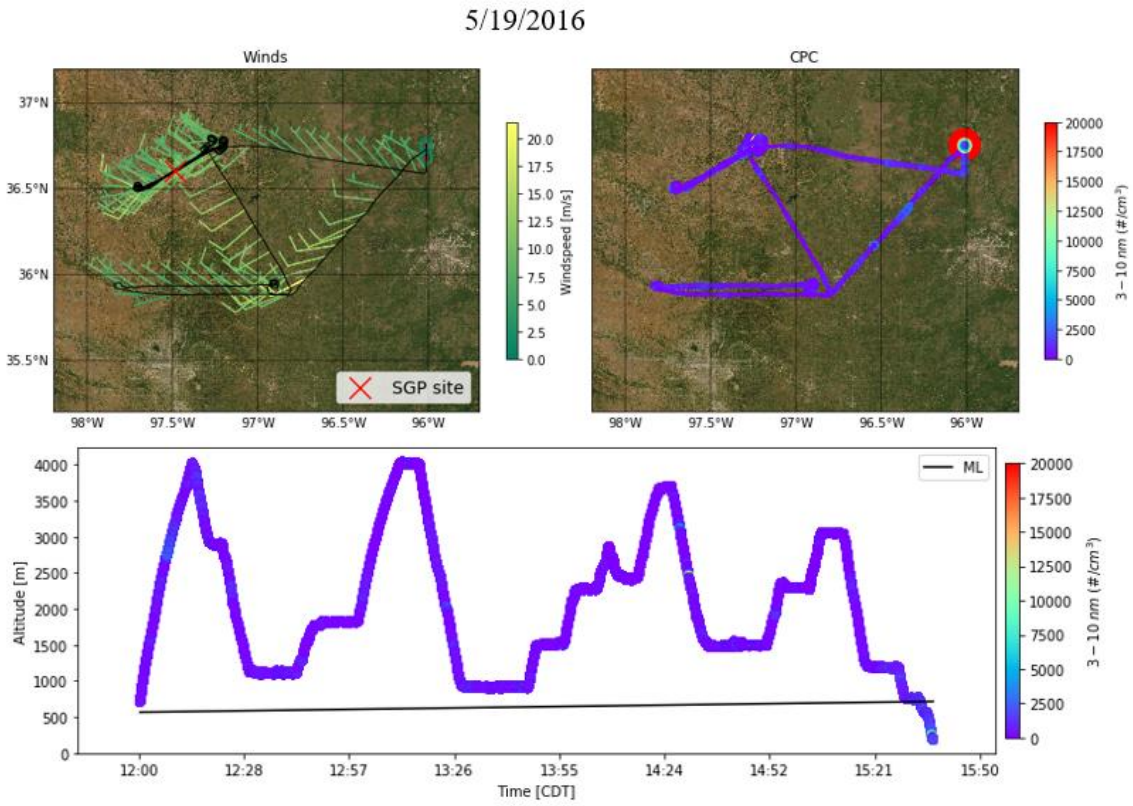

S8 (f). Top left panel shows the horizontal flight path (black line) and wind barbs for the flight on 19 May. The location of the SGP ground site is indicated by the red 'X'. Top right panel shows the horizontal flight path with the color and size of the markers indicating the 3-10 nm particle number concentration derived from the CPC data. The bottom panel shows the vertical flight path (y-axis) in time (x-axis), and the markers are colored using the same CPC data as the top right panel. Additionally, the height of the mixed layer (linearly interpolated between radiosonde launches) is shown by the black solid line.

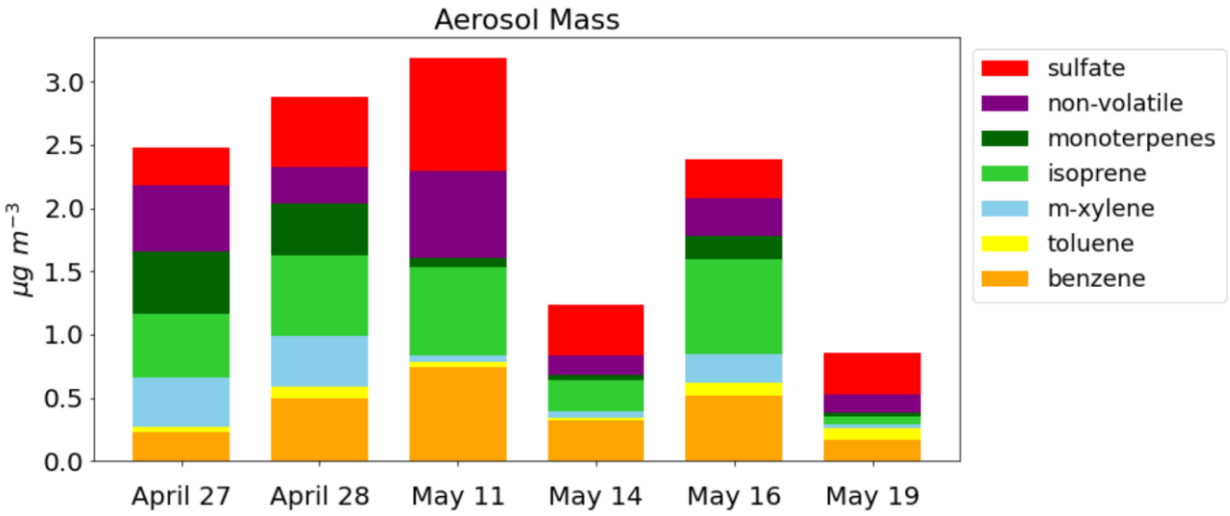

S9. The total change in OA mass during each simulation period (bar height), and the breakdown of the contribution from each precursor class (colors) at the surface. Toluene generally contributes the least to the change in OA mass change, and the dominant contributor varies from day to day. The mass in the purple bars is primarily HOMs, and the primary contributor to the HOM concentrations are the gas-phase monoterpenes.

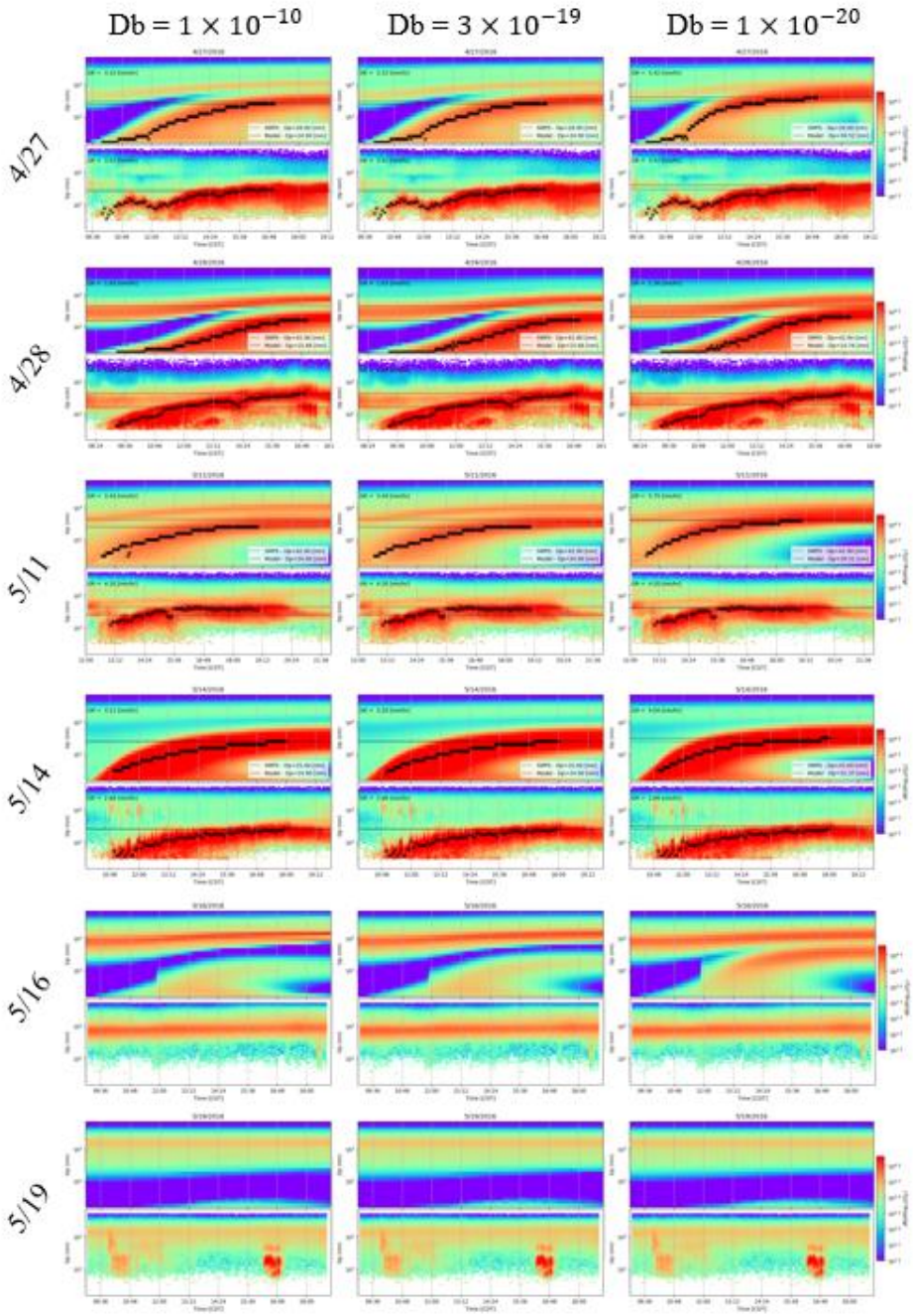

S10. Comparisons of the simulated (top panels) and observed (bottom panels) aerosol size distributions from sensitivity simulations testing particle phase state.

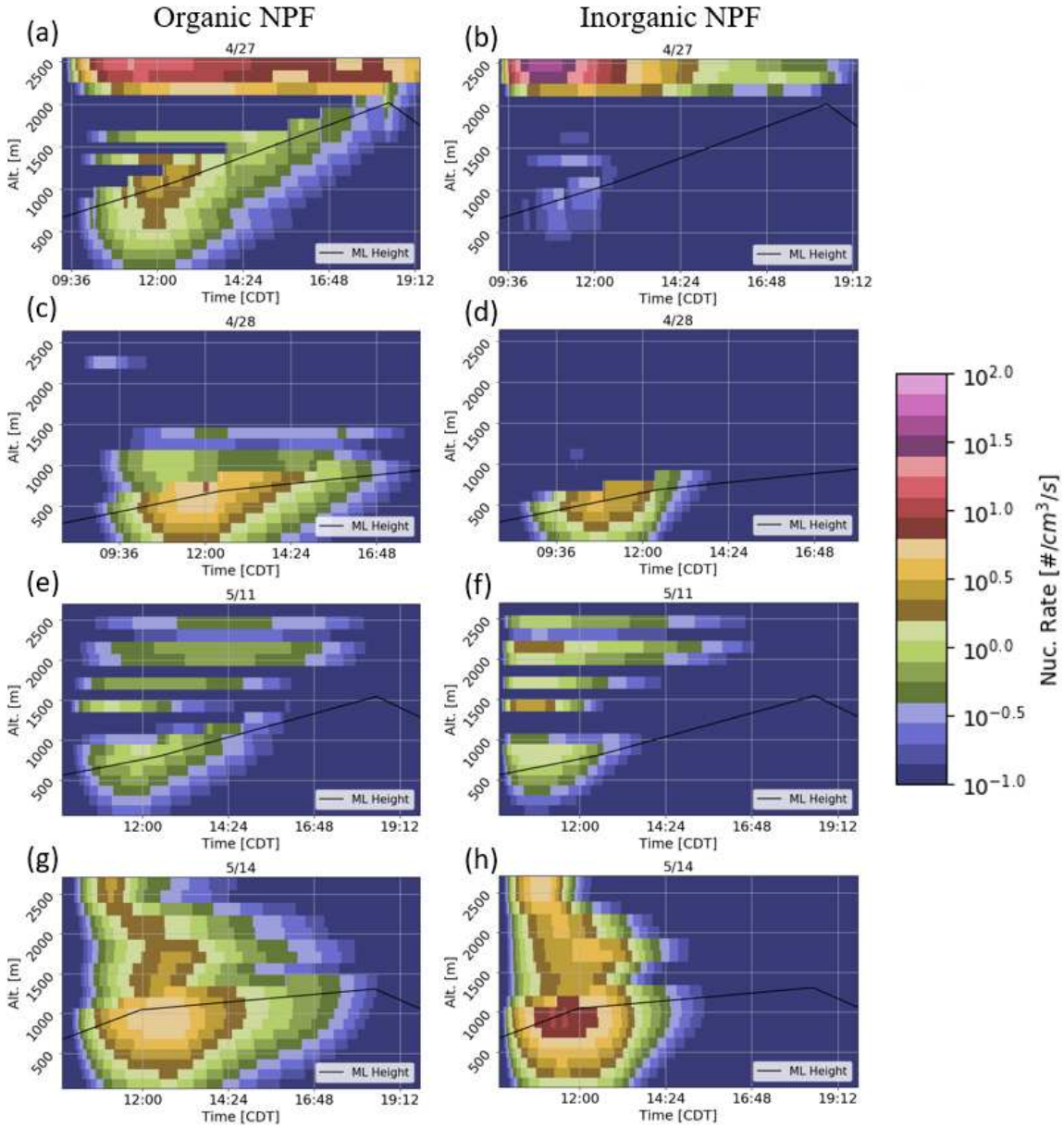

S11. (a-b) Organic (left) and inorganic (right) NPF rate [colors: # $cm^{-3}s^{-1}$] from the base simulation on 27 April. Y-axis indicates the height [m] and the x-axis represents time [CDT]. The height of the mixed layer is indicated by the black line labeled 'ML Height'. (c-d, e-f, g-h) Same as (a-b) but for 28 April, 11 May, and 14 May, respectively.

We find primarily organic-sulfuric acid NPF occurring on 27 and 28 April and primarily inorganic NPF occurring on 11 and 14 May in the base simulations; however, organic-sulfuric acid nucleation contributes to a non-trivial fraction of the total nucleation rate for 11 and 14 May, and the inorganic contribution to nucleation on 28 April is also non-trivial (Figure S11). The two days in May had higher SO_2

concentrations and lower concentrations of terpenes (Table 1), which led to the increased inorganic nucleation. Regardless of the relative contributions of organic-sulfuric acid and inorganic NPF, the organic-sulfuric acid NPF rate persisted longer than the inorganic NPF rate in the simulations. The relative contributions of the organic-sulfuric acid and inorganic NPF schemes to the total NPF rate is sensitive to the assumptions about the contribution of HOMs to the organic-sulfuric acid NPF rate. When 100% of HOMs contribute directly to organic-sulfuric acid NPF, the total nucleation rate is almost entirely driven by the organic-sulfuric acid scheme; contrarily, when only 1% of HOMs contribute to organic-sulfuric acid nucleation, we observe the opposite behavior. Similarly, the relative contribution of organic-sulfuric acid and inorganic nucleation is sensitive to the OH concentration, with higher OH concentrations leading to increased inorganic NPF. For brevity, the details of the sensitivity of the NPF mechanisms to the OH concentrations are not discussed in this work.